

Review

# Overview of Approaches to Increase the Electrochemical Activity of Conventional Perovskite Air Electrodes

Elena Filonova <sup>1,\*</sup>  and Elena Pikalova <sup>2,3</sup> 

<sup>1</sup> Department of Physical and Inorganic Chemistry, Institute of Natural Sciences and Mathematics, Ural Federal University, Yekaterinburg 620002, Russia

<sup>2</sup> Laboratory of Kinetics, Institute of High Temperature Electrochemistry, Ural Branch of the Russian Academy of Sciences, Yekaterinburg 620137, Russia; e.pikalova@list.ru

<sup>3</sup> Department of Environmental Economics, Graduate School of Economics and Management, Ural Federal University, Yekaterinburg 620002, Russia

\* Correspondence: elena.filonova@urfu.ru; Tel.: +7-(343)-251-79-27

**Abstract:** The progressive research trends in the development of low-cost, commercially competitive solid oxide fuel cells with reduced operating temperatures are closely linked to the search for new functional materials as well as technologies to improve the properties of established materials traditionally used in high-temperature devices. Significant efforts are being made to improve air electrodes, which significantly contribute to the degradation of cell performance due to low oxygen reduction reaction kinetics at reduced temperatures. The present review summarizes the basic information on the methods to improve the electrochemical performance of conventional air electrodes with perovskite structure, such as lanthanum strontium manganite (LSM) and lanthanum strontium cobaltite ferrite (LSCF), to make them suitable for application in second generation electrochemical cells operating at medium and low temperatures. In addition, the information presented in this review may serve as a background for further implementation of developed electrode modification technologies involving novel, recently investigated electrode materials.

**Keywords:** SOFC; cathode; air electrode; LSM; LSCF; composite electrode; conductivity; infiltration; collector layer



**Citation:** Filonova, E.; Pikalova, E. Overview of Approaches to Increase the Electrochemical Activity of Conventional Perovskite Air Electrodes. *Materials* **2023**, *16*, 4967. <https://doi.org/10.3390/ma16144967>

Academic Editor: Jose Antonio Alonso

Received: 11 June 2023

Revised: 7 July 2023

Accepted: 10 July 2023

Published: 12 July 2023

Corrected: 19 September 2023



**Copyright:** © 2023 by the authors. Licensee MDPI, Basel, Switzerland. This article is an open access article distributed under the terms and conditions of the Creative Commons Attribution (CC BY) license (<https://creativecommons.org/licenses/by/4.0/>).

## 1. Introduction

The development of renewable energy resources, including hybrid power systems [1–4], is one of the ways for sustainable progress towards decarbonization [5–7]. Hybrid energy systems combining solid oxide fuel cells (SOFCs) with heat generators, energy storage devices, internal combustion engines, and solar cells have been intensively designed and manufactured today [4,8–11]. The progressive trend in the development of SOFCs is to lower the operating temperature, which brings undoubted advantages on the way to the commercialization of these power sources, such as the use of cheaper materials, faster start-up, and increased lifetime due to the reduction of degradation processes. However, challenges arise at low operating temperatures related to the slowing down of electrode reaction kinetics and the increasing ohmic resistance of the electrolyte membrane, resulting in a reduction in the SOFC performance [12,13]. To maintain the electrochemical performance of SOFCs operating at low (LT) and intermediate (IT) temperatures at a satisfactory level, the material optimization has been considered for all construction parts of the SOFC, such as cathodes [14–19], anodes [14,19–21] and electrolytes [19,22–24]. The cathode has been shown to be the major contributor to the electrochemical degradation of the cell [25]. The characterization and performance of the wide range of cathodes can be found in recent reviews [13,26–29].

An analysis of the literature data on the electrical, thermal, mechanical, and electrochemical properties of the conventional perovskite-type cathode materials shows that lanthanum strontium manganite (La,Sr)MnO<sub>3</sub> (LSM) fulfils all the requirements for its

use in high-temperature SOFCs [26,27]. However, as the temperature decreases, the use of LSM materials, which are predominantly electronic conductors with a low level of ionic conductivity, becomes unsatisfactory due to their low electrochemical activity for the oxygen reduction reaction (ORR) [30,31]. On the other hand, cobalt-based perovskite materials, including lanthanum strontium cobaltite ferrite (La,Sr)(Co,Fe)O<sub>3-δ</sub> (LSCF), are characterized by superior catalytic activity [32] due to high values of both electronic and ionic conductivity [33]. However, these materials exhibit increased thermal and chemical expansion, which is detrimental to the long-term operation of SOFCs [33,34]. The poor long-term durability of high-temperature electrochemical cells is often caused by the performance degradation phenomenon of the air electrode [35–37]. It has been found that the electrochemical performance degradation of the LSM- and LSCF-based air electrodes may include microstructural coarsening [33,38,39], the electrolyte/cathode interface reactions [33,40–42], sulfur [43–45] and chromium poisoning [44,46–49], carbon deposition [50,51], and Sr surface segregation [33,35,36,52].

The perceived drawbacks of lanthanum strontium-based cathodes have driven research trends towards alternative solutions to improve their electrochemical performance and durability. A search of the Scopus database using the combination of the keywords “LSM”, “SOFC\*”, “LSCF”, “SOFC\*” (with further application of the limits of “cathode\*”, “cathode materials”, “composite cathode\*”, “cathode polarization”, “cathode performance”, “electrode\*”, “oxygen electrode”, “electrochemical electrodes”) yielded 1141 and 1208 documents respectively for the period of 1996 for LSM and 1998 for LSCF to June of 2023. Figures 1 and 2, generated with the software package *VOSviewer* version 1.6.19 [53], considering a minimum number of occurrences equal to five author keywords, visualize the maps with topic clusters related to LSM and LSCF as cathode materials for SOFCs, respectively.

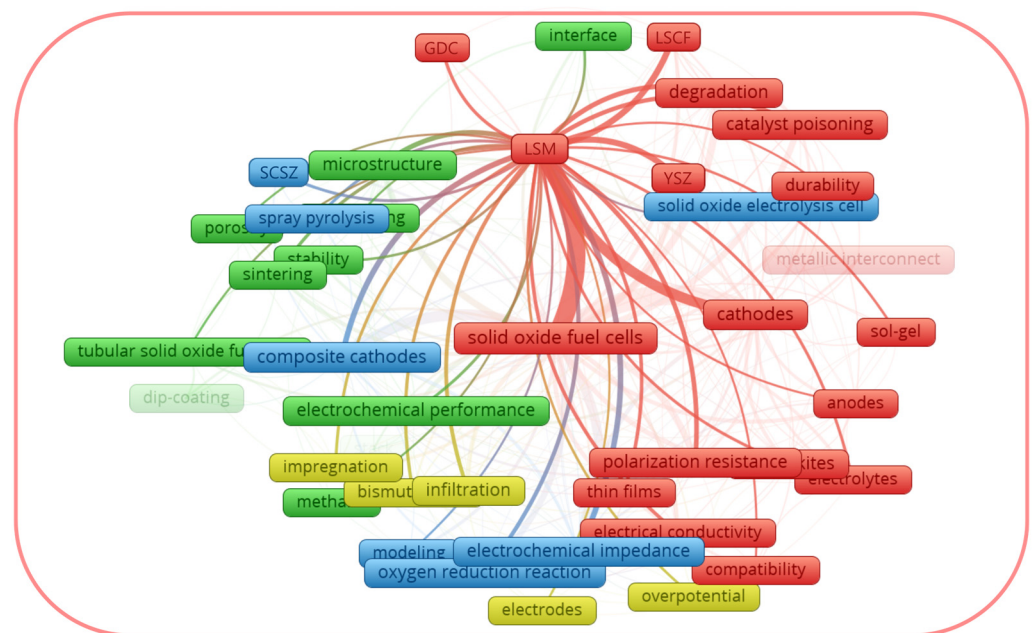


**Figure 1.** Thematic map of co-occurring author keywords in the Scopus dataset for (La,Sr)MnO<sub>3</sub> (LSM).



the reviews [33,36,44], although considering LSCF, did not directly address the cathode enhancement strategies.



**Figure 3.** Network map of bibliographic coupling in the Scopus dataset for LSM.

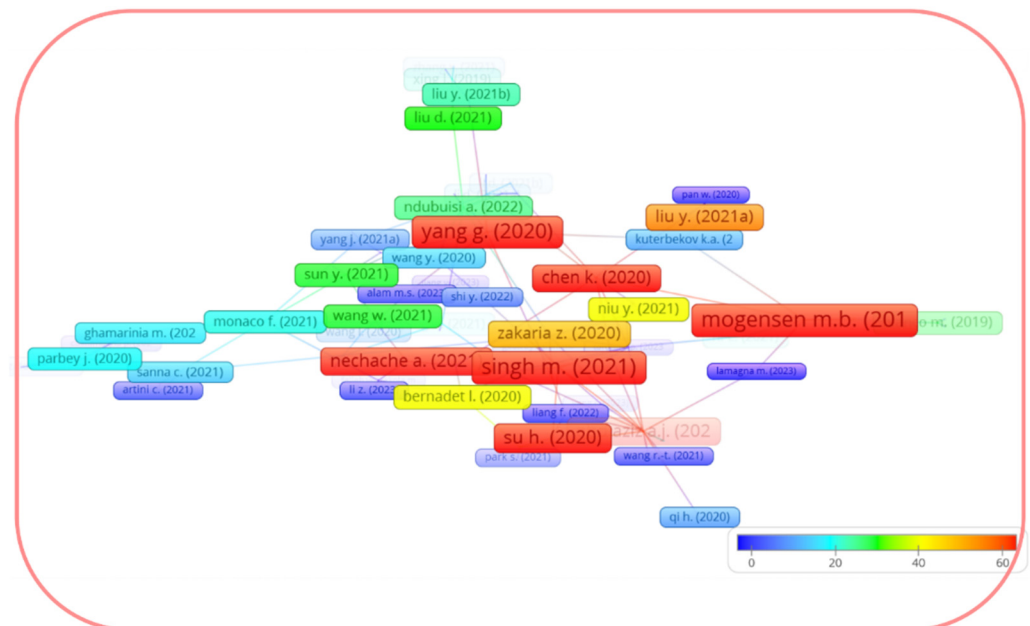


**Figure 4.** Network maps of bibliographic coupling in the Scopus dataset for cited documents of [33].

Therefore, in the present topical review we report on the most promising techniques to improve the electrochemical performance of conventional air electrodes for solid oxide fuel cells and also electrolysis cells based on the lanthanum strontium manganite  $\text{La}_{1-x}\text{Sr}_x\text{MnO}_{3-\delta}$  with  $x = 0.2; 0.3; 0.4$  as the commonly used compositions, and the lanthanum strontium cobaltite ferrite with the composition  $\text{La}_{0.6}\text{Sr}_{0.4}\text{Co}_{0.2}\text{Fe}_{0.8}\text{O}_{3-\delta}$  mainly, as the most prominent representative of the  $(\text{La},\text{Sr})(\text{Co},\text{Fe})\text{O}_{3-\delta}$  series and the most widely used cathode material for the intermediate-temperature (IT) solid oxide fuel cells (IT-SOFCs). The present work highlights for the first time the selection of optimal electrode compositions, as well as electrode fabrication and electrode activation methods.

## 2. Key Functional Properties of LSM and LSCF Electrode Materials: Advantages and Drawbacks

The lanthanum strontium manganite  $\text{La}_{1-x}\text{Sr}_x\text{MnO}_{3-\delta}$  (LSM), as a representative of complex oxides with a perovskite  $\text{ABO}_3$  structure with rhombohedral distortions in the compositional range of  $0.2 \leq x < 0.4$  [56–58], is known to be used as a material for the fabrication of air electrodes for electrochemical devices operating at low- [59] and intermediate temperatures [30]. On the one hand, this is due to the high level of electronic conductivity  $\sigma_e$  for LSM (corresponding to  $200 \text{ S cm}^{-1}$ ,  $250 \text{ S cm}^{-1}$ , and  $320 \text{ S cm}^{-1}$  for  $\text{La}_{0.8}\text{Sr}_{0.2}\text{MnO}_{3-\delta}$  (LSM20),  $\text{La}_{0.7}\text{Sr}_{0.3}\text{MnO}_{3-\delta}$  (LSM30), and  $\text{La}_{0.6}\text{Sr}_{0.4}\text{MnO}_{3-\delta}$  (LSM40), respectively, at  $800 \text{ }^\circ\text{C}$  and at  $\text{Po}_2 = 1 \text{ bar}$  [60]). Secondly, due to the closest values of the coefficient of linear thermal expansion (CTE) of the LSM (e.g., for LSM20— $11.4 \times 10^{-6} \text{ K}^{-1}$  in the range of  $50\text{--}1000 \text{ }^\circ\text{C}$ , [61]; for LSM30— $12.2 \times 10^{-6} \text{ K}^{-1}$  and  $13.2 \times 10^{-6} \text{ K}^{-1}$  in the ranges of  $200\text{--}650 \text{ }^\circ\text{C}$  and  $650\text{--}900 \text{ }^\circ\text{C}$ , respectively, [62]; LSM40— $12.7 \times 10^{-6} \text{ K}^{-1}$  in the range of  $50\text{--}1000 \text{ }^\circ\text{C}$ , [61]); to those for the solid electrolytes perspective for operating in IT-SOFCs and low-temperature SOFCs (LT-SOFCs) [15,22,24,63–65]. The CTE values can be mentioned for doped ceria (e.g., for  $\text{Ce}_{0.8}\text{Sm}_{0.2}\text{O}_{2-\delta}$  (SDC)— $12.0 \times 10^{-6} \text{ K}^{-1}$  in the range of  $25\text{--}1000 \text{ }^\circ\text{C}$ , [66]; for  $\text{Ce}_{0.8}\text{Gd}_{0.2}\text{O}_{2-\delta}$  (GDC)— $12.2 \times 10^{-6} \text{ K}^{-1}$  in the range of  $50\text{--}900 \text{ }^\circ\text{C}$ , [67]), (Sr,Mg)-doped  $\text{LaGaO}_3$  (in general LSGM, e.g., for  $\text{La}_{0.8}\text{Sr}_{0.2}\text{Ga}_{0.8}\text{Mg}_{0.2}\text{O}_{3-\delta}$ — $12.1 \times 10^{-6} \text{ K}^{-1}$  in the range of  $25\text{--}1000 \text{ }^\circ\text{C}$ , [68]),  $\text{Sc}_2\text{O}_3$ -stabilized  $\text{ZrO}_2$  (SSZ) (for 8SSZ— $10.4 \times 10^{-6} \text{ K}^{-1}$  in the range of  $30\text{--}1000 \text{ }^\circ\text{C}$ , [69]). In addition, LSM electrodes offer such an important advantage as the improved stability during operation under SOFC and solid oxide electrolysis cell (SOEC) conditions compared to Fe- [48] and Co- [70,71] containing electrodes.

It should be noted that the oxygen diffusion and interfacial heteroexchange parameters for LSM, which is predominantly an electron conductor, are lower than those of materials possessing high mixed oxygen ion and electron conductivity (MIECs), such as cobalt-based perovskites. For example, the oxygen self-diffusion coefficient ( $D^*$ ) and the oxygen surface exchange coefficient ( $k$ ) for LSM20 at  $800 \text{ }^\circ\text{C}$  were found to be  $4.00 \times 10^{-15} \text{ cm}^2 \text{ s}^{-1}$  and  $5.62 \times 10^{-9} \text{ cm s}^{-1}$ , respectively, compared to  $D^* = 9.87 \times 10^{-10} \text{ cm}^2 \text{ s}^{-1}$  and  $k = 6.31 \times 10^{-7} \text{ cm s}^{-1}$  for the  $\text{La}_{0.8}\text{Sr}_{0.2}\text{CoO}_{3-\delta}$  MIEC material [72]. The values of the ionic conductivity,  $\sigma_i$ , for LSM are in a range of  $10^{-4}\text{--}10^{-7} \text{ S cm}^{-1}$  at  $800\text{--}1000 \text{ }^\circ\text{C}$  and decrease significantly in the intermediate temperature range of  $600\text{--}800 \text{ }^\circ\text{C}$  [30].

Recently Jiang summarized the literature data regarding the characterization of the oxide materials from the lanthanum strontium cobaltite ferrite  $(\text{La,Sr})(\text{Co,Fe})\text{O}_{3-\delta}$  series, and showed that the composition  $\text{La}_{0.6}\text{Sr}_{0.4}\text{Co}_{0.2}\text{Fe}_{0.8}\text{O}_{3-\delta}$  (the acronym LSCF will be used from now on), as a representative of MIECs, is the most prominent cathode material used in IT-SOFCs [33]. LSCF, which has a perovskite structure with rhombohedral distortions [73,74], exhibits excellent electrical properties with ionic and electron partial conductivity values reaching approximately  $1 \times 10^{-2} \text{ S cm}^{-1}$  and  $1 \times 10^2 \text{ S cm}^{-1}$ , respectively, at  $800 \text{ }^\circ\text{C}$  [75]. It demonstrates a moderate CTE value equal to  $17.5 \times 10^{-6} \text{ K}^{-1}$  in the range of  $30\text{--}1000 \text{ }^\circ\text{C}$  [76]. The oxygen self-diffusion and surface exchange coefficients for LSCF amount  $5 \times 10^{-7} \text{ cm}^2 \text{ s}^{-1}$  [77] and  $6 \times 10^{-6} \text{ cm s}^{-1}$  [78] at  $800 \text{ }^\circ\text{C}$ . It should be noted that due to MIEC conductivity nature and the superior oxygen diffusion properties of LSCF compared to LSM, this material is preferred for use in electrochemical devices operated at lower temperatures, whereas LSM materials are still in high demand for high-temperature applications due to their CTE values being more compatible with electrolyte materials and higher total conductivity values.

The main drawbacks of conventional perovskite electrodes, which lead to the degradation of solid oxide cells during long-term operation, are the segregation of Sr at the electrode surface with the formation of the SrO layer for the LSM- [35,52] and LSCF-based [36,79–82] cells, and the high interaction of LSM [41,52,83–86] and LSCF [41,87–90] with Zr-containing electrolytes to form the  $\text{SrZrO}_3$  (SZO) and  $\text{La}_2\text{Zr}_2\text{O}_7$  (LZO) phases. In addition, due to the presence of  $\text{CO}_2$  in the air, the  $\text{SrCO}_3$  carbonate phase was formed on the surfaces of the LSM- [91–93] and LSCF- [94–96] electrodes. The formation of the same insulating phases

limits the oxygen exchange at the electrode–electrolyte interface and reduces the electrocatalytic activity of the LSM [97–100] and LSCF [79,100–105] air electrodes for the ORR, followed by an increase in both the electrode ohmic and polarization resistances. Similar long-term operation tests have shown that the degradation of cells based on LSM [81] or LSCF [106,107] operating in electrolysis mode was higher than that in fuel cell mode, and when comparing two perovskite electrodes, the long-term durability of LSCF was one step ahead of that of LSM [106,108].

Automated methods developed for the detection of Sr nucleation seeds on the electrode surface [109,110], for the identification of the interlayer width between the perovskite and YSZ layers [111,112], and for the computational design and numerical simulation of the perovskite-based composite electrodes [113–116] allowed for the suggestion of possible degradation mechanisms and an understanding of the electrode behavior at both the atomic and macroscopic scales. The deposition of protective and non-catalytic layers on the electrode surface has been proposed as a solution to the problems of segregation [117–119], contaminant poisoning [120–123], and sluggish oxygen kinetics [124–128]. The organization of ceria-based buffer layers at the perovskite electrode/YSZ electrolyte interface and the replacement of the zirconium electrolyte in the composite electrode with other ionic conductors, methods widely used for other perovskite electrodes [129–135], may also help to reduce interactions and increase the activity and long-term stability of LSM [136–138] and LSCF [138–147] electrodes. The high reactivity of the (La, Sr)-containing electrodes with the conventional YSZ electrolyte facilitated extensive investigations of the LSM-based cathodes formed on the SDC [148–151], GDC [152], SSZ [151,153], LSGM [149], BaZr<sub>0.8</sub>Y<sub>0.2</sub>O<sub>3-δ</sub> (BZY20) [154], La<sub>9.5</sub>Si<sub>6</sub>O<sub>26.25</sub> [155], and La<sub>27.44</sub>W<sub>4.56</sub>O<sub>55.68</sub> (LWO56) [156] electrolytes as an alternative. The LSCF-based cathodes were formed on the SSZ [157], SDC [158,159], Ce<sub>0.9</sub>Gd<sub>0.1</sub>O<sub>2-δ</sub> (GDC10) [160–162], GDC [126,163–167] Y<sub>0.1</sub>Ce<sub>0.9</sub>O<sub>1.95</sub> [168], Nd<sub>0.2</sub>Ce<sub>0.8</sub>O<sub>3-δ</sub> [169], SSZ [170], LSGM [171,172], GDC with LSGM [173], SDC with LSGM [174], BZY20 [175], BaZr<sub>0.9</sub>Y<sub>0.1</sub>O<sub>3-δ</sub> [176], BaZr<sub>0.8</sub>Yb<sub>0.2</sub>O<sub>3-δ</sub> (BZYb) [177], BaCe<sub>0.7</sub>Zr<sub>0.1</sub>Y<sub>0.1</sub>Yb<sub>0.1</sub>O<sub>3-δ</sub> (BCZYYb) [178–182], BaCe<sub>0.7</sub>Zr<sub>0.1</sub>Y<sub>0.2</sub>O<sub>3-δ</sub> (BCZY) [183–185], and BaCe<sub>0.7</sub>Zr<sub>0.15</sub>Y<sub>0.15</sub>O<sub>3-δ</sub> (BCZY15) [186] electrolytes.

The chemical compatibility of the LSM and LSCF electrodes with oxygen-ion and proton-conducting electrolytes and the interdiffusion across the cathode/interlayer/electrolyte interfaces have been extensively observed in the recent reviews of Zhang et al. [41], Khan et al. [42] and Hanif et al. [187]. To briefly summarize the data presented in [41], it could be mentioned that LSM20, in contrast to LSCF, showed good chemical compatibility with La<sub>27</sub>W<sub>4</sub>NbO<sub>55-δ</sub> up to 1400 °C [188] and with La<sub>10</sub>Si<sub>55</sub>Al<sub>0.5</sub>O<sub>26.75</sub> at 1300 °C [189], whereas the La-deficient LSM40 did not react with La<sub>0.9</sub>Sr<sub>0.1</sub>Ga<sub>0.8</sub>Mg<sub>0.2</sub>O<sub>2.85</sub> (LSGM9182) at 1300 °C [190]. Secondary phases were found to form after sintering of LSM20 with SDC and BaCe<sub>0.9</sub>Y<sub>0.1</sub>O<sub>3-δ</sub> at 1150 °C [191], La-deficient LSM20 with BZY20 and BaCe<sub>0.8</sub>Y<sub>0.2</sub>O<sub>3-δ</sub> (BCY20) at 1100 °C [192], LSCF with BZY20 and BCY20 at 1100 °C [192]. The conclusions in [41] justified that LSCF had better chemical compatibility with LSGM and CeO<sub>2</sub>-based electrolytes due to the formation of small amounts of impurity phases with LSGM9182 at 1300 °C and negligible interdiffusion with SDC at 1150 °C.

It should be noted that the use of LSM electrodes in contact with the BaCeO<sub>3</sub>-based electrolytes is limited due to their active chemical interaction [193]. However, due to its high electronic conductivity and CTE compatibility, LSM can be successfully used as a collector for perspective layer electrodes for proton-conducting fuel cells operating in the IT range [194–197].

### 3. Conventional and Advanced Techniques to Fabricate Electrode Layers

The choice of electrode deposition method and electrode configuration usually depends on the cell design (tubular/planar configuration), which in turn determines the current characteristics of the electrode. Traditional ceramic methods of the oxygen electrode deposition in planar cells on the supporting fuel electrode, which are technologically simple and easily scalable, are slurry coating [198–201] (LSM), Refs. [202–204] (LSCF), screen printing [205–209] (LSM),

Refs. [110,158,183,210,211] (LSCF), tape casting [212–215] (LSM), Refs. [174,180,216,217] (LSCF), spraying [212,218–221] (LSM), Refs. [170,173,222–224] (LSCF). Figure 5 shows schematics of these deposition methods.

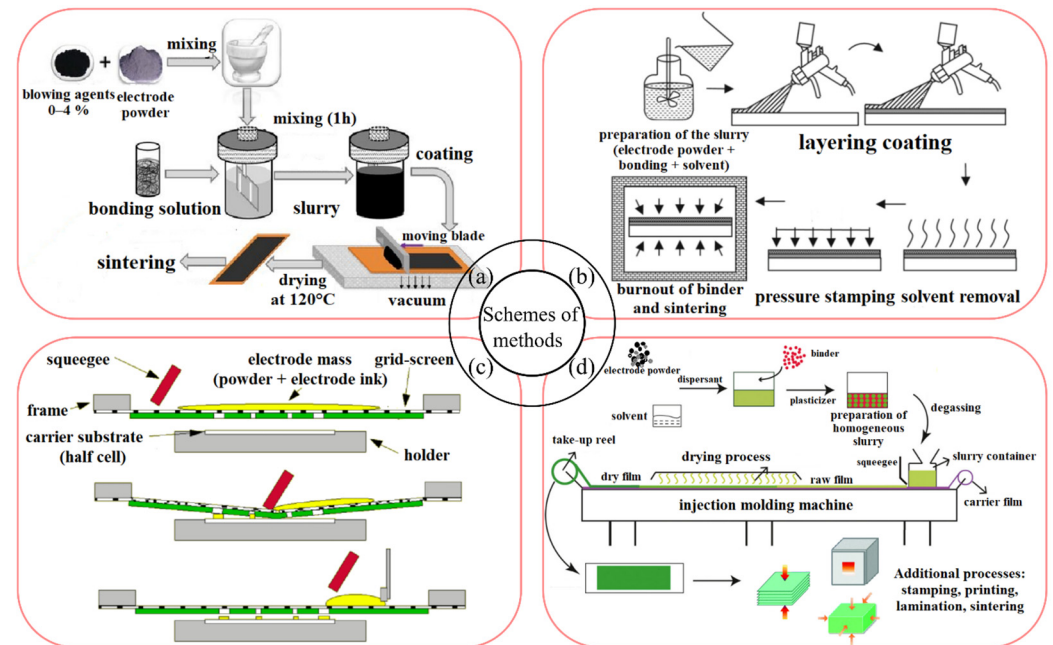


**Figure 5.** Schemes of methods used to apply electrode layers: (a) slurry application; (b) spraying; (c) screen printing; (d) film casting ((a) is reproduced from [225] with permission of IOP Publishing; (b) is reproduced from [226] with permission of Taylor and Francis; (c) is reproduced from [227]; (d) is reproduced from [228] with permission of J. Wiley and Sons).

In addition, freeze casting [229] (LSM), Refs. [230,231] (LSCF), dip coating [232,233] (LSM), Refs. [234–238] (LSCF), and extrusion [239–241] (LSM), Refs. [241–244] (LSCF) have been used to fabricate LSM- and LSCF-based electrodes in microtubular cells. Electrophoretic deposition [245,246] has been applied to form electrode thin films [247–250] (LSM), Refs. [251–254] (LSCF), and to fabricate LSM-based layered electrodes [255,256].

To maintain a high sintering temperature, e.g., to improve adhesion and/or to form air electrodes in the co-sintering process with NiO-based cermet with lower sinterability, different pore formers have been used to control the microstructure of the air electrode: carbon black [257–261] (LSM), Refs. [262–265] (LSCF); various types of starch [154,205,266–269] (LSM), Refs. [251,262,270–272] (LSCF).

To improve the catalytic activity of perovskite electrodes, special techniques for depositing nanoscale layers have been used, which are different from those used for the electrodes based on micro-sized electrode materials. In general, these are mainly the low-temperature methods to maintain the high surface area of the nanosized materials. Among the variety of methods available to improve the conventional perovskite electrodes by extending the triple-phase boundary (TPB), it is worth mentioning spray pyrolysis in its different modifications highlighted in the review [273], and used for LSM in [218,219,274–277], and for LSCF in [223,278–281]; electrospinning represented in reviews [282–284], and used for LSM in [285,286], and for LSCF in [286–292] template method used for LSM in [293], and for LSCF in [294–297]; infiltration method considered in the reviews [298–302], and used for LSM in [26,54,148,154,232,303–312], and for LSCF in [118,182,288,313–344]; solution combustion used for LSM in [345,346], and for LSCF in [346,347]. As a promising technique for the design of solid electrochemical cells, additive manufacturing (3D printing) has demonstrated its advantages for the fabrication of the scalable three-dimensional microstructures [348–351] using the LSM-based electrodes [352–359] and surface-modified LSCF electrodes [337,360,361].

Electrode activation methods are schematically summarized in Figure 6. They include the use of composite materials, materials with mixed electronic and ionic conductivity, the introduction of an active interlayer at the electrode–electrolyte interface (e.g., a highly conductive ionic conductor), the exfoliation of active nanoparticles on the electrode surface, infiltration, the use of nanomaterials. Due to the predominantly electronic nature of LSM materials, the selection and application of appropriate activation methods are necessary, especially for the electrodes used in electrochemical devices operating at decreased temperatures (below 800 °C).

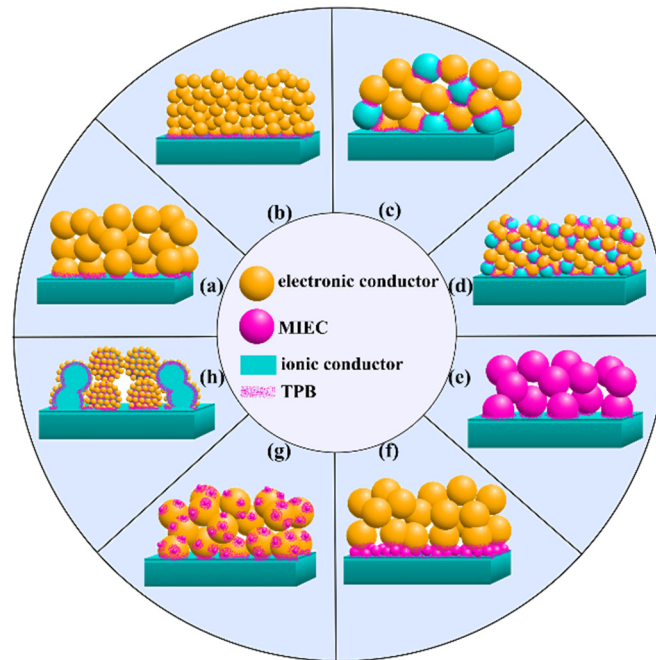


**Figure 6.** Air electrode activation method for electrochemical devices: (a) electronic conductor with localization of the TPB at the electrode–electrolyte interface; (b) nanosized electrode; (c) composite conductor/electronic conductor; (d) nanocomposite electrode; (e) mixed ionic–electronic conductor with extended TPB; (f) thin film active layer at the electrode–electrolyte interface; (g) electronic conductor in a porous ionic conductor matrix obtained by infiltration; (h) nanoparticle exfoliation on the surface of the electronic conductor.

#### 4. Methods to Improve the Electrochemical Performance of the Conventional Electrodes

##### 4.1. Optimization of the Oxide Composition

The interaction of LSM with Zr-containing electrolytes, as it was mentioned above, results in the formation of low conducting LZO and, at high strontium content, SZO phases at the electrode sintering stage at temperatures above 1000–1200 °C, depending on the material dispersity [85]. It has also been found that Mn readily dissolves in YSZ, leaving chemically active  $\text{La}_2\text{O}_3$  at the LSM/YSZ interface, which reacts with  $\text{ZrO}_2$  to form LZO [114]. To reduce the interaction of LSM with Zr-containing electrolytes, the use of  $(\text{LS})_x\text{M}$ , a cation deficient in the A position, has been proposed [129]. It was found that the creation of the A-site deficiency suppressed the formation of the parasitic LZO phase due to the decrease in the La chemical potential. However, it should be noted that increasing the deficiency beyond a certain limit led to the release of the  $\text{MnO}_x$  phase in  $(\text{LS})_x\text{M}$ , resulting in the intensification of interphase reactions. Thus, recent studies on the interaction of  $(\text{La}_{0.75}\text{Sr}_{0.25})_x\text{MnO}_{3-\delta}$  ( $x = 1.0, 0.97, 0.95, 0.9$  and  $0.85$ ) with the SSZ electrolyte showed that the optimum deficiency level was 0.95 [153]. The composite electrode  $(\text{LS})_{0.95}\text{M}$  containing 50 mol% SSZ was characterized by the lowest values of polarization resistance  $R_p$  (sometimes called  $R_\eta$ , ASR in the works of different groups) and serial resistance  $R_s$  in the series studied, despite the high temperatures of the electrode

formation. Therefore, the values of  $R_p$  and  $R_s$  for the electrodes sintered at 1200 and 1300 °C were equal to 1.21 and 1.94  $\Omega \text{ cm}^2$  and 0.82 and 1.60  $\Omega \text{ cm}^2$  at 950 °C, respectively.

The excess of Mn in  $\text{La}_{0.85}\text{Sr}_{0.15}\text{Mn}_y\text{O}_{3-\delta}$  (LSMy,  $y = 1.1$ ) was found to prevent the formation of chemically active  $\text{La}_2\text{O}_3$  and thus, the formation of LZO. In [362], it was shown that the use of LSM1.1 instead of LSM in a composite electrode with 20 wt% YSZ resulted in a reduction of  $R_p$  from 1.6 to 0.6  $\Omega \text{ cm}^2$  at 1000 °C. It has been shown that the modification of the YSZ electrolyte with Mn also results in a reduction of the LSM/YSZ interaction [363,364].

In the case of LSCF, the A-site cation-deficient materials with the  $(\text{LS})_x\text{CF}$  and  $\text{L}_x\text{SCF}$  composition have been developed and widely used [175,365,366] due to their improved electrical conductivity and reduced CTE values [367]. Meanwhile, based on the results of the long-term stability study of the YSZ electrolyte-supported SOFC with the  $(\text{LS})_{0.98}\text{SF}$  cathode, Simner et al. [79] concluded that the high rate of the cell degradation (about 30% during 500 h) was mainly caused by Sr segregation at the cathode–electrolyte and cathode/collector layer interfaces, without any significant microstructural and chemical changes. Bucher et al. [366] also confirmed that  $\text{L}_{0.96}\text{SCF}$  underwent strong Si-induced degradation at 600 °C in both wet and air atmospheres.

As a possible solution to the problem of the Sr segregation and contaminant poisoning in the perovskite electrodes, the use of high entropy oxides (HEOs) containing at least five co-dopants in an equimolar ratio in the A-position could be considered [19]. Recently, HEOs based on LSM have been reported, such as  $\text{La}_{0.2}\text{Pr}_{0.2}\text{Nd}_{0.2}\text{Sm}_{0.2}\text{Sr}_{0.2}\text{MnO}_3$  [368] and  $\text{La}_{0.2}\text{Nd}_{0.2}\text{Sm}_{0.2}\text{Ca}_{0.2}\text{Sr}_{0.2}\text{MnO}_3$  [369]. It was shown that the distortions in the LSM perovskite structure caused by the multi-doping in the A-site led to the highly disordered stress field around the Sr ions, which resulted in limiting the transport and migration of the Sr ions, and suppressed the Sr segregation phenomenon [368,369]. Dabrowa et al. [370] synthesized a nanosized homogeneous high entropy oxide (HEO) based on LSCF, such as  $\text{La}_{0.6}\text{Sr}_{0.4}\text{Co}_{0.2}\text{Cr}_{0.2}\text{Fe}_{0.2}\text{Mn}_{0.2}\text{Ni}_{0.2}\text{O}_{3-\delta}$ . The resulting HEO was characterized by lower CTE, increased electronic conductivity, and enhanced stability to Cr contamination compared to the base oxide [370].

Xu et al. [371] synthesized the orthorhombic phase  $\text{La}_{0.2}\text{Nd}_{0.2}\text{Gd}_{0.2}\text{Sr}_{0.2}\text{Ba}_{0.2}\text{Co}_{0.2}\text{Fe}_{0.8}\text{O}_{3-\delta}$  (HE–LSCF) and investigated the electrochemical activity of the HE–LSCF on the SDC substrate in the symmetrical cells. The  $R_p$  value for the HE–LSCF cathode was measured to be 0.57  $\Omega \text{ cm}^2$  at 700 °C compared to 0.71  $\Omega \text{ cm}^2$  for the conventional LSCF cathode. The kinetics of the oxygen reduction reaction in the HE–LSCF cathode, related to the processes of oxygen dissociation and interfacial charge transfer, was attributed by the authors to the middle-frequency process. The polarization results obtained for the cells aged at 800 °C for 200 h showed that the HE–LSCF cathode was characterized by higher stability compared to the pristine LSCF cathode. The  $R_p$  values were 0.75 and 1.27  $\Omega \text{ cm}^2$  at 700 °C for the high-entropy LSCF cathode and the conventional LSCF cathode, respectively. Scanning electron microscopy (SEM) and energy dispersive spectroscopy (EDS) data confirmed that the surface of the HE–LSCF cathode had a homogeneous distribution of all elements in the A-position with no Sr segregation both before and after cell ageing in contrast to the pristine LSCF cathode. The authors reported that the Sr segregation was successfully suppressed in the HE–LSCF cathode.

In summary, although the formation of the (La,Sr)-deficient sites, which aims at both increasing the electrical conductivity and suppressing Sr segregation is the most widely used technique for selecting the optimal composition of the LSM and LSCF electrodes, the creation of highly disordered oxides with sluggish cation diffusion can be quite perspective direction in the composition modification of the conventional perovskite materials.

#### 4.2. Enhancement of the Ionic-Conducting Electrode Component

To increase the electrochemical activity of LSM air electrodes, their compositions with ionic conductors were applied, e.g., with solid electrolytes (YSZ [205,303,352,372–383], YSZ with GDC10 [374], SSZ [149,384–390], GDC10 [391], GDC [152,198], SDC [148,149,387,392,393], doped  $\text{Bi}_2\text{O}_3$  [151,394–399],  $\text{BaZr}_{0.85}\text{Y}_{0.15}\text{O}_{3-\delta}$  (BZY15) [154], LWO56 [156], LSGM [400,401]),

or MIEC materials (Co- [150,402] and Fe-based perovskites [403–405]). The optimum electrolyte content in the composite electrode depends on the specific surface area ratio of the components and is in the range of 30–50 wt% in most cases. Calculations using *Comsol* software showed that the maximum active TPB of  $9.53 \mu\text{m} \mu\text{m}^{-3}$  was achieved for electrodes containing 35 vol% of the electrode material, 35 vol% of the electrolyte and 30 vol% of pores [396].

Wang et al. [373] found that the enhancement of the electrochemical activity of the LSM–YSZ composites was due to the spatial enlargement of the triple-phase boundary (TPB) area, which increased the active sites for the oxygen adsorption and charge transfer processes. Lee et al. [383] reported on dissociative adsorption as the main rate-determining step of the ORR on the LSM–YSZ composite cathodes. It was found that the replacement of YSZ with GDC in the LSM–based composite electrodes developed in [152] resulted in much lower current interfacial resistances compared to the conventional LSM–YSZ electrodes on the corresponding electrolytes.

A detailed study of the influence of ionic conductivity on the properties of the LSM20-based composite electrodes was carried out by Yaroslavtsev et al. in [149], using high ionic conductivity materials SSZ, SDC and  $\text{La}_{0.88}\text{Sr}_{0.12}\text{Ga}_{0.82}\text{Mg}_{0.18}\text{O}_{2.85}$  (LSGM8282) as the electrolyte component, whose content in the composite electrodes was 50 wt%. The thickness of the electrodes, obtained by screen-printing of a powder suspension with polyvinyl butyral (PVB) binder with the addition of ethyl alcohol, was  $50 \mu\text{m}$ . A collector layer of LSM40 composition was used for the composite electrode to ensure stable current collection. Sintering of the 50LSM20–50SSZ micro-sized electrode layers was carried out at 1200 and 1250 °C, 1 h. Figure 7a shows the characteristics of the electrodes after sintering and after activation with praseodymium oxide (m) in symmetrical cells based on the Sm-doped ceria electrolyte of the composition often used to organize buffer layers at the air electrode–electrolyte interface in  $\text{ZrO}_2$  and  $\text{LaGaO}_3$ -based cells). The 50LSM20–50SDC composite electrode was found to have the best performance, with the 50LSM20–50SSZ electrode with LSM40 collector coming close. The polarization conductivities of the modified 50LSM20–50SDC and 50LSM20–50SSZ/LSM40 electrodes were 114 and 100  $\text{S cm}^{-2}$  at 800 °C, corresponding to  $R_p$  of 0.009 and 0.01  $\Omega \text{cm}^2$ .

Furthermore, Yaroslavtsev et al. have proposed to modify the properties of 50LSM20–50SDC and 50LSM20–50SSZ electrodes by activation through the LSM40 collector layer containing Y-doped bismuth oxide  $\text{Bi}_{1.5}\text{Y}_{0.5}\text{O}_{3-\delta}$  (YDB) [151]. It was shown that when the collector layer was sintered at 1000 °C, the polarization resistance of the electrodes decreased due to the diffusion of bismuth-containing melt phases into the functional composite layer (Figure 7b). The optimum additive content in the collector layer for both electrodes was therefore set at the level of 5 wt% (Figure 7c,d). When the YDB content was increased beyond this value, a decrease in the cathode performance was observed due to the sintering and reduction in porosity of the collector layer. The  $R_p$  values of 0.1 and 0.2  $\Omega \text{cm}^2$  at 800 °C were obtained for the 50LSM20–50SDC and 50LSM20–50SSZ electrodes, which were optimized in terms of sintering temperature and amount of the additive. The composite electrodes, activated through the collector, exhibited higher  $R_p$  values compared to the praseodymium oxide-activated electrodes; however, they demonstrated a significantly lower degradation rate.

Mosiłek et al. [150] investigated the performance of the composite cathodes containing LSM20 and the MIEC material of  $\text{YFe}_{0.5}\text{Co}_{0.5}\text{O}_3$  (YFC) formed on the SDC electrolyte by screenprinting. It was found that the addition of 5 wt% YFC to LSM resulted in a decrease of the polarization resistance  $R_p$  from 2.7 to 1.9  $\Omega \text{cm}^2$  at 800 °C. This fact was attributed to the facilitation of the charge transfer process.

LSM composite electrodes can be prepared by various techniques: by mechanically mixing the components in a mill [114,396], by forming composites with a core–shell structure (by depositing one material on top of another) [206], by infiltrating one component of the composite electrode into the pre-sintered porous matrix of the other component [198,377], and by preparing vertically oriented high-entropy nanocomposites [393].

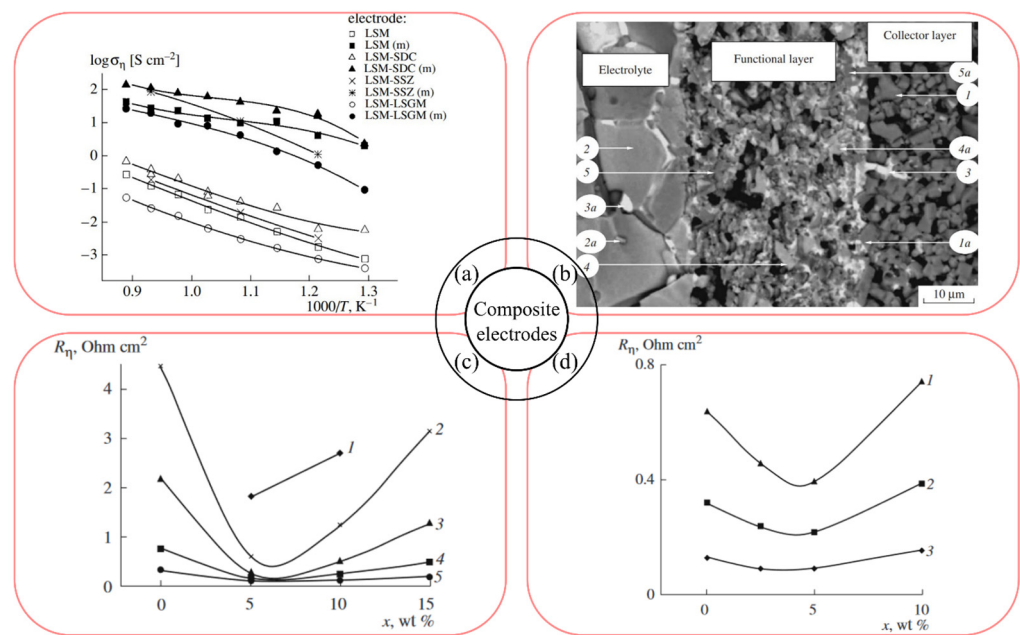


**Figure 7.** Effect of activation on the properties of composite electrodes of different composition applied by screen printing on SDC electrolyte: (a) temperature dependences of polarization conductivity for basic and praseodymium oxide (m) modified 50 wt% LSM20 based electrodes; (b) SEM micrograph showing diffusion of bismuth-based fusible components from 95LSM40–5YDB collector into 50LSM20–50SDC functional layer and YSZ electrolyte (Bi-containing phases are denoted by 3, 3a and 5, 5a); (c,d) polarization resistance of 50LSM20–50SDC and 50LSM20–50ScSZ electrodes with LSM40 collector as a function of its YDB content ( $x$ ) ((a) is reproduced from [149] with permission of Springer; (b–d) are reproduced from [151] with permission of Springer).

In [206], the  $60(\text{LS})_{0.95}\text{M}_{25}\text{–}40\text{YSZ}$  composite powder was obtained by the synthesizing of LSM on submicron YSZ particles using in situ glycine-nitrate combustion method. The electrode with a core-shell structure was formed on the surface of the YSZ electrolyte by screen printing (Cell A). The organic binder consisted of 5 wt% ethyl cellulose dissolved in 95 wt% terpeneol, and the weight ratio of electrode powder to the binder in the stencil was 2:3. The applied electrode was sintered at 1180 °C for 2 h. For comparison, the second electrode was formed under the same conditions from a mechanical mixture of YSZ and LSM, synthesized by the glycine-nitrate combustion method (Cell B). The YSZ electrolyte formation in the half-cells on the NiO–YSZ support cathode for the single-cell test was also carried out by screen printing with sintering at 1400 °C for 2 h, with a film thickness of about 10  $\mu\text{m}$ . The authors observed a reduction in the electrolysis cell performance when using an anode produced by conventional mixing. Current densities of 0.520  $\text{A cm}^{-2}$  and 0.431  $\text{A cm}^{-2}$  at 900 °C and 0.333  $\text{A cm}^{-2}$  and 0.231  $\text{A cm}^{-2}$  at 850 °C at 1.50 V were obtained for Cell A and Cell B, respectively.

It should be noted that the dispersity of the materials used has a great influence on the performance of composite electrodes obtained by mechanical mixing. It is therefore important to obtain LSM powders with nanosized particles. According to the data reported in [406],  $\text{La}_{0.5}\text{Sr}_{0.5}\text{MnO}_{3-\delta}$  (LSM50) with homogeneous morphology and nanoparticles of 20 nm, prepared by the Pechini method, has been characterized as a material that provides improved electrode activity compared to those obtained with LSM50 powders synthesized by citrate and alkoxide techniques. The application of nanosized (86 nm) low-agglomerated powder ( $\text{La}_{0.75}\text{Sr}_{0.25}\text{MnO}_{3-\delta}$  ((LS) $_{0.95}\text{M}_{25}$ ), obtained by pyrolysis of acetate acrylic polymer, in the composite with YSZ reduced the electrode polarization to less than 0.1  $\Omega \text{ cm}^2$  at 800 °C [378]. A 20  $\mu\text{m}$  thick  $50(\text{LS})_{0.95}\text{M}_{25}\text{–}50\text{YSZ}$  composite was formed in a NiO–YSZ|YSZ half-cell by spraying an ethanol-based suspension followed by drying and sintering at 1000 °C for 2 h (Figure 8a).

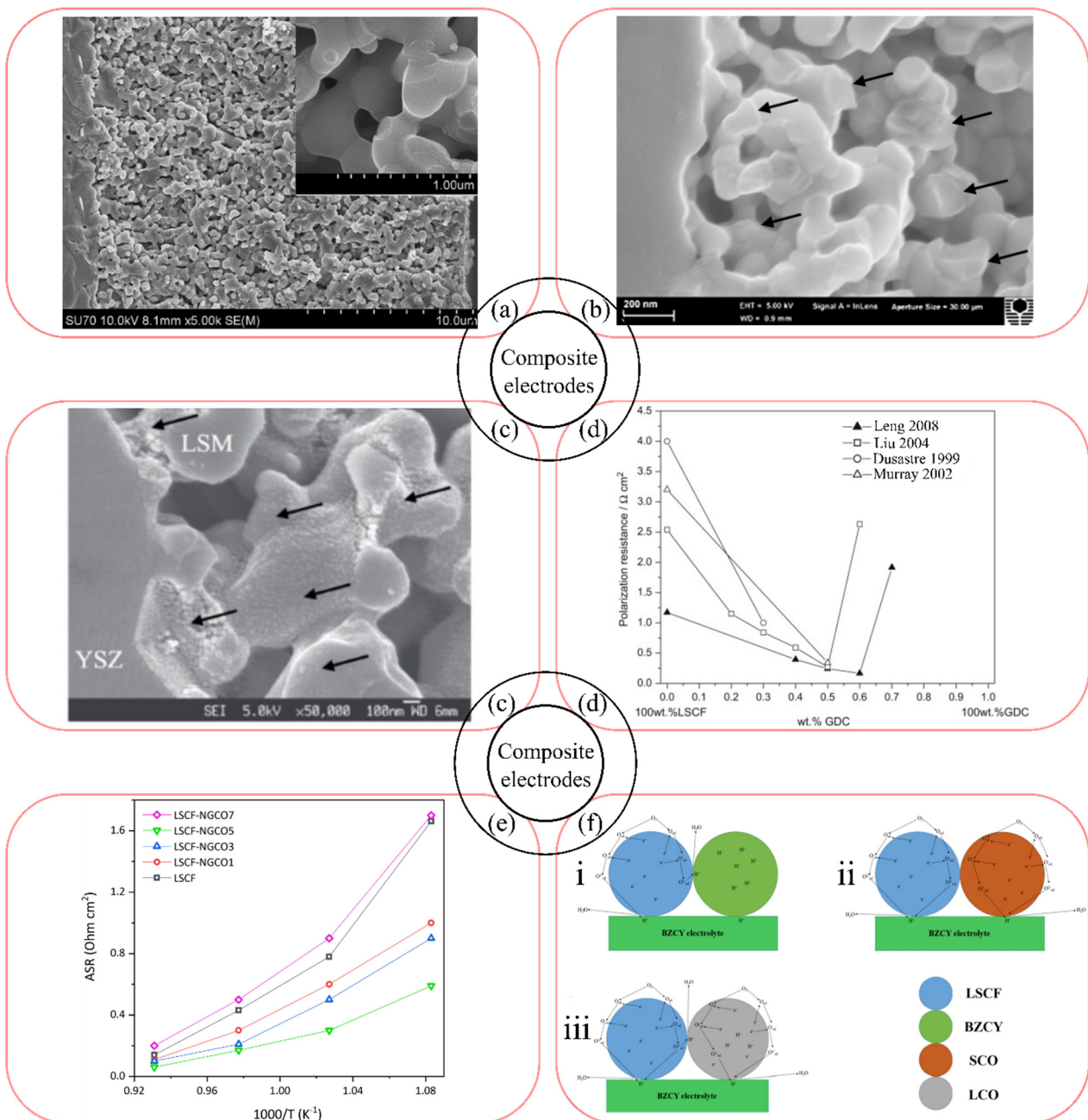


**Figure 8.** SEM micrograph of the 50(LS)<sub>0.95</sub>M25-50YSZ electrode of 20 μm thickness, prepared by nanopowder suspension spraying followed by sintering at 1000 °C, 2 h (a); YSZ ceramic matrix followed by heat treatment at 600 and 1100 °C (arrows indicate LSM particles) (b); SEM micrograph of the 75LSM20-25GDC electrode obtained by GDC infiltration into the LSM ceramic matrix (arrows indicate GDC particles) (c); polarization resistance of the LSCF-GDC10 composite cathodes on the GDC10 content at 600 °C by Leng et al. [407], Liu et al. [408], Dusastre et al. [409], Murray et al. [410], (d); temperature dependencies of the polarization resistance for LSCF-NGCO cathodes characterized in symmetrical cells (e); scheme of migration paths of conducting species in LSCF-BZCY (i), LSCF-SCO (ii), LSCF-LCO (iii) composite cathodes on BZCY electrolyte (f) ((a) is reproduced from [378] with permission of Elsevier; ((b) is reproduced from [377] with permission of Elsevier; (c) is reproduced from [198] with permission of Elsevier (d) is reproduced from [407] with permission of Elsevier; (e) is reproduced from [166]; (f) is reproduced from [185] with permission of Elsevier).

The application of infiltration leads to both an increase in the activity of the composite electrode and a solution to the problem of electrode delamination, which is particularly

pronounced under conditions of anodic polarization. For example, the 45LSM20–55YSZ nanostructured electrodes, obtained in [377] by infiltration of  $\text{La}_{0.8}\text{Sr}_{0.2}\text{Mn}(\text{NO}_3)_x$  with addition of citric acid into the porous YSZ ceramic matrix (Figure 8b), followed by a two-step temperature treatment at 600 °C and then at 900 or 1100 °C, showed  $R_p$  values of 0.21 and 0.74  $\Omega \text{ cm}^2$  at 800 °C, respectively. The YSZ matrix for the composite electrode was formed in [377] on the YSZ electrolyte surface by slurry coating followed by sintering at 1200 °C for 2 h. In [198], the 75LSM20–25GDC composite was prepared by infiltrating the solution of  $\text{Gd}_{0.2}\text{Ce}_{0.8}(\text{NO}_3)_x$  into a 20–30  $\mu\text{m}$ -thick porous LSM matrix (Figure 8c) formed by slurry deposition followed by presintering at 1100 °C for 2 h. The polarization resistance of the bare LSM electrode measured at 8.2  $\Omega \text{ cm}^2$  at 800 °C was reduced to 0.39 and 0.09  $\Omega \text{ cm}^2$  after infiltration with 0.5 and 1.5  $\text{mg cm}^{-2}$  GDC, respectively. The electrodes, developed by Chen et al. [198,377], showed high stability under polarization with an anodic current of 500  $\text{mA cm}^{-2}$  at 800 °C in air for 100 h. However, it should be noted that the area of the infiltrated electrodes is generally small ( $<1 \text{ cm}^2$ ) because it is difficult to obtain a homogeneous distribution of the component in the matrix over a large area in a non-mechanized infiltration process.

For the preparation of the LSCF-based electrodes, compositions with ionic conductors were used, such as YSZ [411,412], YSZ with GDC10 [413], GDC10 [160,336,407,414–418] GDC [110,120,171,417–421],  $\text{Nd}_x\text{Gd}_{0.15}\text{Ce}_{0.85-x}\text{O}_{2-\delta}$  (NGCOx) [166], SDC [114,127,162, 184,185,416,422–426],  $\text{Ce}_{0.8}\text{Zr}_{0.2}\text{O}_{2-\delta}$  [427], BZYb [177], BCZYYb [178,181], BCZY [185], BCZY15 [186],  $\text{La}_2\text{Ce}_2\text{O}_7$  (LCO) [185], LSGM [428,429], as well as with the MIEC materials  $\text{Bi}_{0.3}\text{Sr}_{0.7}\text{Co}_{0.3}\text{Fe}_{0.7}\text{O}_{3-\delta}$  [172],  $\text{La}_{0.94}\text{Ni}_{0.6}\text{Fe}_{0.4}\text{O}_3$  (LNF94) [340],  $\text{Ba}_{0.5}\text{Sr}_{0.5}\text{Co}_{0.8}\text{Fe}_{0.2}\text{O}_{3-\delta}$  [430],  $\text{SrCo}_{0.2}\text{Fe}_{0.6}\text{Ni}_{0.2}\text{O}_{3-\delta}$  [431]. As in the case of the LSM-based composites, the LSCF-based composite electrodes can be prepared by conventional mixing [166,185,407], infiltration [340,416–418,421,425,426], and by creating core-shell structures [340,424].

Ling et al. [407] evaluated the electrochemical activity of the pristine LSCF cathode and the LSCF–GDC10 composite cathodes at the operating temperatures of 500–700 °C. The  $R_p$  value of the LSCF porous electrode, sintered on the thin-film GDC10 electrolyte at 975 °C, was measured to be 1.20  $\Omega \text{ cm}^2$  at 600 °C. The GDC10 additives to LSCF improved the electrode performance, reducing the polarization resistance down to 0.17  $\Omega \text{ cm}^2$  at 600 °C for the LSCF–GDC composite cathode with the GDC10 content of 60 wt%. The higher GDC10 content resulted in an increase of polarization resistance, which was consistent with the ambipolar resistivity model of the porous composite cathode [409]. It has been shown that the polarization resistance increases in the composites with high electrolyte content because the electron-conducting pathways cannot be effectively formed [407]. Besides, both the ohmic resistance and the contact resistance were high for the LSCF–GDC10 composite cathode with the GDC10 content of 70 wt%. Therefore, it was concluded that the optimum GDC content to achieve the lowest polarization resistance of the LSCF–GDC10 composite cathode was 60 wt%. The performance of the single cell with the optimized LSCF–GDC composite as the cathode, GDC10 as the electrolyte, and Ni–GDC10 as the anode was characterized by the maximum power density (MPD) value of 422  $\text{mW cm}^{-2}$  at 600 °C. The superior electrochemical performance of the LSCF–GDC10 composite cathode, observed in [407], compared to that obtained in [408–410] (as shown in Figure 8d) is consistent with the model that the optimum GDC10 volume fraction to achieve the minimum polarization resistance may be greater than 50 wt%, since the grain size of the LSCF powder is much smaller compared to that of the GDC powder.

A simple method for the preparation of nanosized composites has been proposed by Xi et al. [415]. The LSCF–GDC10 powders were obtained from  $\text{La}_2\text{O}_3$ ,  $\text{Sr}(\text{OH})_2$ ,  $\text{Co}_3\text{O}_4$ ,  $\text{Fe}_2\text{O}_3$ , and GDC10 powders, mechanically treated in a high-speed attrition-type mill for 20 min. The resulting composite electrodes, sintered on the SSZ substrate at 900 °C, were characterized by the corresponding polarization resistance value of 0.38  $\Omega \text{ cm}^2$  at 700 °C. The authors of [415] concluded that the mechanical treatment allowed the formation of nanosized particles in the LSCF–GDC10 composite as compared to the conventional mixing technique with the formation of micro-sized particles.

Samreen et al. [166] used the co-doped GDC for the fabrication of the LSCF–NGCO<sub>x</sub> composite electrodes (*x* was equal to 1, 3, 5, 7 wt%), obtained from the corresponding powder mixtures. According to the electrochemical impedance spectroscopy (EIS) data obtained on the symmetrical cells with the LSCF–NGCO<sub>x</sub> electrodes, sintered at 1100 °C on the GDC substrate, the lowest  $R_p$  equal to 0.31  $\Omega\text{ cm}^2$  at 700 °C was observed for NGCO5. As shown in Figure 8e, the NGCO5-based electrode showed better performance not only compared to LSCF and other studied LSCF–NGCO<sub>x</sub> electrodes [166], but also compared to the LSCF–GDC10 electrodes [415]. Thus, the Nd co-doping of GDC can be considered as the promising way for the fabrication of the composite electrodes based on LSCF due to the improvement of the oxygen ion diffusion pathways and the optimization of the TPB sites.

In [120], the GDC-coated LSCF composite cathode prepared by the dip-coating technique was shown to have both the excellent electrochemical performance and the Cr poisoning tolerance. According to the EIS results, the 76LSCF–24GDC composite cathode was characterized by the polarization resistance value of 0.59  $\Omega\text{ cm}^2$  at 700 °C, compared to 0.87  $\Omega\text{ cm}^2$  at 700 °C for the bare LSCF. The 76LSCF–24GDC and LSCF cathodes showed the  $R_p$  values of 0.71 and 1.35  $\Omega\text{ cm}^2$  at 700 °C, respectively. After the stability tests under the Cr poisoning conditions for 200 h. Zhang et al. [120] considered that the Cr poisoning of the composite cathode was reduced due to the diminishing of both Cr deposition on the electrode surface and the SrCrO<sub>4</sub> formation.

Three different types of the LSCF-based composite cathodes for proton-conducting fuel cells (PCFCs) were obtained and investigated in [185]. The LSCF–SDC, LSCF–BCZY, LSCF–LCO electrode slurries were prepared from the LSCF and SDC, BCZY, and LCO powders, respectively, mixed in a 7:3 weight ratio using terpineol and ethyl cellulose as binders. The power densities of the anode-supported cells (ASC) with the LSCF–SDC, LSCF–BCZY, and LSCF–LCO cathodes, sintered on the BCZY electrolyte at 1000 °C, were measured to be 421, 432, 469  $\text{mW}\cdot\text{cm}^{-2}$  at 600 °C. The long-term operation tests of the single cell with the LSCF–LCO cathode showed the stability of the cell power of 420  $\text{mW}\text{ cm}^{-2}$  during 100 h at 600 °C without any obvious degradation. Gao et al. [185] suggested that the excellent performance of the LSCF–LCO cathode, compared to LSCF–SDC and LSCF–BCZY was due to the enhanced migration rates of proton and oxygen ions through the BCZY electrolyte, as shown in Figure 8f.

According to the conclusions of the work [421], the LSCF-based cathodes, obtained as a three-dimensional network of nanofibers had such advantages as high porosity, high percolation, continuous paths for charge migration, good thermal stability, and excellent framework for subsequent infiltration. The maximum power densities of the single cells with the NiO–YSZ as anode, YSZ as electrolyte, LSCF nanofiber cathode, prepared by electrospinning, and LSCF–GDC composite, prepared by the GDC infiltration, were measured to be 900 and 1070  $\text{W}\text{ cm}^{-2}$  at 1.9  $\text{A}\text{ cm}^{-2}$  at 750 °C, respectively. The polarization resistances of the LSCF and LSCF–GDC composite cathodes were equal to 0.26 and 0.21  $\Omega\text{ cm}^2$  at 750 °C, respectively. In [417], the LSCF–GDC10 composite cathodes were formed from the LSCF nanofibers deposited on the GDC10 electrolyte, and the GDC10 was introduced into the LSCF scaffold by the infiltration method. The polarization resistances for the LSCF nanofiber and LSCF–GDC10 (weight ratio of 1:0.56) composite cathodes were equal to 0.78 and 0.14  $\Omega\text{ cm}^2$  at 700 °C, respectively. The size of the infiltrated particles also may have an influence on the electrode performance. Burye and Nicholas [432] used desiccation of LSCF precursor nitrate solutions infiltrated into porous GDC10 scaffold with CaCl<sub>2</sub> to decrease the average size of the infiltrated LSCF particles in the LSCF–GDC10 composite cathode down to 22 nm, which was more than twice lower than that in the pristine cathode. It allowed polarization resistance of 0.10  $\Omega\text{ cm}^2$  to be obtained at 575 °C, compared to 650 °C for the undesiccated electrode. The results of the works [417,421,432] demonstrated the efficiency of the infiltration method in achieving the high cell performance of the solid oxide fuel cells.

The 50LSCF–50SDC core–shell composite cathode was prepared in [424]. The 500-nm size of the SDC core was controlled to achieve the total encapsulation of the SDC particles

with the LSCF particles, resulting in the improved phase homogeneity with the excellent microstructure and increased TPB. The LSCF–SDC core–shell cathode was characterized by a polarization resistance of  $0.265 \Omega \text{ cm}^2$  at  $650^\circ\text{C}$  and long-term operational stability during both the 120 h electrochemical test and the 30 thermocycles between 100 and  $650^\circ\text{C}$  [424]. According to the data of [340], the LNF94-infiltrated LSCF composite cathode with the core–shell structure on the GDC10 electrolyte was characterized by the values of  $R_p$  equal to  $0.041 \Omega \text{ cm}^2$  and MPD, equal to  $1080 \text{ mW cm}^{-2}$  at  $800^\circ\text{C}$ , and the excellent long-term stability in  $\text{CO}_2$  and Cr-containing atmospheres. The authors [340] showed that it was the heterogeneous electrode interface that significantly increased the electron conductivity and the oxygen dissociation.

Wang et al. [433] proposed a novel core–shell LSCF-based perovskite structured electrocatalyst covered with Ruddlesden–Popper phase  $\text{La}_{0.6}\text{Sr}_{1.4}\text{Co}_{0.2}\text{Fe}_{0.8}\text{O}_{4-\delta}$  ( $\text{LSCF}_{214}$ ) thin film. To form a local  $\text{LSCF}_{214}$  structure on the LSCF particles,  $\text{Sr}(\text{NO}_3)_2$  was added to the suspension of LSCF particles simultaneously with urea as a complexing agent. After suspension evaporation on a hot plate, a uniform  $\text{Sr}^{2+}$  coated LSCF particle precursor was obtained, which was finally calcined at  $800^\circ\text{C}$ . The core–shell electrode formed by screen-printing followed by sintering at  $900^\circ\text{C}$ , 2 h on the SDC electrolyte demonstrated a lower polarization resistance ( $0.17 \Omega \text{ cm}^2$ ) than the LSCF electrode ( $0.32 \Omega \text{ cm}^2$ ) at  $650^\circ\text{C}$ . The MPD values obtained for the anode-supported cell with the thin-film SDC electrolyte and the core–shell and conventional LSCF electrodes were  $0.57$  and  $0.3 \text{ W cm}^{-2}$  at  $650^\circ\text{C}$ , respectively. Moreover, the core–shell electrode showed a low degradation rate in the long-term test at  $600^\circ\text{C}$ . The ASR values at 0, 100, 200, 300 and 400 h were  $0.58$ ,  $0.77$ ,  $0.84$ ,  $0.85$  and  $0.82 \Omega \text{ cm}^2$ , respectively.

In summary, the preparation of the composite electrodes, aimed at increasing the TPB by improving the oxygen ion migration, remains the most demanded strategy to enhance the electrochemical performance of the traditional perovskite electrodes. However, the latest composite fabrication techniques use nanostructured materials to provide an increased electrode interface.

#### 4.3. Improvement of the Electrode Surface

The effective approach to increase the electrochemical activity of the conventional perovskite electrodes by increasing the TPB is related to the preparation of decorated electrodes by the infiltration (also called impregnation) method, where the porous cathode is filled with various additives [148,163,304,323,340,382,403,434–438] as well as decorating the electrode surface with nanocatalysts [141,154,315,387,405,416,426,439] and nanocoatings [303,308,341,342], which significantly improve the electrode surface diffusion and exchange with the gas phase.

The enhancement of the electrochemical performance of  $(\text{La}_{0.8}\text{Sr}_{0.2})_{0.95}\text{MnO}_{3-\delta}$  ((LSM20<sub>0.95</sub>)–YSZ cathodes by infiltrating salt solutions was reported in [382]. The developed 50LSM20<sub>0.95</sub>–50YSZ cathodes were characterized by the reduction of the high-frequency polarization resistance up to 45% of the baseline ( $R_{p(\text{hf})} = 1.06 \Omega \text{ cm}^2$  at  $700^\circ\text{C}$  for the YSZ infiltrated electrode), and the low-frequency polarization resistance up to 28% of the baseline ( $R_{p(\text{lf})} = 0.57 \Omega \text{ cm}^2$  at  $700^\circ\text{C}$  for the ammonium chloride infiltrated electrode).

According to Zhang et al. [304] and Han et al. [305], the reversible cell with the LSM20–YSZ air electrode infiltrated with  $\text{SrTi}_{0.3}\text{Fe}_{0.6}\text{Co}_{0.1}\text{O}_{3-\delta}$  (STFC), the YSZ electrolyte, and the  $\text{SrTi}_{0.3}\text{Fe}_{0.7}\text{O}_{3-\delta}$  fuel electrode showed the improved power performance using different fuel gases. The STFC infiltration allowed for an increase in the peak power density of the solid oxide cell in the fuel mode by >1.5 times, up to  $0.88 \text{ W cm}^{-2}$  and  $1.37 \text{ W cm}^{-2}$  using air and oxygen as an oxidizer, respectively [304], and up to  $0.9 \text{ W cm}^{-2}$  and  $0.68 \text{ W cm}^{-2}$  using wet  $\text{H}_2$  and wet  $\text{CO}$  as a fuel, respectively [305], at  $800^\circ\text{C}$ .

Wu et al. [148], who investigated the influence of the infiltration process on the morphology and performance of the LSM electrode (electrode schemes are presented in Figure 9), showed that the electrochemical characteristics of the LSM–SDC electrodes infiltrated with  $\text{Sm}_{0.5}\text{Sr}_{0.5}\text{CoO}_{3-\delta}$  (SSC) and the LSM–SSC electrodes infiltrated with

SDC (LSM–SSC–SDC) were dependent on the infiltration time. It was shown that as the infiltration time increased, the cathode polarization resistance and overpotential decreased, and the single-cell peak power density improved. The  $R_p$  value for the LSM–SSC–SDC electrode was obtained as low as  $0.08 \Omega \text{ cm}^2$  at  $800 \text{ }^\circ\text{C}$  compared to  $2.38 \Omega \text{ cm}^2$  at  $800 \text{ }^\circ\text{C}$  for the LSM electrode.

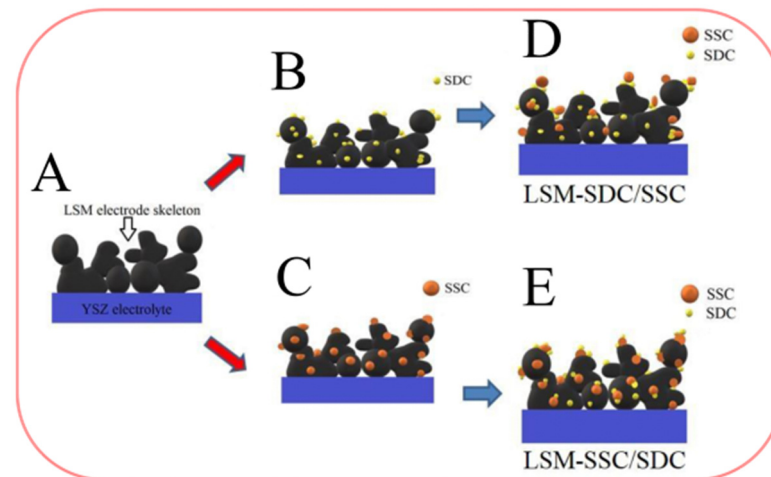


**Figure 9.** The schemes for the alternate infiltration: LSM electrode (A), SDC infiltrated LSM (B), SSC infiltrated LSM (C), SDC and SSC alternately infiltrated LSM (D), SSC and SDC alternately infiltrated LSM (E) (reproduced from [148] with permission of Elsevier).

Sun et al. in [154] developed the composite electrode for a protonic ceramic fuel cell based on  $(\text{LS})_{0.95}\text{M20}$  and BZY15 infiltrated with  $\text{Pr}_6\text{O}_{11}$  nanoparticles over four cycles. The polarization resistance of the  $(\text{LS})_{0.95}\text{M20}$ –BZY15 cathode on the BZY20 electrolyte, measured at  $600 \text{ }^\circ\text{C}$ , was equal to  $0.12 \Omega \text{ cm}^2$ , and the peak power density of the NiO–BZY20 | BZY20 | LSM–BZY15– $\text{Pr}_6\text{O}_{11}$  single cell reached  $0.28 \text{ W cm}^{-2}$  at  $600 \text{ }^\circ\text{C}$ . The long-term stability tests showed that the obtained cathode was stable at  $600 \text{ }^\circ\text{C}$  for 100 h. The results of the work [154] demonstrated that the infiltration technique, which ultimately led to the TPB extension, is a highly effective strategy to improve the electrochemical activity of conventional LSM–YSZ cathodes by enhancing the oxygen adsorption, dissociation, and diffusion processes.

In [387], the possibility of using the low-cost mixed metal  $\text{LnO}_x$  ( $\text{Ln} = \text{Ce}, \text{La}, \text{Nd}, \text{Pr}, \text{Sm}$ ) as an ionic conductor in an air nanostructured electrode was demonstrated, and the  $R_p$  value, equal to  $0.04 \Omega \text{ cm}^2$  at  $800 \text{ }^\circ\text{C}$ , was measured for the composite electrode of praseodymium oxide-modified  $60\text{LSM20}$ – $40\text{LnO}_x$ . The influence of the cerium, praseodymium or manganese oxide infiltration on the electrochemical performance of the  $80(\text{LS})_{0.95}\text{M20}$ – $20\text{YSZ}$  electrodes was investigated in [306]. It was shown that the infiltration of oxide nanoparticles significantly increased the electrochemical performance of LSM–YSZ: infiltration of  $\text{PrO}_x$  resulted in a polarization resistance value of  $0.068 \Omega \text{ cm}^2$  at  $700 \text{ }^\circ\text{C}$ .

Seyed-Vakili et al. [405] investigated the effect of co-infiltration with metallic (Ag) and ceramic ( $\text{La}_{0.8}\text{Sr}_{0.2}\text{FeO}_3$  (LSF20),  $\text{CeO}_2$ ) precursors on the performance of the LSM cathode on the YSZ substrate. It was shown that the introduction of Ag and ceria reduced the polarization resistance down to  $0.64 \Omega \text{ cm}^2$  at  $800 \text{ }^\circ\text{C}$ , which was 2.5% lower than that of the pristine LSM electrode, while the infiltration of Ag solution reduced the electrode overpotential by approximately 114%.

The results of the study [303] showed that the enhancement of the LSM20–YSZ electrode activity can be achieved by using a nanocoating consisting of the dual (CoOx, Pt) nanocatalyst. The polarization resistance values for the electrodes without and with deposited nanocatalysts were equal to  $0.66$  and  $0.31 \Omega \text{ cm}^2$  at  $750 \text{ }^\circ\text{C}$ , respectively. In addition, the long-term operation of the NiO–YSZ | YSZ | LSM20–YSZ single cell at  $750 \text{ }^\circ\text{C}$  showed that the use of the nanocoating resulted in an increase in the MPD value of almost 200%.

The improved electrochemical performance of the LSM20 cathode on the YSZ electrolyte substrate was achieved by depositing the nanocrystalline YSZ interlayer at the LSM/YSZ interface using an infiltration process [308]. The LSM–YSZ infiltrated cathode showed a reduced polarization resistance value of  $0.11 \Omega \text{ cm}^2$  compared to  $0.35 \Omega \text{ cm}^2$  for the LSM infiltrated cathode (at  $750^\circ\text{C}$ ). In addition, the single cell NiO–YSZ | YSZ | LSM20 with the nanocrystalline YSZ interlayer was characterized by the increased peak power density at  $750^\circ\text{C}$ , equal to  $1.54 \text{ W cm}^{-2}$ , compared to the value of  $0.76 \text{ W cm}^{-2}$  for the cell without the YSZ interlayer. The single cell based on the LSM–YSZ infiltrated cathode showed long-term stability at  $750^\circ\text{C}$  for 300 h at a current density of  $0.5 \text{ A cm}^{-2}$ . Koo et al. attributed the improved oxygen reduction kinetics to the increased TPB on the infiltrated YSZ interlayer, which increased the number of reaction sites with a low reaction barrier [308].

The LSCF–GDC10 composite electrodes decorated with CuO nanoparticles were prepared by the infiltration technique in [416]. The results of the high-temperature X-ray diffraction study indicated the formation of a new Cu-containing LSCF-based compound. The polarization resistance of the LSCF–GDC10 cathode on the GDC10 substrate decreased significantly from  $0.62 \Omega \text{ cm}^2$  to  $0.32 \Omega \text{ cm}^2$  at  $650^\circ\text{C}$  for the bare and infiltrated electrodes, respectively. Gao et al. concluded that the electrode improvement was due to the  $\text{Cu}^{2+}$  reduction at the LSCF–GDC10/CuO interface. Meanwhile, a slight degradation in the performance of the infiltrated samples was observed during the ageing tests at  $500^\circ\text{C}$  and  $650^\circ\text{C}$  for 150 h in air. The authors of [416] attributed the electrode degradation to the coarsening of the CuO particles, the Sr segregation and the low stability of Cu-containing impurities formed at the interface.

The 50LSCF–50Er<sub>0.4</sub>Bi<sub>1.6</sub>O<sub>3</sub> (ESB) composite cathode prepared by infiltration using organic solvents in [323] showed the excellent electrochemical performance with the SDC electrolyte, equal to  $0.11 \Omega \text{ cm}^2$  at  $700^\circ\text{C}$ , compared to  $0.27 \Omega \text{ cm}^2$  at  $700^\circ\text{C}$  for the LSCF cathode. It was also found that this value was the best performance for the LSCF infiltrated electrodes reported in the literature, such as LSCF–Ce(Ag) [315], LSCF–(Pr,Ni,Mn)O [341], LSCF–Pd [439], LSCF–LSM [403], LSCF–SDC [425], LSCF–SDC–CuO [416], LSCF–SDC–Ag [426], LSCF–GDC10 [417,418]. The NiO–SDC | SDC | LSCF–ESB single cell fuelled with wet hydrogen, characterized by an MPD value of  $469 \text{ mW cm}^{-2}$  at  $700^\circ\text{C}$  had a good short-term stability for 50 h at a current density of  $0.45 \text{ A cm}^{-2}$  [323]. Wang et al. concluded that the ESB additive had changed the rate-limiting electrode process from the charge transfer to the oxygen diffusion on the cathode surface.

Shi et al. [341] reported on the enhanced electrochemical activity of the LSCF cathode by coating a thin film of (Pr,Ni,Mn)O (PNM5) oxide using an infiltration method. According to the XRD and SEM data, the PNM5 thin film coating, which consisted of a mixture of the Pr<sub>6</sub>O<sub>11</sub>, PrNiO<sub>3</sub>, MnO and NiO oxides, have formed the small particles on the surface of the LSCF backbone particles. The EIS data showed that the PNM5-infiltrated LSCF cathode on the GDC substrate exhibited  $R_p = 0.388 \Omega \text{ cm}^2$  at  $700^\circ\text{C}$  compared to  $R_p = 1.166 \Omega \text{ cm}^2$  for the bare LSCF cathode. The MPD values of the NiO–DC | GDC | LSCF single cells were equal to 241 and  $580 \text{ mW cm}^{-2}$  at  $750^\circ\text{C}$  for the cells with the bare and infiltrated LSCF cathodes, respectively. The degradation rates of the above cells were measured to be 0.07093% and 0.02168 at  $750^\circ\text{C}$  during 200 h, respectively. Distribution of Relaxation Times (DRT) function analysis confirmed that the PNM5 coating significantly improved the ORR on the LSCF electrode surface.

Thus, the literature data presented confirm that the infiltration technique is currently the most advanced method for producing active air electrodes with enhanced surface properties.

#### 4.4. Improvement of the Electrode–Electrolyte Interface

An advanced air electrode may consist of several layers, each of which has specific requirements. For a functional layer (FL), which is close to the interface with the electrolyte, it is important to have the thermo-mechanical properties (CTE value) close to those

of the electrolyte substrate with no chemical interaction with the electrolyte, and high electrochemical activity.

It is known that the electrical conductivity of LSM-based composite layers decreases significantly with increasing electrolyte content [440], so it is necessary to form a collector layer (CL) with high electronic conductivity to ensure uniform current distribution over the electrode volume and to organize a stable current capacity. Therefore, noble metals have been used as the collectors for the composite electrodes: platinum in [149,198,377], and silver in [441]. The oxide electrode collectors with LSM were used in [149,151,387,442] (LSM40), in [205] (LSM30), [442]  $\text{La}_{0.65}\text{Sr}_{0.3}\text{MnO}_{3-\delta}$  ( $\text{L}_{0.65}\text{SM30}$ ) and in [303,443] (LSM20), [442]  $(\text{LS})_{0.98}\text{M20}$ .

Harboe et al. [205] investigated the microstructure and electrochemical activity of the  $\text{L}_{0.65}\text{SM30}$ –YSZ–graphite–rice starch electrodes with the LSM collector with different compositions in a symmetrical YSZ electrolyte-supported cell. The results obtained showed that the application of the double  $\text{L}_{0.65}\text{SM30}$ –YSZ–rice starch electrode combinations with the LSM30 current collector, sintered at 1150 °C, showed the best electrochemical performance of the cathode, equal to 0.26  $\Omega \text{ cm}^2$  at 800 °C.

In [379] the effect of the configuration of the electrode based on LSM20–YSZ on its performance was investigated. The electrode with an area of 25 mm<sup>2</sup> was formed by screen printing and annealed at 1200 °C for 2 h. Three electrode configurations were studied: monolayer 80LSM20–20YSZ electrode (the mass ratio of the components in the electrode is shown); bilayer electrode with FL 80LSM20–20YSZ and CL LSM20; triple-layer electrode with FL 60LSM20–40YSZ, interlayer 80LSM20–20YSZ and CL LSM20, as shown in Figure 10a. Scanning electron microscopy showed the absence of any defects at the interfaces between the composite cathode and the electrolyte, and between the different cathode layers for the triple-layer electrode, which was ensured by the gradual change in CTE (Figure 10b). The thickness of each cathode layer was approximately 5–6  $\mu\text{m}$ . The polarization resistances for the above electrode configurations were 0.32, 0.24 and 0.18  $\Omega \text{ cm}^2$  at 800 °C, respectively. Maximum values of current density (0.77 A cm<sup>-2</sup> at an overvoltage of 0.1 V at 800 °C) and specific power of a single SOFC (447 mW cm<sup>-2</sup> compared to 220 mW cm<sup>-2</sup> for the single-layer electrode) were obtained for the triple-layer electrode.

Gradient composite electrodes based on  $\text{La}_{0.72}\text{Sr}_{0.18}\text{MnO}_{3-\delta}$  (LSM18), LSCF, GDC were prepared by sol–gel slurry deposition [199]. The polarization resistance values for the 50LSM18–50GDC cathode with the 25LSM18–25LSCF–50GDC and 50LSCF–50GDC interlayers, and the LSCF collector layer (Figure 10c,d), sintered at 900 °C on the YSZ substrate, were equal to 0.21 and 0.10  $\Omega \text{ cm}^2$  at 700 and 800 °C, respectively.

Tian et al. [307] fabricated the double-layer electrode LSM35–LSCF with the LSCF top layer infiltrated with SDC, the polarization resistance of which decreased by a factor of 3 times at 800 °C compared to the single-layer LSM electrode. The single fuel cell with the above-fabricated air electrode had an MPD value of 671 mW cm<sup>-2</sup> at 800 °C, which was 5 times higher than that of the bare LSM cell. The electrolysis cell with the LSM35–LSCF air electrode was characterized by the hydrogen production rate of 547.58 mL cm<sup>-2</sup> h<sup>-1</sup> at 800 °C under 1.5 V, which was three times higher than that of the LSM air electrode. The results obtained in [307] justified that the formation of the double-layer air electrodes, whose functional layers consist of both LSCF and LSM, is a promising strategy for enhancing the oxygen reaction reduction and could be useful for the improvement of fuel cells and electrolysis cells.

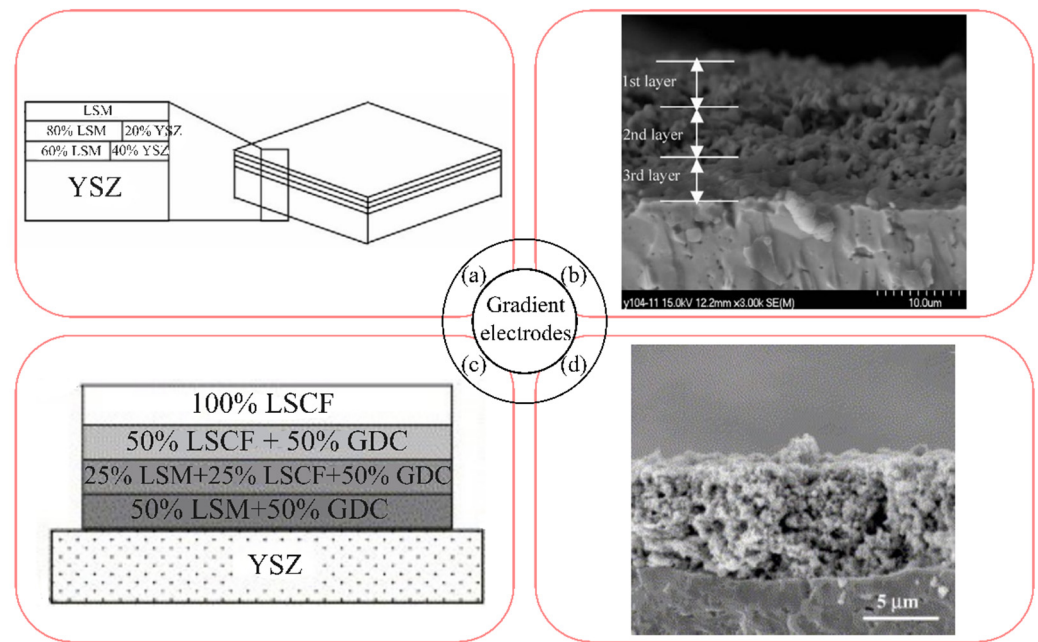


**Figure 10.** Examples of functional-layer electrodes based on LSM: (a) scheme and (b) SEM micrograph of three-layer electrode with 60LSM20–40YSZ functional layer, 80LSM20–20YSZ interlayer and LSM20 collector layer (1200 °C, 2 h), obtained by screen printing [379]; (c) scheme and (d) SEM micrograph of four-layer electrode with 50LSM18–50GDC functional layer, 25LSM18–25LSCF–50GDC and 50LSCF–50GDC interlayers and LSCF collector layer (900 °C, 2 h), obtained by sol–gel slurry deposition ((a,b) are reproduced from [379] with permission of Springer; (c,d) are reproduced from [199] with the permission of Elsevier).

The addition of  $\text{La}_{0.8}\text{Sr}_{0.2}\text{FeO}_{3-\delta}$  (LSF) into the double functional layer and infiltration were simultaneously used in [444] to fabricate the LSCF–LSF–YSZ composite cathode. Layers of LSF and LSCF were sequentially deposited on the YSZ scaffold with LSF as a protective layer between LSCF and YSZ. The  $R_p$  values of the symmetrical cells with the LSF- and LSCF–LSF-based cathodes were equal to 0.72 and 0.19  $\Omega \text{ cm}^2$  at 700 °C, respectively. The MPD values of the single cells with the LSCF–LSF–YSZ and LSF–YSZ cathodes were measured to be 1277 and 922  $\text{mW cm}^{-2}$  at 700 °C, respectively. The results obtained showed that the use of the LSF protective layer could be applied to the adoption of the LSCF air electrode for use in YSZ-based cells without  $\text{CeO}_2$ -based buffer layers.

The study on the effect of the thickness of FL and CL of the LSCF-based double-layer electrode on its polarization resistance in contact with the GDC10 electrolyte showed that the optimum FL was almost 5  $\mu\text{m}$ -thick, while the optimum CL thickness reached 30  $\mu\text{m}$  [445]. For the symmetrical cell with the optimum thickness cathode layers the excellent  $R_p$  value was measured to be 0.021  $\Omega \text{ cm}^2$  at 650 °C.

Lee et al. [186] prepared the LSCF–BCZY15 composite cathode with gradient porosity by a slurry deposition method for use in PCFCs with the BCZY15 electrolyte. The gradient composite cathodes were prepared in such a way that the cathode porosity and cathode powder size increased significantly in the opposite direction from the electrode–electrolyte interface. The polarization resistances of the symmetrical cells with the porosity gradient and the conventional LSCF–BCZY15 composite cathodes were 0.19 and 0.22  $\Omega \text{ cm}^2$  at 700 °C, respectively. The MPD values of the NiO–BCZY15 | BCZY15 | LSCF–BCZY15 single cells with the porosity gradient and the conventional cathodes were 367 and 352  $\text{mW cm}^{-2}$  at 700 °C, respectively. In addition, the cell with the porosity gradient cathode showed excellent 100 h stability at 700 °C with a degradation rate of no more than 2%. The authors [186] concluded that it was the gradient structure of the composite cathode that

prevented the degradation of the cell performance and stabilized the long-term durability by improving the oxygen adsorption and oxygen reduction at the TPBs.

A numerical simulation of the microstructure of the porosity gradient electrodes was presented in [115]. A “multi-sphere” discrete element method was used to model the powder packing, a kinetic Monte Carlo method was used to model the powder sintering, and the lattice Boltzmann method was used to model the electrochemical reaction at the cathode. It was found that the best performance of the cathode was achieved for the cathode design with a thickness of 25  $\mu\text{m}$  and a density range of 40–65%, which suppressed the sintering but improved the thermal stability of the electrode.

The sintering conditions of the electrode affect the microstructure, adhesion of the electrode to the electrolyte and the possible electrode–electrolyte interdiffusion and chemical interaction, and are, therefore, the most important parameters of the electrode formation.

In [380], the effect of sintering conditions on the performance of electrodes with a  $50(\text{LS})_{0.95}\text{M}25\text{--}50\text{YSZ}$  functional layer and an  $(\text{LS})_{0.95}\text{M}25$  collector was investigated. Electrodes annealed in the temperature range 1150–1300  $^{\circ}\text{C}$  were studied, with the thickness of the FL varying in the range of 4–14  $\mu\text{m}$ , and the collector layer 15–85  $\mu\text{m}$ . Reducing the sintering temperature of the FL resulted in a more porous structure with smaller pores and particles, which reduced the polarization resistance. When the sintering temperature of the FL was kept constant at 1300  $^{\circ}\text{C}$ , a reduction in the annealing temperature of the collector also resulted in a reduction in the polarization resistance. The minimum values of the polarization and contact resistances (0.03 and 0.17  $\Omega\text{ cm}^2$  at 1000  $^{\circ}\text{C}$ , respectively) were obtained for the 13  $\mu\text{m}$  thick FL electrode annealed at 1150  $^{\circ}\text{C}$  and the 80  $\mu\text{m}$  thick CL electrode annealed at 1150  $^{\circ}\text{C}$ .

A comparative study to investigate the effect of sintering temperature on the functional properties of  $(\text{LS})_{0.95}\text{M}20\text{--}\text{YSZ}$  and  $(\text{LS})_{0.95}\text{CF}\text{--}\text{YSZ}$  composites prepared as hollow fibers in the range of 1250–1450  $^{\circ}\text{C}$  was presented in [241]. For LSCF–YSZ, the formation of the pyrochlore structured impurity phase was observed at the sintering temperature of 1300  $^{\circ}\text{C}$ , followed by the degradation of the perovskite phase at 1400  $^{\circ}\text{C}$ . In contrast, LSM–YSZ showed high thermal stability. It was shown that the highest porosity (34.57% and 33.32% for LSM–YSZ and LSCF–YSZ, respectively) was obtained after sintering at the temperature of 1250  $^{\circ}\text{C}$ , and with the increasing sintering temperature, the porosity and gas permeability of both composites decreased significantly. The mechanical strength of the composites (which is an important property for the cathode-supported SOFCs) was improved by increasing the sintering temperature. For the two composites sintered at 1400  $^{\circ}\text{C}$  and with a sufficient porosity of 22%, the mechanical strength was measured to be 161 and 114 MPa for LSM–YSZ and LSCF–YSZ, respectively. Thus, Ab Rahman et al. [241] concluded that the LSM–YSZ composite cathode was more noticeable at high sintering temperatures compared to the LSCF–YSZ due to its thermal and chemical stability, optimum values of the mechanical strength, gas permeability, and porosity.

The effect of sintering temperature on the performance of the LSCF-based composite cathodes in PCFCs was investigated in [177]. It was shown, that the ohmic and polarization resistances of the LSCF–BZYb composite cathodes on the BZYb electrolyte decreased from 0.76 to 0.45, and from 2.43 to 0.73  $\Omega\text{ cm}^2$  at 600  $^{\circ}\text{C}$  for the electrodes sintered at 900 and 1100  $^{\circ}\text{C}$ , respectively. The power densities of the fabricated PCFCs with the LSCF–BZYb composite cathodes sintered at 900 and 1100  $^{\circ}\text{C}$  were equal to 120 and 250  $\text{mW cm}^{-2}$  at 600  $^{\circ}\text{C}$ , respectively. Watanabe et al. [177] suggested that a better performance of the electrodes sintered at higher temperatures was due to the improved adhesion at the cathode–electrolyte interface, resulting in an increased number and thickness of the BZYb proton conducting paths within the composite cathodes.

In addition, well-known problems with air electrode delamination [446–448] were partially solved by introducing a porous electrolyte layer at the LSM electrode/YSZ dense electrolyte interface [372,384] or by forming nanostructured or contact layers at the LSCF/YSZ interface [449,450]. The flash co-sintering technique was used to form of the LSCF nanofiber coating on the GDC substrate [451] as a possible solution to the electrode delamination

problem. The experimental and modeling results showed that severe cracking was observed when the LSCF layer was connected to the electrode. When the LSCF layer was electrically isolated from the electrode, the temperature gradient was dropped. It was concluded that the optimum LSCF/SDC bilayer structure for use in SOFCs would be maintained if the GDC layer density of 92.86% and the LSCF layer porosity of 52.26% were achieved.

He et al. applied the numerical simulation using level-set and adjoint methods to optimize the porous LSCF microstructure [452–454]. It was shown that the spherical LSCF solid particles were preferable for performance improvement [452]. In [454], the LSCF/GDC10 electrode–electrolyte interface was numerically modelled using the adjoint method, and it was concluded from the calculation results that the cathode with the optimized electrode–electrolyte interface (optimized electrolyte volume fraction along the cathode thickness direction) had higher electrochemical activity compared to the flat electrode–electrolyte interface.

Thus, the data presented in this section show that the improvement of the perovskite electrode–electrolyte interface aimed at improving the processes occurring in TPBs includes the techniques of the gradient electrode fabrication, the use of collector layers, and the application of the optimum sintering temperature.

## 5. Modeling of the Electrode Performance

The data presented in the above paragraphs justify a greater number of experimental studies to improve the electrochemical performance of the conventional perovskite electrodes. Meanwhile, the high cost of the fuel and electrochemical cell elements and the time required for the investigations have led to the attempts to develop the mathematical models of the electrode performance and to perform 3D reconstruction of solid oxide cells with LSM- and LSCF-based electrodes using computational studies and an Artificial Intelligence (AI) technique. The computational modeling allows the analysis of key parameters that influence the electrochemical activity of the air electrodes.

In [309], Zhang et al. combined the super-resolution of a two-dimensional micrograph with the distribution of relaxation times (DRT) analysis data, showed that the active TPB was the key factor responsible for the LSM–YSZ infiltrated electrode activity, which monitored the electrochemical process at a high frequency. The authors of [309] presented the prospective strategy for modeling three-dimensional heterogeneous nanostructures from two-dimensional graphical data, and proposed an approach for correlating between functional properties of nanostructured electrodes. Sharma et al. [455] simulated a button cell based on a NiO–YSZ fuel electrode, YSZ electrolyte, and LSM air electrode. Electrochemical model equations (Fick’s model, Butler–Volmer equation, Ohm’s law used to estimate the values of concentration, activation, and ohmic overpotential losses, correspondingly) implemented in MATLAB software allowed the overall performance of the cell to be predicted by varying the fuel gas composition, operating temperature, electrolyte thickness and cell configuration. The authors believe that the mathematical model developed in [455] could be a prospect for the future design of solid oxide cells.

Yang et al. [456], for the first time, applied a calibrated multiphysics simulation with a multistep ORR model and structural coarsening data from a phase field study to investigate the degradation of the LSM–YSZ composite cathode performance. The multistep oxygen reduction reaction mechanism was considered to involve parallel surface (3PB) and bulk (2PB) pathways (Figure 11a,b). Multiphysical processes, such as charge conservation, gas transport through porous media and surface/bulk transport in the solid phase, were considered. The numerical simulation with a multistep ORR mechanism was simultaneously calibrated with DC polarization curves and AC impedance behavior for different air/fuel supply conditions. The structural changes were found to be sensitive to the volume fraction of LSM in the composite (Figure 11c). The degradation due to grain coarsening in the composite cathode was mainly due to the reduction of active sites for surface and bulk charge transfer steps with a change in the contributions of the 3PB (bulk) and 2PB (surface) pathways (Figure 11d). The simulation results were in good

agreement with the experimental investigation of the degradation kinetics of the LSM–YSZ cathode performance carried out using combined isotope exchange, EIS and microstructural study [457].

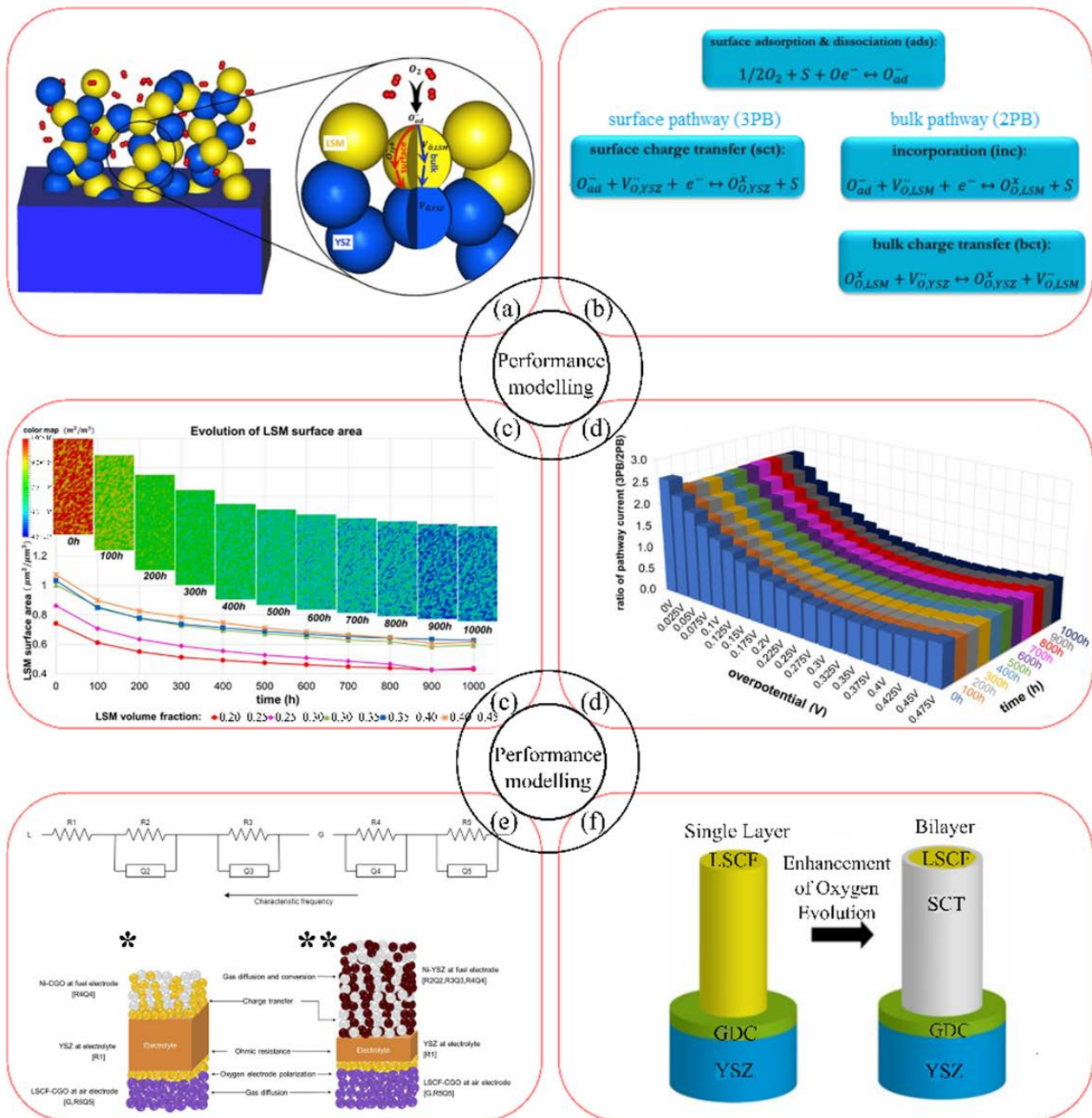


**Figure 11.** Modeling the degradation of the LSM–YSZ cathode (a); 3PB (surface) and 2PB (bulk) pathways of the electrode reaction for LSM–YSZ cathodes (b); the predicted evolution trend of the LSM/air interface, where surface adsorption and dissociation steps occur (c); the changes in the contributions of the 3PB and 2PB pathways due to structural degradation (d); Equivalent Circuit Model for the fit of the impedance data and their attribution to each layer for electrolyte-supported (\*) and anode-supported (\*\*) cells with LSCF cathode (e); single and bilayer LSCF-based electrode configurations (f) ((a–d) are reproduced from [456]; (e) is reproduced from [116], (f) is reproduced from [458]).

The numerical simulation of the influence of microstructural characteristics, such as particle size and porosity, on the electrochemical performance of LSCF-based cathodes was

provided by the He's group [459,460]. In [459], it was predicted that the best performance of the LSCF cathode was observed at a porosity of 0.40, and the cathode performance decreased sharply at a critical porosity of 0.10–0.25 due to pore blockage. It was also shown that the LSCF cathodes with the smaller mean pore size could be active at the low porosity of 0.10. In [460], the 3D microstructure of the LSCF–GDC cathode was constructed and the influence of the GDC pillars inside the bare LSCF and composite cathodes with different particle sizes was studied. The results obtained showed that the GDC fibers improved the performance of the LSCF cathode and were more effective in the cathode microstructures with smaller particle sizes.

The prediction of the performance characteristics for the YSZ electrolyte-supported single cell with NiO–SDC as the composite anode and LSCF as the cathode was provided in [461] using a Support Vector Machine (SVM) machine learning technique. The key SOFC parameters, such as the temperature and the supply voltage, were input into the computational model and the values of current density and the MPD values were the output parameters, corresponding to  $1160 \text{ mA cm}^{-2}$  and  $225 \text{ mW cm}^{-2}$  at  $800 \text{ }^\circ\text{C}$ , respectively. The prepared NiO–SDC | YSZ | LSCF single cell with hydrogen as fuel showed the values of peak current and power density equal to  $1170 \text{ mA cm}^{-2}$  and  $227 \text{ mW cm}^{-2}$  at  $800 \text{ }^\circ\text{C}$ , respectively, which showed the closeness of the theoretically predicted and research data [461].

The experimental and theoretical approaches to identify the contributions of the different cell components were applied in [116] using EIS and a 2D simulation tool for the anode-supported NiO–YSZ | YSZ | LSCF–GDC10 and electrolyte-supported NiO–CGO | YSZ | LSCF–GDC10 planar cells (Figure 11e). It was found that in the electrolyte-supported cell, the largest contribution to the total cell resistance was ohmic due to the greater thickness of the electrolyte layer compared to the anode-supported cell. The major contribution to the total cell resistance of the anode-supported cell was due to the activation overpotential, which was three times higher than that of the electrolyte-supported cell. Gas diffusion was negligible in all tests with the electrolyte-supported cell, in contrast to its large influence in the anode-supported cell. In addition, temperature had a greater influence in the anode-supported cell due to the higher values of the activation energy for the ohmic and activation losses. As the current density increased, the contribution to the activation resistance decreased in both cells studied. Padinjarethil et al. [116] considered that the same work, if improved by introducing the effect of time on the kinetic parameters, could be useful for predicting the long-term operation of SOFCs. The influence of temperature, concentration, and current density gradients within and along the cell structure on the performance of the NiO–cermet anode-supported single cell was evaluated in [462] using a calibration model. The results obtained for the cell in a steady state showed the strong role of the temperature gradients along the channel and the mass transport processes at the gas/electrode interface.

The 1D and 2D models for the LSCF cathode degradation due to sulfur poisoning were developed numerically in [463]. The 1D model viewed a barrier layer formed on the LSCF surface with a random distribution of sulfur content in the thickness direction. The above 1D model was fed to the 2D model of the anode-supported single cell under sulfur poisoning. The results obtained for the 2D simulation model of the planar SOFC showed that it was the model that correctly predicted the  $\text{SrSO}_4$  formation near the cathode–electrolyte interface in the region of the air channel. Iwai et al. concluded that the model proposed in [463] could be used to improve the LSCF cathode by considering the poisoning rate as a function of the barrier thickness.

Modelling of the electrochemical reactions occurring at 2PBs and 3PBs of the single layer  $\text{La}_{0.6}\text{Sr}_{0.4}\text{Co}_{0.4}\text{Fe}_{0.6}\text{O}_{3-\delta}$  (LSCF60) and bilayer LSCF60/SCT (strontium cobalt tantalum oxide) air electrodes in a solid oxide electrolysis cell with the YSZ electrolyte and GDC10 buffer layer provided in [458] (as shown in Figure 11f) revealed a competition in electrode kinetics between 2PBs and 3PBs. However, 3PBs were the preferred reactive sites for the single-layer LSCF60 electrode at high voltages. The application of the SCT layer increased the activity of 2PBs, thus reducing the oxygen stoichiometry and dimensional

changes. The authors of [458] considered that the analog strategy would be used to prevent delamination at the electrode–electrolyte interface. In addition, the cyclic voltammetry (CV) response of the porous LSCF electrode was simulated in [464], considering the models of solid-state diffusion coupled with oxygen exchange (model-I) and a detailed description of the reaction mechanism (model-II). It was shown that the peaks of the voltammograms were due to the change in oxygen stoichiometry governed by both oxygen diffusion and oxygen exchange, and model-I satisfactorily described the CV curves when the  $k_{\text{chem}}$  constant was determined far from equilibrium. Meanwhile, model II adequately explained the shape of the voltammograms due to the passivation and decomposition of the LSCF surface.

## 6. Conclusions

In the present review, the established and novel methods for modifying conventional air electrodes with perovskite structure were discussed, such as lanthanum strontium manganite  $\text{La}_{1-x}\text{Sr}_x\text{MnO}_{3-\delta}$  (LSM) and lanthanum strontium cobaltite ferrite  $\text{La}_{0.6}\text{Sr}_{0.4}\text{Co}_{0.8}\text{Fe}_{0.2}\text{O}_{3-\delta}$  (LSCF), with particular emphasis on the selection of the optimal electrode material composition, electrode layer design, progressive synthesis and deposition methods, and electrode activation techniques. In addition to the creation of defects as the most suitable way to increase the chemical stability of the materials, the development of high-entropy oxides based on LSM and LSCF containing at least five co-dopants was noted. Ceramic methods such as screen printing, tape casting and spraying were found to be the most technologically simple and easily scalable electrode fabrication methods. Spray pyrolysis in its different modifications, along with electrospinning, template method, and 3D printing were mentioned among the variety of methods available to improve the conventional perovskite electrodes by extending TPB. The deposition of protective and non-catalytic layers on the electrode surface was proposed as a solution to the problems of segregation, impurity poisoning and sluggish oxygen kinetics.

New trends in the design of the LSM- and LSCF-based composite electrodes were highlighted, including various infiltration techniques, modification of the electrode structure using nanofibers and the creation of core–shell structures. The selection of the optimum sintering temperature, the creation of the electrodes with gradient composition and porosity and the use of collector layers were shown to be important in improving the perovskite electrode–electrolyte interface, preventing electrode delamination, and ensuring stable current collection.

It was shown that computational design and numerical simulations of the perovskite-based composite allowed us to suggest possible degradation mechanisms and to understand the electrode behavior at both atomic and macroscopic scales. These methods were found to be useful for quickly analyzing key parameters that influence the electrochemical activity of the air electrodes and for predicting the durability of the electrode without time-consuming experimental work. The development of the mathematical models was shown to be promising for the future design of solid oxide cells.

The present review, which summarizes the basic information on the methods to improve the electrochemical performance of conventional air electrodes, can serve as a guide for the application of the developed technologies to the modification of electrodes with novel, recently investigated electrode materials.

**Author Contributions:** Conceptualization, E.F. and E.P.; writing—original draft preparation, E.F. and E.P.; writing—review and editing, E.F. and E.P.; data visualization, E.F.; funding acquisition, E.F. All authors have read and agreed to the published version of the manuscript.

**Funding:** The research funding from the Russian Science Foundation (agreement 23-23-00083) is gratefully acknowledged.

**Institutional Review Board Statement:** Not applicable.

**Informed Consent Statement:** Not applicable.

**Data Availability Statement:** Not applicable.

**Acknowledgments:** The authors thank Anastasia Ivanova and Polina Morozova for help with data visualization.

**Conflicts of Interest:** The authors declare no conflict of interest.

## References

1. Erixno, O.; Rahim, N.A.; Ramadhani, F.; Adzman, N.N. Energy Management of Renewable Energy-Based Combined Heat and Power Systems: A Review. *Sustain. Energy Technol. Assess.* **2022**, *51*, 101944. [\[CrossRef\]](#)
2. Iliiev, I.K.; Filimonova, A.A.; Chichirov, A.A.; Chichirova, N.D.; Pechenkin, A.V.; Vinogradov, A.S. Theoretical and Experimental Studies of Combined Heat and Power Systems with SOFCs. *Energies* **2023**, *16*, 1898. [\[CrossRef\]](#)
3. Lee, J.; Lin, K.-Y.A.; Jung, S.; Kwon, E.E. Hybrid Renewable Energy Systems Involving Thermochemical Conversion Process for Waste-to-Energy Strategy. *Chem. Eng. J.* **2023**, *452*, 139218. [\[CrossRef\]](#)
4. He, V.; Gaffuri, M.; Van Herle, J.; Schifffmann, J. Readiness Evaluation of SOFC-MGT Hybrid Systems with Carbon Capture for Distributed Combined Heat and Power. *Energy Convers. Manag.* **2023**, *278*, 116728. [\[CrossRef\]](#)
5. Wang, Y.; Cao, Q.; Liu, L.; Wu, Y.; Liu, H.; Gu, Z.; Zhu, C. A Review of Low and Zero Carbon Fuel Technologies: Achieving Ship Carbon Reduction Targets. *Sustain. Energy Technol. Assess.* **2022**, *54*, 102762. [\[CrossRef\]](#)
6. Maestre, V.M.; Ortiz, A.; Ortiz, I. Challenges and Prospects of Renewable Hydrogen-Based Strategies for Full Decarbonization of Stationary Power Applications. *Renew. Sustain. Energy Rev.* **2021**, *152*, 111628. [\[CrossRef\]](#)
7. Russo, M.A.; Carvalho, D.; Martins, N.; Monteiro, A. Forecasting the Inevitable: A Review on the Impacts of Climate Change on Renewable Energy Resources. *Sustain. Energy Technol. Assess.* **2022**, *52*, 102283. [\[CrossRef\]](#)
8. Shen, M. Solid Oxide Fuel Cell-Lithium Battery Hybrid Power Generation System Energy Management: A Review. *Int. J. Hydrogen Energy* **2021**, *46*, 32974–32994. [\[CrossRef\]](#)
9. Kumar, P.; Singh, O. A Review of Solid Oxide Fuel Cell Based Hybrid Cycles. *Int. J. Energy Res.* **2022**, *46*, 8560–8589. [\[CrossRef\]](#)
10. Feng, Y.; Qu, J.; Zhu, Y.; Wu, B.; Wu, Y.; Xiao, Z.; Liu, J. Progress and Prospect of the Novel Integrated SOFC-ICE Hybrid Power System: System Design, Mass and Heat Integration, System Optimization and Techno-Economic Analysis. *Energy Convers. Manag.* **2023**, *18*, 100350. [\[CrossRef\]](#)
11. Kasaeian, A.; Javidmehr, M.; Mirzaie, M.R.; Fereidooni, L. Integration of Solid Oxide Fuel Cells with Solar Energy Systems: A Review. *Appl. Therm. Eng.* **2023**, *224*, 120117. [\[CrossRef\]](#)
12. Singh, M.; Zappa, D.; Comini, E. Solid Oxide Fuel Cell: Decade of Progress, Future Perspectives and Challenges. *Int. J. Hydrogen Energy* **2021**, *46*, 27643–27674. [\[CrossRef\]](#)
13. Bilal Hanif, M.; Motola, M.; Qayyum, S.; Rauf, S.; Khalid, A.; Li, C.-J.; Li, C.-X. Recent Advancements, Doping Strategies and the Future Perspective of Perovskite-Based Solid Oxide Fuel Cells for Energy Conversion. *Chem. Eng. J.* **2022**, *428*, 132603. [\[CrossRef\]](#)
14. Hu, S.; Li, J.; Zeng, Y.; Pu, J.; Chi, B. A Mini Review of the Recent Progress of Electrode Materials for Low-Temperature Solid Oxide Fuel Cells. *Phys. Chem. Chem. Phys.* **2023**, *25*, 5926–5941. [\[CrossRef\]](#)
15. Tarutin, A.P.; Filonova, E.A.; Ricote, S.; Medvedev, D.A.; Shao, Z. Chemical Design of Oxygen Electrodes for Solid Oxide Electrochemical Cells: A Guide. *Sustain. Energy Technol. Assess.* **2023**, *57*, 103185. [\[CrossRef\]](#)
16. Md Harashid, M.A.; Chen, R.S.; Ahmad, S.H.; Ismail, A.F.; Baharuddin, N.A. Recent Advances in Electrode Material for Symmetrical Solid Oxide Fuel Cells and Way Forward Sustainability Based on Local Mineral Resources. *Int. J. Energy Res.* **2022**, *46*, 22188–22221. [\[CrossRef\]](#)
17. Tahir, N.N.M.; Baharuddin, N.A.; Samat, A.A.; Osman, N.; Somalu, M.R. A Review on Cathode Materials for Conventional and Proton-Conducting Solid Oxide Fuel Cells. *J. Alloys Compd.* **2022**, *894*, 162458. [\[CrossRef\]](#)
18. Zhang, M.; Du, Z.; Zhang, Y.; Zhao, H. Progress of Perovskites as Electrodes for Symmetrical Solid Oxide Fuel Cells. *ACS Appl. Energy Mater.* **2022**, *5*, 13081–13095. [\[CrossRef\]](#)
19. Pikalova, E.Y.; Kalinina, E.G.; Pikalova, N.S.; Filonova, E.A. High-Entropy Materials in SOFC Technology: Theoretical Foundations for Their Creation, Features of Synthesis, and Recent Achievements. *Materials* **2022**, *15*, 8783. [\[CrossRef\]](#)
20. Skutina, L.; Filonova, E.; Medvedev, D.; Maignan, A. Undoped Sr<sub>2</sub>MMoO<sub>6</sub> Double Perovskite Molybdates (M = Ni, Mg, Fe) as Promising Anode Materials for Solid Oxide Fuel Cells. *Materials* **2021**, *14*, 1715. [\[CrossRef\]](#)
21. Curi, M.; da Silva, E.R.; de Furtado, J.G.M.; Ferraz, H.C.; Secchi, A.R. Anodes for SOFC: Review of Material Selection, Interface and Electrochemical Phenomena. *Quim. Nova* **2021**, *44*, 86–97. [\[CrossRef\]](#)
22. Filonova, E.; Medvedev, D. Recent Progress in the Design, Characterisation and Application of LaAlO<sub>3</sub><sup>−</sup> and LaGaO<sub>3</sub>-Based Solid Oxide Fuel Cell Electrolytes. *Nanomaterials* **2022**, *12*, 1991. [\[CrossRef\]](#)
23. Kim, D.; Jeong, I.; Kim, K.J.; Bae, K.T.; Kim, D.; Koo, J.; Yu, H.; Lee, K.T. A Brief Review of Heterostructure Electrolytes for High-Performance Solid Oxide Fuel Cells at Reduced Temperatures. *J. Korean Ceram. Soc.* **2022**, *59*, 131–152. [\[CrossRef\]](#)
24. Hanif, M.B.; Rauf, S.; Motola, M.; Babar, Z.U.D.; Li, C.-J.; Li, C.-X. Recent Progress of Perovskite-Based Electrolyte Materials for Solid Oxide Fuel Cells and Performance Optimizing Strategies for Energy Storage Applications. *Mater. Res. Bull.* **2022**, *146*, 111612. [\[CrossRef\]](#)
25. Dey, S.; Chaudhary, S.; Parvatalu, D.; Mukhopadhyay, M.; Sharma, A.D.; Mukhopadhyay, J. Advancing Electrode Properties through Functionalization for Solid Oxide Cells Application: A Review. *Chem. Asian J.* **2023**, *18*, e202201222. [\[CrossRef\]](#)

26. Kaur, P.; Singh, K. Review of Perovskite-Structure Related Cathode Materials for Solid Oxide Fuel Cells. *Ceram. Int.* **2020**, *46*, 5521–5535. [[CrossRef](#)]
27. Jun, A.; Kim, J.; Shin, J.; Kim, G. Perovskite as a Cathode Material: A Review of Its Role in Solid-Oxide Fuel Cell Technology. *ChemElectroChem* **2016**, *3*, 511–530. [[CrossRef](#)]
28. Klyndyuk, A.I.; Chizhova, E.A.; Kharytonau, D.S.; Medvedev, D.A. Layered oxygen-deficient double perovskites as promising cathode materials for solid oxide fuel cells. *Materials* **2022**, *15*, 141. [[CrossRef](#)] [[PubMed](#)]
29. Vinoth Kumar, R.; Khandale, A.P. A Review on Recent Progress and Selection of Cobalt-Based Cathode Materials for Low Temperature-Solid Oxide Fuel Cells. *Renew. Sustain. Energy Rev.* **2022**, *156*, 111985. [[CrossRef](#)]
30. Jiang, S.P. Development of Lanthanum Strontium Manganite Perovskite Cathode Materials of Solid Oxide Fuel Cells: A Review. *J. Mater. Sci.* **2008**, *43*, 6799–6833. [[CrossRef](#)]
31. Carda, M.; Budáč, D.; Paidar, M.; Bouzek, K. Current Trends in the Description of Lanthanum Strontium Manganite Oxygen Electrode Reaction Mechanism in a High-Temperature Solid Oxide Cell. *Curr. Opin. Electrochem.* **2022**, *31*, 100852. [[CrossRef](#)]
32. Oliveira, L.C.; Venâncio, R.; de Azevedo, P.V.; Anchieta, C.G.; Nepel, T.C.; Rodella, C.B.; Zanin, H.; Doubek, G. Reviewing Perovskite Oxide Sites Influence on Electrocatalytic Reactions for High Energy Density Devices. *J. Energy Chem.* **2023**, *81*, 1–19. [[CrossRef](#)]
33. Jiang, S.P. Development of Lanthanum Strontium Cobalt Ferrite Perovskite Electrodes of Solid Oxide Fuel Cells—A Review. *Int. J. Hydrogen Energy* **2019**, *44*, 7448–7493. [[CrossRef](#)]
34. Ndubuisi, A.; Abouali, S.; Singh, K.; Thangadurai, V. Recent Advances, Practical Challenges, and Perspectives of Intermediate Temperature Solid Oxide Fuel Cell Cathodes. *J. Mater. Chem. A* **2022**, *10*, 2196–2227. [[CrossRef](#)]
35. Li, Z.; Li, M.; Zhu, Z. Perovskite Cathode Materials for Low-Temperature Solid Oxide Fuel Cells: Fundamentals to Optimization. *Electrochem. Energy Rev.* **2022**, *5*, 263–311. [[CrossRef](#)]
36. Safian, S.D.; Abd Malek, N.I.; Jamil, Z.; Lee, S.-W.; Tseng, C.-J.; Osman, N. Study on the Surface Segregation of Mixed Ionic-Electronic Conductor Lanthanum-Based Perovskite Oxide  $\text{La}_{1-x}\text{Sr}_x\text{Co}_{1-y}\text{Fe}_y\text{O}_{3-\delta}$ . *Materials. Int. J. Energy Res.* **2022**, *46*, 7101–7117. [[CrossRef](#)]
37. Zarabi Golkhatmi, S.; Asghar, M.I.; Lund, P.D. A Review on Solid Oxide Fuel Cell Durability: Latest Progress, Mechanisms, and Study Tools. *Renew. Sustain. Energy Rev.* **2022**, *161*, 112339. [[CrossRef](#)]
38. Connor, P.A.; Yue, X.; Savaniu, C.D.; Price, R.; Triantafyllou, G.; Cassidy, M.; Kerherve, G.; Payne, D.J.; Maher, R.C.; Cohen, L.F.; et al. Tailoring SOFC Electrode Microstructures for Improved Performance. *Adv. Energy Mater.* **2018**, *8*, 1800120. [[CrossRef](#)]
39. Celik, I.; Lee, S.; Abernathy, H.; Hackett, G. Performance Degradation Predictions Based on Microstructural Evolution Due to Grain Coarsening Effects in Solid Oxide Fuel Cell Electrodes. *J. Electrochem. Soc.* **2018**, *165*, F64–F74. [[CrossRef](#)]
40. Geoffrey Sahini, M.; Daud Lupyana, S. Perspective and Control of Cation Interdiffusion and Interface Reactions in Solid Oxide Fuel Cells (SOFCs). *Mater. Sci. Eng. B* **2023**, *292*, 116415. [[CrossRef](#)]
41. Zhang, L.; Chen, G.; Dai, R.; Lv, X.; Yang, D.; Geng, S. A Review of the Chemical Compatibility between Oxide Electrodes and Electrolytes in Solid Oxide Fuel Cells. *J. Power Sources* **2021**, *492*, 229630. [[CrossRef](#)]
42. Khan, M.Z.; Song, R.-H.; Mehran, M.T.; Lee, S.-B.; Lim, T.-H. Controlling Cation Migration and Inter-Diffusion across Cathode/Interlayer/Electrolyte Interfaces of Solid Oxide Fuel Cells: A Review. *Ceram. Int.* **2021**, *47*, 5839–5869. [[CrossRef](#)]
43. Wang, F.; Kishimoto, H.; Ishiyama, T.; Develos-Bagarinao, K.; Yamaji, K.; Horita, T.; Yokokawa, H. A Review of Sulfur Poisoning of Solid Oxide Fuel Cell Cathode Materials for Solid Oxide Fuel Cells. *J. Power Sources* **2020**, *478*, 228763. [[CrossRef](#)]
44. Wang, C.C.; O'Donnell, K.; Jian, L.; Jiang, S.P. Co-Deposition and Poisoning of Chromium and Sulfur Contaminants on  $\text{La}_{0.6}\text{Sr}_{0.4}\text{Co}_{0.2}\text{Fe}_{0.8}\text{O}_{3-\delta}$  Cathodes of Solid Oxide Fuel Cells. *J. Electrochem. Soc.* **2015**, *162*, F507–F512. [[CrossRef](#)]
45. Wang, R.; Parent, L.R.; Gopalan, S.; Zhong, Y. Experimental and Computational Investigations on the  $\text{SO}_2$  Poisoning of  $(\text{La}_{0.8}\text{Sr}_{0.2})_{0.95}\text{MnO}_3$  Cathode Materials. *Adv. Powder Mater.* **2023**, *2*, 100062. [[CrossRef](#)]
46. Horita, T. Chromium Poisoning for Prolonged Lifetime of Electrodes in Solid Oxide Fuel Cells—Review. *Ceram. Int.* **2021**, *47*, 7293–7306. [[CrossRef](#)]
47. Zhou, L.; Mason, J.H.; Li, W.; Liu, X. Comprehensive Review of Chromium Deposition and Poisoning of Solid Oxide Fuel Cells (SOFCs) Cathode Materials. *Renew. Sustain. Energy Rev.* **2020**, *134*, 110320. [[CrossRef](#)]
48. Wang, R.; Sun, Z.; Lu, Y.; Gopalan, S.; Basu, S.N.; Pal, U.B. Comparison of Chromium Poisoning between Lanthanum Strontium Manganite and Lanthanum Strontium Ferrite Composite Cathodes in Solid Oxide Fuel Cells. *J. Power Sources* **2020**, *476*, 228743. [[CrossRef](#)]
49. Jiang, S.P.; Chen, X. Chromium Deposition and Poisoning of Cathodes of Solid Oxide Fuel Cells—A Review. *Int. J. Hydrogen Energy* **2014**, *39*, 505–531. [[CrossRef](#)]
50. Li, Q.; Wang, X.; Jia, L.; Chi, B.; Pu, J.; Li, J. High Performance and Carbon-Deposition Resistance Metal-Supported Solid Oxide Fuel Cell with a Nickel–Manganese Spinel Modified Anode. *Mater. Today Energy* **2020**, *17*, 100473. [[CrossRef](#)]
51. Girona, K.; Laurencin, J.; Fouletier, J.; Lefebvre-Joud, F. Carbon Deposition in  $\text{CH}_4/\text{CO}_2$  Operated SOFC: Simulation and Experimentation Studies. *J. Power Sources* **2012**, *210*, 381–391. [[CrossRef](#)]
52. Chen, K.; Jiang, S.P. Surface Segregation in Solid Oxide Cell Oxygen Electrodes: Phenomena, Mitigation Strategies and Electrochemical Properties. *Electrochem. Energy Rev.* **2020**, *3*, 730–765. [[CrossRef](#)]
53. van Eck, N.J.; Waltman, L. Software Survey: VOSviewer, a Computer Program for Bibliometric Mapping. *Scientometrics* **2010**, *84*, 523–538. [[CrossRef](#)]

54. Chen, S.; Zhang, H.; Yao, C.; Lou, H.; Chen, M.; Lang, X.; Cai, K. Review of SOFC Cathode Performance Enhancement by Surface Modifications: Recent Advances and Future Directions. *Energy Fuels* **2023**, *37*, 3470–3487. [[CrossRef](#)]
55. Jiang, S.P. Issues on Development of (La,Sr)MnO<sub>3</sub> Cathode for Solid Oxide Fuel Cells. *J. Power Sources* **2003**, *124*, 390–402. [[CrossRef](#)]
56. Cherepanov, V.A.; Barkhatova, L.Y.; Voronin, V.I. Phase Equilibria in the La–Sr–Mn–O System. *J. Solid State Chem.* **1997**, *134*, 38–44. [[CrossRef](#)]
57. Cherepanov, V.A.; Filonova, E.A.; Voronin, V.I.; Berger, I.F.; Barkhatova, L.Y. Phase Equilibria in the LaCoO<sub>3</sub>–LaMnO<sub>3</sub>–SrCoO<sub>2.5</sub>–SrMnO<sub>3</sub> System. *Mater. Res. Bull.* **1999**, *34*, 1481–1489. [[CrossRef](#)]
58. Filonova, E.A.; Demina, A.N.; Kleibaum, E.A.; Gavrilova, L.Y.; Petrov, A.N. Phase Equilibria in the System LaMnO<sub>3+δ</sub>–SrMnO<sub>3</sub>–LaFeO<sub>3</sub>–SrFeO<sub>3–δ</sub>. *Inorg. Mater.* **2006**, *42*, 443–447. [[CrossRef](#)]
59. Yusenko, M.V.; Belyaev, V.D.; Demin, A.K.; Bronin, D.I.; Sobyenin, V.A.; Snytnikov, P.V. A Study of the Electrochemical Characteristics of Single-Chamber Solid Oxide Fuel Cells Based on Platinum and Strontium-Doped Lanthanum Manganite Electrodes and Fed with a Methane–Air Mixture. *Kinet. Catal.* **2022**, *63*, 117–122. [[CrossRef](#)]
60. Mizusaki, J. Electronic Conductivity, Seebeck Coefficient, Defect and Electronic Structure of Nonstoichiometric La<sub>1–x</sub>Sr<sub>x</sub>MnO<sub>3</sub>. *Solid State Ion.* **2000**, *132*, 167–180. [[CrossRef](#)]
61. Mori, M.; Hiei, Y.; Sammes, N.M.; Tomsett, G.A. Thermal-Expansion Behaviors and Mechanisms for Ca- or Sr-Doped Lanthanum Manganite Perovskites under Oxidizing Atmospheres. *J. Electrochem. Soc.* **2000**, *147*, 1295. [[CrossRef](#)]
62. Demina, A.N.; Polovnikova, K.P.; Filonova, E.A.; Petrov, A.N.; Demin, A.K.; Pikalova, E.Y. Thermal Expansion and Electrical Conductivity of La<sub>0.7</sub>Sr<sub>0.3</sub>Mn<sub>1–y</sub>Cr<sub>y</sub>O<sub>3</sub>. *Inorg. Mater.* **2007**, *43*, 430–435. [[CrossRef](#)]
63. Løken, A.; Ricote, S.; Wachowski, S. Thermal and Chemical Expansion in Proton Ceramic Electrolytes and Compatible Electrodes. *Crystals* **2018**, *8*, 365. [[CrossRef](#)]
64. Tsvetkov, D.S.; Sereda, V.V.; Malyshev, D.A.; Ivanov, I.L.; Zuev, A.Y. Chemical Lattice Strain in Nonstoichiometric Oxides: An Overview. *J. Mater. Chem. A* **2022**, *10*, 6351–6375. [[CrossRef](#)]
65. Maiti, T.K.; Majhi, J.; Maiti, S.K.; Singh, J.; Dixit, P.; Rohilla, T.; Ghosh, S.; Bhushan, S.; Chattopadhyay, S. Zirconia- and Ceria-Based Electrolytes for Fuel Cell Applications: Critical Advancements toward Sustainable and Clean Energy Production. *Environ. Sci. Pollut. Res.* **2022**, *29*, 64489–64512. [[CrossRef](#)] [[PubMed](#)]
66. Sameshima, S.; Kawaminami, M.; Hirata, Y. Thermal Expansion of Rare-Earth-Doped Ceria Ceramics. *J. Ceram. Soc. Jpn.* **2002**, *110*, 597–600. [[CrossRef](#)]
67. Tsvinkinberg, V.A.; Tolkacheva, A.S.; Filonova, E.A.; Gyrdasova, O.I.; Pikalov, S.M.; Vorotnikov, V.A.; Vylkov, A.I.; Moskalenko, N.I.; Pikalova, E.Y. Structure, Thermal Expansion and Electrical Conductivity of La<sub>2–x</sub>Gd<sub>x</sub>NiO<sub>4+δ</sub> (0.0 ≤ x ≤ 0.6) Cathode Materials for SOFC Applications. *J. Alloys Compd.* **2021**, *853*, 156728. [[CrossRef](#)]
68. Lee, D.; Han, J.-H.; Chun, Y.; Song, R.-H.; Shin, D.R. Preparation and Characterization of Strontium and Magnesium Doped Lanthanum Gallates as the Electrolyte for IT-SOFC. *J. Power Sources* **2007**, *166*, 35–40. [[CrossRef](#)]
69. Tietz, F. Thermal Expansion of SOFC Materials. *Ionics* **1999**, *5*, 129–139. [[CrossRef](#)]
70. De Haart, L.G.J.; Vinke, I.C. Long-Term Operation of Planar Type SOFC Stacks. *ECS Trans.* **2011**, *35*, 187–194. [[CrossRef](#)]
71. Kim-Lohsoontorn, P.; Brett, D.J.L.; Laosiripojana, N.; Kim, Y.-M.; Bae, J.-M. Performance of Solid Oxide Electrolysis Cells Based on Composite La<sub>0.8</sub>Sr<sub>0.2</sub>MnO<sub>3–δ</sub>–Yttria Stabilized Zirconia and Ba<sub>0.5</sub>Sr<sub>0.5</sub>Co<sub>0.8</sub>Fe<sub>0.2</sub>O<sub>3–δ</sub> Oxygen Electrodes. *Int. J. Hydrogen Energy* **2010**, *35*, 3958–3966. [[CrossRef](#)]
72. De Souza, R.A.; Kilner, J.A.; Walker, J.F. A SIMS Study of Oxygen Tracer Diffusion and Surface Exchange in La<sub>0.8</sub>Sr<sub>0.2</sub>MnO<sub>3+δ</sub>. *Mater. Lett.* **2000**, *43*, 43–52. [[CrossRef](#)]
73. Tai, L. Structure and Electrical Properties of La<sub>1–x</sub>Sr<sub>x</sub>Co<sub>1–y</sub>Fe<sub>y</sub>O<sub>3</sub>. Part 2. The System La<sub>1–x</sub>Sr<sub>x</sub>Co<sub>0.2</sub>Fe<sub>0.8</sub>O<sub>3</sub>. *Solid State Ion.* **1995**, *76*, 273–283. [[CrossRef](#)]
74. Mineshige, A.; Izutsu, J.; Nakamura, M.; Nigaki, K.; Kobune, M.; Fujii, S.; Inaba, M.; Ogumi, Z.; Yao, T. Electrical Property, Crystal Structure and Oxygen Nonstoichiometry of La<sub>1–x</sub>Sr<sub>x</sub>Co<sub>0.2</sub>Fe<sub>0.8</sub>O<sub>3–δ</sub>. *Electrochemistry* **2000**, *68*, 515–518. [[CrossRef](#)]
75. Teraoka, Y.; Zhang, H.M.; Okamoto, K.; Yamazoe, N. Mixed Ionic-Electronic Conductivity of La<sub>1–x</sub>Sr<sub>x</sub>Co<sub>1–y</sub>Fe<sub>y</sub>O<sub>3–δ</sub> Perovskite-Type Oxides. *Mater. Res. Bull.* **1988**, *23*, 51–58. [[CrossRef](#)]
76. Petric, A. Evaluation of La–Sr–Co–Fe–O Perovskites for Solid Oxide Fuel Cells and Gas Separation Membranes. *Solid State Ion.* **2000**, *135*, 719–725. [[CrossRef](#)]
77. Carter, S. Oxygen Transport in Selected Nonstoichiometric Perovskite-Structure Oxides. *Solid State Ion.* **1992**, *53–56*, 597–605. [[CrossRef](#)]
78. Katsuki, M. High Temperature Properties of La<sub>0.6</sub>Sr<sub>0.4</sub>Co<sub>0.8</sub>Fe<sub>0.2</sub>O<sub>3–δ</sub> Oxygen Nonstoichiometry and Chemical Diffusion Constant. *Solid State Ion.* **2003**, *156*, 453–461. [[CrossRef](#)]
79. Simner, S.P.; Anderson, M.D.; Engelhard, M.H.; Stevenson, J.W. Degradation Mechanisms of La–Sr–Co–Fe–O<sub>3</sub> SOFC Cathodes. *Electrochem. Solid-State Lett.* **2006**, *9*, A478. [[CrossRef](#)]
80. Wang, H.; Barnett, S.A. Degradation Mechanisms of Porous La<sub>0.6</sub>Sr<sub>0.4</sub>Co<sub>0.2</sub>Fe<sub>0.8</sub>O<sub>3–δ</sub> Solid Oxide Fuel Cell Cathodes. *J. Electrochem. Soc.* **2018**, *165*, F564–F570. [[CrossRef](#)]
81. Laurencin, J.; Hubert, M.; Sanchez, D.F.; Pylypko, S.; Morales, M.; Morata, A.; Morel, B.; Montinaro, D.; Lefebvre-Joud, F.; Siebert, E. Degradation Mechanism of La<sub>0.6</sub>Sr<sub>0.4</sub>Co<sub>0.2</sub>Fe<sub>0.8</sub>O<sub>3–δ</sub>/Gd<sub>0.1</sub>Ce<sub>0.9</sub>O<sub>2–δ</sub> Composite Electrode Operated under Solid Oxide Electrolysis and Fuel Cell Conditions. *Electrochim. Acta* **2017**, *241*, 459–476. [[CrossRef](#)]

82. Zhao, L.; Drennan, J.; Kong, C.; Amarasinghe, S.; Jiang, S.P. Insight into Surface Segregation and Chromium Deposition on  $\text{La}_{0.6}\text{Sr}_{0.4}\text{Co}_{0.2}\text{Fe}_{0.8}\text{O}_{3-\delta}$  Cathodes of Solid Oxide Fuel Cells. *J. Mater. Chem. A* **2014**, *2*, 11114–11123. [[CrossRef](#)]
83. Lee, W.; Han, J.W.; Chen, Y.; Cai, Z.; Yildiz, B. Cation Size Mismatch and Charge Interactions Drive Dopant Segregation at the Surfaces of Manganite Perovskites. *J. Am. Chem. Soc.* **2013**, *135*, 7909–7925. [[CrossRef](#)]
84. He, S.; Jiang, S.P. Electrode/Electrolyte Interface and Interface Reactions of Solid Oxide Cells: Recent Development and Advances. *Prog. Nat. Sci.* **2021**, *31*, 341–372. [[CrossRef](#)]
85. Stochniol, G.; Syskakis, E.; Naoumidis, A. Chemical Compatibility between Strontium-Doped Lanthanum Manganite and Yttria-Stabilized Zirconia. *J. Am. Ceram. Soc.* **1995**, *78*, 929–932. [[CrossRef](#)]
86. Yokokawa, H.; Tu, H.; Iwanschitz, B.; Mai, A. Fundamental Mechanisms Limiting Solid Oxide Fuel Cell Durability. *J. Power Sources* **2008**, *182*, 400–412. [[CrossRef](#)]
87. Kindermann, L. Chemical Compatibility of the  $\text{LaFeO}_3$  Base Perovskites ( $\text{La}_{0.6}\text{Sr}_{0.4}$ ) $\text{ZFe}_{0.8}\text{M}_{0.2}\text{O}_{3-\delta}$  ( $z = 1, 0.9$ ;  $\text{M} = \text{Cr, Mn, Co, Ni}$ ) with Yttria Stabilized Zirconia. *Solid State Ion.* **1996**, *89*, 215–220. [[CrossRef](#)]
88. Hubert, M.; Laurencin, J.; Cloetens, P.; Mouglin, J.; Ferreira Sanchez, D.; Pylypko, S.; Morales, M.; Morata, A.; Morel, B.; Montinaro, D.; et al. Solid Oxide Cell Degradation Operated in Fuel Cell and Electrolysis Modes: A Comparative Study on Ni Agglomeration and LSCF Destabilization. *ECS Trans.* **2017**, *78*, 3167–3177. [[CrossRef](#)]
89. Kostoglouidis, G. Chemical Reactivity of Perovskite Oxide SOFC Cathodes and Yttria Stabilized Zirconia. *Solid State Ion.* **2000**, *135*, 529–535. [[CrossRef](#)]
90. Fan, B.; Yan, J.; Yan, X. The Ionic Conductivity, Thermal Expansion Behavior, and Chemical Compatibility of  $\text{La}_{0.54}\text{Sr}_{0.44}\text{Co}_{0.2}\text{Fe}_{0.8}\text{O}_{3-\delta}$  as SOFC Cathode Material. *Solid State Sci.* **2011**, *13*, 1835–1839. [[CrossRef](#)]
91. Darvish, S.; Asadikiya, M.; Hu, B.; Singh, P.; Zhong, Y. Thermodynamic Prediction of the Effect of  $\text{CO}_2$  to the Stability of  $(\text{La}_{0.8}\text{Sr}_{0.2})_{0.98}\text{MnO}_{3\pm\delta}$  System. *Int. J. Hydrogen Energy* **2016**, *41*, 10239–10248. [[CrossRef](#)]
92. Hu, B.; Mahapatra, M.K.; Keane, M.; Zhang, H.; Singh, P. Effect of  $\text{CO}_2$  on the Stability of Strontium Doped Lanthanum Manganite Cathode. *J. Power Sources* **2014**, *268*, 404–413. [[CrossRef](#)]
93. Zhao, Z.; Liu, L.; Zhang, X.; Wu, W.; Tu, B.; Ou, D.; Cheng, M. A Comparison on Effects of  $\text{CO}_2$  on  $\text{La}_{0.8}\text{Sr}_{0.2}\text{MnO}_{3+\delta}$  and  $\text{La}_{0.6}\text{Sr}_{0.4}\text{CoO}_{3-\delta}$  Cathodes. *J. Power Sources* **2013**, *222*, 542–553. [[CrossRef](#)]
94. Darvish, S.; Gopalan, S.; Zhong, Y. Thermodynamic Stability Maps for the  $\text{La}_{0.6}\text{Sr}_{0.4}\text{Co}_{0.2}\text{Fe}_{0.8}\text{O}_{3\pm\delta}-\text{CO}_2-\text{O}_2$  System for Application in Solid Oxide Fuel Cells. *J. Power Sources* **2016**, *336*, 351–359. [[CrossRef](#)]
95. Zhao, Z.; Liu, L.; Zhang, X.; Wu, W.; Tu, B.; Cui, D.; Ou, D.; Cheng, M. High- and Low-Temperature Behaviors of  $\text{La}_{0.6}\text{Sr}_{0.4}\text{Co}_{0.2}\text{Fe}_{0.8}\text{O}_{3-\delta}$  Cathode Operating under  $\text{CO}_2/\text{H}_2\text{O}$ -Containing Atmosphere. *Int. J. Hydrogen Energy* **2013**, *38*, 15361–15370. [[CrossRef](#)]
96. Lai, S.Y.; Ding, D.; Liu, M.; Liu, M.; Alamgir, F.M. Operando and in Situ X-ray Spectroscopies of Degradation in  $\text{La}_{0.6}\text{Sr}_{0.4}\text{Co}_{0.2}\text{Fe}_{0.8}\text{O}_{3-\delta}$  Thin Film Cathodes in Fuel Cells. *ChemSusChem* **2014**, *7*, 3078–3087. [[CrossRef](#)]
97. Liu, Y.L.; Hagen, A.; Barfod, R.; Chen, M.; Wang, H.J.; Poulsen, F.W.; Hendriksen, P.V. Microstructural Studies on Degradation of Interface between LSM–YSZ Cathode and YSZ Electrolyte in SOFCs. *Solid State Ion.* **2009**, *180*, 1298–1304. [[CrossRef](#)]
98. Hu, B.; Mahapatra, M.K.; Singh, P. Performance Regeneration in Lanthanum Strontium Manganite Cathode during Exposure to  $\text{H}_2\text{O}$  and  $\text{CO}_2$  Containing Ambient Air Atmospheres. *J. Ceram. Soc. Jpn.* **2015**, *123*, 199–204. [[CrossRef](#)]
99. Xia, Z.; Zhao, D.; Zhou, Y.; Deng, Z.; Kupecki, J.; Fu, X.; Li, X. Control-Oriented Performance Prediction of Solid Oxide Electrolysis Cell and Durability Improvement through Retard Oxygen Electrode Delamination with Reverse Operation. *Energy Convers. Manag.* **2023**, *277*, 116596. [[CrossRef](#)]
100. Wachsman, E.D.; Huang, Y.-L.; Pellegrinelli, C.; Taillon, J.A.; Salamanca-Riba, L.G. Towards a Fundamental Understanding of the Cathode Degradation Mechanisms. *ECS Trans.* **2014**, *61*, 47–56. [[CrossRef](#)]
101. Wei, B.; Chen, K.; Zhao, L.; Lü, Z.; Jiang, S.P. Chromium Deposition and Poisoning at  $\text{La}_{0.6}\text{Sr}_{0.4}\text{Co}_{0.2}\text{Fe}_{0.8}\text{O}_{3-\delta}$  Oxygen Electrodes of Solid Oxide Electrolysis Cells. *Phys. Chem. Chem. Phys.* **2015**, *17*, 1601–1609. [[CrossRef](#)] [[PubMed](#)]
102. Subotić, V.; Futamura, S.; Harrington, G.F.; Matsuda, J.; Natsukoshi, K.; Sasaki, K. Towards Understanding of Oxygen Electrode Processes during Solid Oxide Electrolysis Operation to Improve Simultaneous Fuel and Oxygen Generation. *J. Power Sources* **2021**, *492*, 229600. [[CrossRef](#)]
103. He, S.; Saunders, M.; Chen, K.; Gao, H.; Suvorova, A.; Rickard, W.D.A.; Quadir, Z.; Cui, C.Q.; Jiang, S.P. A FIB-STEM Study of Strontium Segregation and Interface Formation of Directly Assembled  $\text{La}_{0.6}\text{Sr}_{0.4}\text{Co}_{0.2}\text{Fe}_{0.8}\text{O}_{3-\delta}$  Cathode on  $\text{Y}_2\text{O}_3\text{-ZrO}_2$  Electrolyte of Solid Oxide Fuel Cells. *J. Electrochem. Soc.* **2018**, *165*, F417–F429. [[CrossRef](#)]
104. Pellegrinelli, C.; Huang, Y.-L.; Wachsman, E.D. Effect of  $\text{H}_2\text{O}$  and  $\text{CO}_2$  on LSCF–GDC Composite Cathodes. *ECS Trans.* **2019**, *91*, 665–680. [[CrossRef](#)]
105. Xiong, C.; Qiu, P.; Zhang, W.; Pu, J. Influence of Practical Operating Temperature on the Cr Poisoning for LSCF-GDC Cathode. *Ceram. Int.* **2022**, *48*, 33999–34004. [[CrossRef](#)]
106. Minh, N.Q. Development of Reversible Solid Oxide Fuel Cells (RSOFCs) and Stacks. *ECS Trans.* **2011**, *35*, 2897–2904. [[CrossRef](#)]
107. Monaco, F.; Ferreira-Sanchez, D.; Hubert, M.; Morel, B.; Montinaro, D.; Grolimund, D.; Laurencin, J. Oxygen Electrode Degradation in Solid Oxide Cells Operating in Electrolysis and Fuel Cell Modes: LSCF Destabilization and Interdiffusion at the Electrode/Electrolyte Interface. *Int. J. Hydrogen Energy* **2021**, *46*, 31533–31549. [[CrossRef](#)]
108. Lu, K.; Shen, F. Long Term Behaviors of  $\text{La}_{0.8}\text{Sr}_{0.2}\text{MnO}_3$  and  $\text{La}_{0.6}\text{Sr}_{0.4}\text{Co}_{0.2}\text{Fe}_{0.8}\text{O}_3$  as Cathodes for Solid Oxide Fuel Cells. *Int. J. Hydrogen Energy* **2014**, *39*, 7963–7971. [[CrossRef](#)]

109. Türk, H.; Götsch, T.; Schmidt, F.; Hammud, A.; Ivanov, D.; (Bert) de Haart, L.G.J.; Vinke, I.C.; Eichel, R.; Schlögl, R.; Reuter, K.; et al. Sr Surface Enrichment in Solid Oxide Cells—Approaching the Limits of EDX Analysis by Multivariate Statistical Analysis and Simulations. *ChemCatChem* **2022**, *14*, e202200300. [[CrossRef](#)]
110. Li, D.; Zhang, X.; Liang, C.; Jin, Y.; Fu, M.; Yuan, J.; Xiong, Y. Study on Durability of Novel Core-Shell-Structured  $\text{La}_{0.8}\text{Sr}_{0.2}\text{Co}_{0.2}\text{Fe}_{0.8}\text{O}_{3-\delta}$ @ $\text{Gd}_{0.2}\text{Ce}_{0.8}\text{O}_{1.9}$  Composite Materials for Solid Oxide Fuel Cell Cathodes. *Int. J. Hydrogen Energy* **2021**, *46*, 28221–28231. [[CrossRef](#)]
111. Türk, H.; Schmidt, F.; Götsch, T.; Girgsdies, F.; Hammud, A.; Ivanov, D.; Vinke, I.C.; (Bert) de Haart, L.G.J.; Eichel, R.; Reuter, K.; et al. Complexions at the Electrolyte/Electrode Interface in Solid Oxide Cells. *Adv. Mater. Interfaces* **2021**, *8*, 2100967. [[CrossRef](#)]
112. Cheng, K.; Xu, H.; Zhang, L.; Du, Y.; Zhou, J.; Tang, S.; Chen, M. Numerical Simulation of the  $\text{SrZrO}_3$  Formation in Solid Oxide Fuel Cells. *J. Electron. Mater.* **2019**, *48*, 5510–5515. [[CrossRef](#)]
113. Jacobs, R.; Liu, J.; Na, B.T.; Guan, B.; Yang, T.; Lee, S.; Hackett, G.; Kalapos, T.; Abernathy, H.; Morgan, D. Unconventional Highly Active and Stable Oxygen Reduction Catalysts Informed by Computational Design Strategies. *Adv. Energy Mater.* **2022**, *12*, 2201203. [[CrossRef](#)]
114. Han, H.; Hu, X.; Zhang, B.; Zhang, S.; Zhang, Y.; Xia, C. Method to Determine the Oxygen Reduction Reaction Kinetics via Porous Dual-Phase Composites Based on Electrical Conductivity Relaxation. *J. Mater. Chem. A* **2023**, *11*, 2460–2471. [[CrossRef](#)]
115. Yan, Z.; He, A.; Hara, S.; Shikazono, N. Design and Optimization of Functionally Graded Electrodes for Solid Oxide Fuel Cells (SOFCs) by Mesoscale Modeling. *Int. J. Hydrogen Energy* **2022**, *47*, 16610–16625. [[CrossRef](#)]
116. Padinjarethil, A.K.; Bianchi, F.R.; Bosio, B.; Hagen, A. Electrochemical Characterization and Modelling of Anode and Electrolyte Supported Solid Oxide Fuel Cells. *Front. Energy Res.* **2021**, *9*, 668964. [[CrossRef](#)]
117. Bliem, R.; Kim, D.; Wang, J.; Crumlin, E.J.; Yildiz, B. Hf Deposition Stabilizes the Surface Chemistry of Perovskite Manganese Oxide. *J. Phys. Chem. C* **2021**, *125*, 3346–3354. [[CrossRef](#)] [[PubMed](#)]
118. Zeng, D.; Xu, K.; Zhu, F.; Chen, Y. Enhancing the Oxygen Reduction Reaction Activity and Durability of a Solid Oxide Fuel Cell Cathode by Surface Modification of a Hybrid Coating. *Int. J. Hydrogen Energy* **2023**, *48*, 23992–24001. [[CrossRef](#)]
119. Li, J.; Zhou, X.; Wu, C.; Zhao, L.; Dong, B.; Wang, S.; Chi, B. Self-Stabilized Hybrid Cathode for Solid Oxide Fuel Cell: A-Site Deficient Perovskite Coating as Solid Solution for Strontium Diffusion. *Chem. Eng. J.* **2022**, *438*, 135446. [[CrossRef](#)]
120. Zhang, X.; Jin, Y.; Jiang, Y.; Zong, X.; Li, Y.; Xiong, Y. Enhancing Chromium Poisoning Tolerance of  $\text{La}_{0.8}\text{Sr}_{0.2}\text{Co}_{0.2}\text{Fe}_{0.8}\text{O}_{3-\delta}$  Cathode by  $\text{Ce}_{0.8}\text{Gd}_{0.2}\text{O}_{1.9-\delta}$  Coating. *J. Power Sources* **2022**, *547*, 231996. [[CrossRef](#)]
121. Pei, K.; Zhou, Y.; Ding, Y.; Xu, K.; Zhang, H.; Yuan, W.; Sasaki, K.; Choi, Y.; Liu, M.; Chen, Y. An Improved Oxygen Reduction Reaction Activity and  $\text{CO}_2$ -Tolerance of  $\text{La}_{0.6}\text{Sr}_{0.4}\text{Co}_{0.2}\text{Fe}_{0.8}\text{O}_{3-\delta}$  Achieved by a Surface Modification with Barium Cobaltite Coatings. *J. Power Sources* **2021**, *514*, 230573. [[CrossRef](#)]
122. Pei, K.; Zhou, Y.; Xu, K.; He, Z.; Chen, Y.; Zhang, W.; Yoo, S.; Zhao, B.; Yuan, W.; Liu, M.; et al. Enhanced Cr-Tolerance of an SOFC Cathode by an Efficient Electro-Catalyst Coating. *Nano Energy* **2020**, *72*, 104704. [[CrossRef](#)]
123. Ishfaq, H.A.; Khan, M.Z.; Shirke, Y.M.; Qamar, S.; Hussain, A.; Mehran, M.T.; Song, R.-H.; Saleem, M. A Heuristic Approach to Boost the Performance and Cr Poisoning Tolerance of Solid Oxide Fuel Cell Cathode by Robust Multi-Doped Ceria Coating. *Appl. Catal. B Environ.* **2023**, *323*, 122178. [[CrossRef](#)]
124. Chen, Y.; Hinerman, A.; Liang, L.; Gerdes, K.; Navia, S.P.; Prucz, J.; Song, X. Conformal Coating of Cobalt Oxide on Solid Oxide Fuel Cell Cathode and Resultant Continuously Increased Oxygen Reduction Reaction Kinetics upon Operation. *J. Power Sources* **2018**, *405*, 45–50. [[CrossRef](#)]
125. Niu, Y.; Zhou, Y.; Zhang, W.; Zhang, Y.; Evans, C.; Luo, Z.; Kane, N.; Ding, Y.; Chen, Y.; Guo, X.; et al. Highly Active and Durable Air Electrodes for Reversible Protonic Ceramic Electrochemical Cells Enabled by an Efficient Bifunctional Catalyst. *Adv. Energy Mater.* **2022**, *12*, 2103783. [[CrossRef](#)]
126. Zhang, X.; Jin, Y.; Li, D.; Zong, X.; Xiong, Y. Effects of  $\text{Gd}_{0.8}\text{Ce}_{0.2}\text{O}_{1.9-\delta}$  Coating with Different Thickness on Electrochemical Performance and Long-Term Stability of  $\text{La}_{0.8}\text{Sr}_{0.2}\text{Co}_{0.2}\text{Fe}_{0.8}\text{O}_{3-\delta}$  Cathode in SOFCs. *Int. J. Hydrogen Energy* **2022**, *47*, 4100–4108. [[CrossRef](#)]
127. Chen, Y.; Paredes-Navia, S.A.; Romo-De-La-Cruz, C.-O.; Liang, L.; Fernandes, A.; Hinerman, A.; Prucz, J.; Williams, M.; Song, X. Coating Internal Surface of Porous Electrode for Decreasing the Ohmic Resistance and Shifting Oxygen Reduction Reaction Pathways in Solid Oxide Fuel Cells. *J. Power Sources* **2021**, *499*, 229854. [[CrossRef](#)]
128. Niu, Y.; Zhou, Y.; Lv, W.; Chen, Y.; Zhang, Y.; Zhang, W.; Luo, Z.; Kane, N.; Ding, Y.; Soule, L.; et al. Enhancing Oxygen Reduction Activity and Cr Tolerance of Solid Oxide Fuel Cell Cathodes by a Multiphase Catalyst Coating. *Adv. Funct. Mater.* **2021**, *31*, 2100034. [[CrossRef](#)]
129. Yokokawa, H.; Horita, T. Cathodes. In *High Temperature and Solid Oxide Fuel Cells*; Elsevier: Amsterdam, The Netherlands, 2003; pp. 119–147. ISBN 978-1-85617-387-2.
130. Filonova, E.A.; Gilev, A.R.; Skutina, L.S.; Vylkov, A.I.; Kuznetsov, D.K.; Shur, V.Y. Double  $\text{Sr}_2\text{Ni}_{1-x}\text{Mg}_x\text{MoO}_6$  Perovskites ( $x = 0, 0.25$ ) as Perspective Anode Materials for  $\text{LaGaO}_3$ -Based Solid Oxide Fuel Cells. *Solid State Ion.* **2018**, *314*, 112–118. [[CrossRef](#)]
131. Wu, Y.; Sang, J.; Liu, Z.; Fan, H.; Cao, B.; Wang, Q.; Yang, J.; Guan, W.; Liu, X.; Wang, J. Enhancing the Performance and Stability of Solid Oxide Fuel Cells by Adopting Samarium-Doped Ceria Buffer Layer. *Ceram. Int.* **2023**, *49*, 20290–20297. [[CrossRef](#)]
132. Yang, Q.; Wang, Y.; Tian, D.; Wu, H.; Ding, Y.; Lu, X.; Chen, Y.; Lin, B. Enhancing Performance and Stability of Symmetrical Solid Oxide Fuel Cells via Quasi-Symmetrical Ceria-Based Buffer Layers. *Ceram. Int.* **2022**, *48*, 27509–27515. [[CrossRef](#)]
133. Zhang, Y.; Niu, B.; Hao, X.; Wang, Y.; Liu, J.; Jiang, P.; He, T. Layered Oxygen-Deficient Double Perovskite  $\text{GdBaFe}_2\text{O}_{5+\delta}$  as Electrode Material for Symmetrical Solid-Oxide Fuel Cells. *Electrochim. Acta* **2021**, *370*, 137807. [[CrossRef](#)]

134. Niemczyk, A.; Zheng, K.; Cichy, K.; Berent, K.; Küster, K.; Starke, U.; Poudel, B.; Dabrowski, B.; Świerczek, K. High Cu Content  $\text{LaNi}_{1-x}\text{Cu}_x\text{O}_{3-\delta}$  Perovskites as Candidate Air Electrode Materials for Reversible Solid Oxide Cells. *Int. J. Hydrogen Energy* **2020**, *45*, 29449–29464. [[CrossRef](#)]
135. Yang, X.; Li, R.; Yang, Y.; Wen, G.; Tian, D.; Lu, X.; Ding, Y.; Chen, Y.; Lin, B. Improving Stability and Electrochemical Performance of  $\text{Ba}_{0.5}\text{Sr}_{0.5}\text{Co}_{0.2}\text{Fe}_{0.8}\text{O}_{3-\delta}$  Electrode for Symmetrical Solid Oxide Fuel Cells by Mo Doping. *J. Alloys Compd.* **2020**, *831*, 154711. [[CrossRef](#)]
136. Huang, K.; Wan, J.; Goodenough, J.B. Oxide-Ion Conducting Ceramics for Solid Oxide Fuel Cells. *J. Mater. Sci.* **2001**, *36*, 1093–1098. [[CrossRef](#)]
137. Yun, J.W.; Yoon, S.P.; Park, S.; Han, J.; Nam, S.W.; Lim, T.-H.; Kim, J.-S. Modifying the Cathodes of Intermediate-Temperature Solid Oxide Fuel Cells with a  $\text{Ce}_{0.8}\text{Sm}_{0.2}\text{O}_2$  Sol–Gel Coating. *Int. J. Hydrogen Energy* **2009**, *34*, 9213–9219. [[CrossRef](#)]
138. Hanifi, A.R.; Paulson, S.; Torabi, A.; Shinbine, A.; Tucker, M.C.; Birss, V.; Etsell, T.H.; Sarkar, P. Slip-Cast and Hot-Solution Infiltrated Porous Yttria Stabilized Zirconia (YSZ) Supported Tubular Fuel Cells. *J. Power Sources* **2014**, *266*, 121–131. [[CrossRef](#)]
139. Hwang, S.; Lee, J.; Kang, G.; Choi, M.; Kim, S.J.; Lee, W.; Byun, D. A Hydrogel-Assisted GDC Chemical Diffusion Barrier for Durable Solid Oxide Fuel Cells. *J. Mater. Chem. A* **2021**, *9*, 11683–11690. [[CrossRef](#)]
140. Liu, Y.; Tian, Y.; Wang, Y.; Li, Y.; Pu, J.; Ciucci, F.; Chi, B. Nano Film  $\text{Pr}_2\text{Ni}_{0.8}\text{Cu}_{0.2}\text{O}_{4+\delta}$  Decorated  $\text{La}_{0.6}\text{Sr}_{0.4}\text{Co}_{0.2}\text{Fe}_{0.8}\text{O}_{3-\delta}$  Oxygen Electrode for Highly Efficient and Stable Reversible Solid Oxide Cells. *Electrochim. Acta* **2022**, *430*, 141032. [[CrossRef](#)]
141. Wang, Y.; Xu, N.; Dogdibegovic, E.; Su, T.; Brocato, A.D.; Zhou, X.-D. Role of Mixed Conducting  $\text{Pr}_{0.1}\text{Gd}_{0.1}\text{Ce}_{0.8}\text{O}_{1.9-\delta}$  Barrier Layer on the Promotion of SOFC Performance. *Int. J. Hydrogen Energy* **2022**, *47*, 1917–1924. [[CrossRef](#)]
142. Park, J.H.; Jung, C.H.; Kim, K.J.; Kim, D.; Shin, H.R.; Hong, J.-E.; Lee, K.T. Enhancing Bifunctional Electrocatalytic Activities of Oxygen Electrodes via Incorporating Highly Conductive  $\text{Sm}^{3+}$  and  $\text{Nd}^{3+}$  Double-Doped Ceria for Reversible Solid Oxide Cells. *ACS Appl. Mater. Interfaces* **2021**, *13*, 2496–2506. [[CrossRef](#)] [[PubMed](#)]
143. Park, J.H.; Han, S.M.; Kim, B.-K.; Lee, J.-H.; Yoon, K.J.; Kim, H.; Ji, H.-I.; Son, J.-W. Sintered Powder-Base Cathode over Vacuum-Deposited Thin-Film Electrolyte of Low-Temperature Solid Oxide Fuel Cell: Performance and Stability. *Electrochim. Acta* **2019**, *296*, 1055–1063. [[CrossRef](#)]
144. Choi, H.-J.; Na, Y.-H.; Kwak, M.; Kim, T.W.; Seo, D.-W.; Woo, S.-K.; Kim, S.-D. Development of Solid Oxide Cells by Co-Sintering of GDC Diffusion Barriers with LSCF Air Electrode. *Ceram. Int.* **2017**, *43*, 13653–13660. [[CrossRef](#)]
145. Yoo, Y.-S.; Jeon, S.-Y.; Park, M.-A.; Lee, J.; Lee, Y. Electrochemical Performance of Solid Oxide Electrolysis Cells with LSCF6428–SDC/SDC Electrode for  $\text{H}_2\text{O}/\text{CO}_2$  High Temperature Co-Electrolysis. *ECS Trans.* **2017**, *78*, 3123–3128. [[CrossRef](#)]
146. Zhang, G.; Zheng, G.; Huang, Z.; Bao, X.; Shi, C.; Yang, X.; Zhou, J.; Chen, T.; Wang, S. The Effect of  $\text{Fe}_2\text{O}_3$  Sintering Aid on  $\text{Gd}_{0.1}\text{Ce}_{0.9}\text{O}_{1.95}$  Diffusion Barrier Layer and Solid Oxide Fuel Cell Performance. *Int. J. Hydrogen Energy* **2023**, *48*, 21908–21919. [[CrossRef](#)]
147. Budiman, R.A.; Yamaguchi, T.; Ishiyama, T.; Develos-Bagarinao, K.; Yamaji, K.; Kishimoto, H. Interlayer Modification for High-Performance and Stable Solid Oxide Electrolysis Cell. *Mater. Lett.* **2022**, *309*, 131419. [[CrossRef](#)]
148. Wu, P.; Tian, Y.; Lü, Z.; Zhang, X.; Ding, L. Electrochemical Performance of  $\text{La}_{0.65}\text{Sr}_{0.35}\text{MnO}_3$  Oxygen Electrode with Alternately Infiltrated  $\text{Sm}_{0.5}\text{Sr}_{0.5}\text{CoO}_{3-\delta}$  and  $\text{Sm}_{0.2}\text{Ce}_{0.8}\text{O}_{1.9}$  Nanoparticles for Reversible Solid Oxide Cells. *Int. J. Hydrogen Energy* **2022**, *47*, 747–760. [[CrossRef](#)]
149. Yaroslavtsev, I.Y.; Kuzin, B.L.; Bronin, D.I.; Bogdanovich, N.M. Polarization Characteristics of Composite Electrodes in Electrochemical Cells with Solid Electrolytes Based on  $\text{CeO}_2$  and  $\text{LaGaO}_3$ . *Russ. J. Electrochem.* **2005**, *41*, 527–531. [[CrossRef](#)]
150. Mosialek, M.; Zimowska, M.; Kharytonau, D.; Komenda, A.; Górski, M.; Krzan, M. Improvement of  $\text{La}_{0.8}\text{Sr}_{0.2}\text{MnO}_{3-\delta}$  Cathode Material for Solid Oxide Fuel Cells by Addition of  $\text{YFe}_{0.5}\text{Co}_{0.5}\text{O}_3$ . *Materials* **2022**, *15*, 642. [[CrossRef](#)]
151. Bogdanovich, N.M.; Bronin, D.I.; Vdovin, G.K.; Yaroslavtsev, I.Y.; Kuzin, B.L. Effect of  $\text{Bi}_{0.75}\text{Y}_{0.25}\text{O}_{1.5}$  Electrolyte Additive in Collector Layer to Properties of Bilayer Composite Cathodes of Solid Oxide Fuel Cells Based on  $\text{La}(\text{Sr})\text{MnO}_3$  and  $\text{La}(\text{Sr})\text{Fe}(\text{Co})\text{O}_3$  Compounds. *Russ. J. Electrochem.* **2009**, *45*, 456–464. [[CrossRef](#)]
152. Perry Murray, E.  $(\text{La},\text{Sr})\text{MnO}_3-(\text{Ce},\text{Gd})\text{O}_{2-x}$  Composite Cathodes for Solid Oxide Fuel Cells. *Solid State Ion.* **2001**, *143*, 265–273. [[CrossRef](#)]
153. Chen, G.; Gao, Y.; Luo, Y.; Guo, R. Effect of A Site Deficiency of LSM Cathode on the Electrochemical Performance of SOFCs with Stabilized Zirconia Electrolyte. *Ceram. Int.* **2017**, *43*, 1304–1309. [[CrossRef](#)]
154. Sun, K.; Yu, Z.; Ni, Q.; Li, Y.; Xu, D.; Gu, Y.; Zheng, Y.; Chen, H.; Ge, L.; Guo, L. Highly Durable Sr-Doped  $\text{LaMnO}_3$ -Based Cathode Modified with  $\text{Pr}_6\text{O}_{11}$  Nano-Catalyst for Protonic Ceramic Fuel Cells Based on Y-Doped  $\text{BaZrO}_3$  Electrolyte. *J. Eur. Ceram. Soc.* **2022**, *42*, 4266–4274. [[CrossRef](#)]
155. Cao, X.G.; Jiang, S.P. Identification of Oxygen Reduction Processes at  $(\text{La},\text{Sr})\text{MnO}_3$  Electrode/ $\text{La}_{0.5}\text{Si}_6\text{O}_{26.25}$  Apatite Electrolyte Interface of Solid Oxide Fuel Cells. *Int. J. Hydrogen Energy* **2013**, *38*, 2421–2431. [[CrossRef](#)]
156. Strandbakke, R.; Dyrllie, O.; Hage, F.S.; Norby, T. Reaction Kinetics of Protons and Oxide Ions in LSM/Lanthanum Tungstate Cathodes with Pt Nanoparticle Activation. *J. Electrochem. Soc.* **2016**, *163*, F507–F515. [[CrossRef](#)]
157. Shen, F.; Wang, R.; Tucker, M.C. Long Term Durability Test and Post Mortem for Metal-Supported Solid Oxide Electrolysis Cells. *J. Power Sources* **2020**, *474*, 228618. [[CrossRef](#)]
158. Mater, A.; Othmani, A.; Boukhachem, A.; Madani, A. Cathode Performance Study of  $\text{La}_{0.6}\text{Sr}_{0.4}\text{Co}_{0.8}\text{Fe}_{0.2}\text{O}_{3-\delta}$  with Various Electrolyte-Doped Ceria  $\text{Ce}_{0.8}\text{Sm}_{0.17}\text{Ln}_{0.03}\text{O}_{1.9}$  for IT-Solid Oxide Fuel Cell. *J. Electron. Mater.* **2020**, *49*, 4123–4133. [[CrossRef](#)]

159. Yang, C.; Cheng, J.G.; He, H.G.; Gao, J.F. Ni/SDC Materials for Solid Oxide Fuel Cell Anode Applications by the Glycine-Nitrate Method. *Key Eng. Mater.* **2010**, *434–435*, 731–734. [[CrossRef](#)]
160. Ahuja, A.; Gautam, M.; Sinha, A.; Sharma, J.; Patro, P.K.; Venkatasubramanian, A. Effect of Processing Route on the Properties of LSCF-Based Composite Cathode for IT-SOFC. *Bull. Mater. Sci.* **2020**, *43*, 129. [[CrossRef](#)]
161. He, A.; Onishi, J.; Shikazono, N. Optimization of Electrode-Electrolyte Interface Structure for Solid Oxide Fuel Cell Cathode. *J. Power Sources* **2020**, *449*, 227565. [[CrossRef](#)]
162. Loureiro, F.J.A.; Macedo, D.A.; Nascimento, R.M.; Cesário, M.R.; Grilo, J.P.F.; Yaremchenko, A.A.; Fagg, D.P. Cathodic Polarisation of Composite LSCF-SDC IT-SOFC Electrode Synthesised by One-Step Microwave Self-Assisted Combustion. *J. Eur. Ceram. Soc.* **2019**, *39*, 1846–1853. [[CrossRef](#)]
163. Wei, F.; Wang, L.; Luo, L.; Cheng, L.; Xu, X. One-Pot Impregnation to Construct Nanoparticles Loaded Scaffold Cathode with Enhanced Oxygen Reduction Performance for LT-SOFCs. *J. Alloys Compd.* **2023**, *941*, 168981. [[CrossRef](#)]
164. Sun, Y.; He, S.; Saunders, M.; Chen, K.; Shao, Z.; Jiang, S.P. A Comparative Study of Surface Segregation and Interface of  $\text{La}_{0.6}\text{Sr}_{0.4}\text{Co}_{0.2}\text{Fe}_{0.8}\text{O}_{3-\delta}$  Electrode on GDC and YSZ Electrolytes of Solid Oxide Fuel Cells. *Int. J. Hydrogen Energy* **2021**, *46*, 2606–2616. [[CrossRef](#)]
165. Abarzua, G.; Udayabhaskar, R.; Mangalaraja, R.V.; Durango-Petro, J.; Usuba, J.; Flies, H. A Feasible Strategy for Tailoring Stable Spray-Coated Electrolyte Layer in Micro-Tubular Solid Oxide Fuel Cells. *Int. J. Appl. Ceram. Technol.* **2022**, *19*, 1389–1396. [[CrossRef](#)]
166. Samreen, A.; Galvez-Sanchez, M.; Steinberger-Wilckens, R.; Arifin, N.A.; Saher, S.; Ali, S.; Qamar, A. Electrochemical Performance of Novel NGCO–LSCF Composite Cathode for Intermediate Temperature Solid Oxide Fuel Cells. *Int. J. Hydrogen Energy* **2020**, *45*, 21714–21721. [[CrossRef](#)]
167. Hong, T.; Lee, S.; Ohodnicki, P.; Brinkman, K. A Highly Scalable Spray Coating Technique for Electrode Infiltration: Barium Carbonate Infiltrated  $\text{La}_{0.6}\text{Sr}_{0.4}\text{Co}_{0.2}\text{Fe}_{0.8}\text{O}_{3-\delta}$  Perovskite Structured Electrocatalyst with Demonstrated Long Term Durability. *Int. J. Hydrogen Energy* **2017**, *42*, 24978–24988. [[CrossRef](#)]
168. Tsuji, Y.; Amezawa, K.; Nakao, T.; Ina, T.; Kawada, T.; Yamamoto, K.; Uchimoto, Y.; Orikasa, Y. Investigation of Cathodic Reaction Mechanism in Solid Oxide Fuel Cells by Operando X-ray Absorption Spectroscopy. *Electrochemistry* **2020**, *88*, 560–565. [[CrossRef](#)]
169. Chen, X.; Sun, X.; Zhou, J.; Zhou, D.; Zhu, X.; Meng, J. Effects of CoO and  $\text{Bi}_2\text{O}_3$  Single/Dual Sintering Aids Doping on Structure and Properties of  $\text{Ce}_{0.8}\text{Nd}_{0.2}\text{O}_{1.9}$ . *Ceram. Int.* **2020**, *46*, 22727–22732. [[CrossRef](#)]
170. Wang, Y.-P.; Liu, S.-H.; Zhang, H.-Y.; Li, C.-X.; Zhang, S.-L.; Yang, G.-J.; Li, C.-J. Structured  $\text{La}_{0.6}\text{Sr}_{0.4}\text{Co}_{0.2}\text{Fe}_{0.8}\text{O}_{3-\delta}$  Cathode with Large-Scale Vertical Cracks by Atmospheric Laminar Plasma Spraying for IT-SOFCs. *J. Alloys Compd.* **2020**, *825*, 153865. [[CrossRef](#)]
171. Wang, J.; Yang, Z.; Yang, K.; Peng, S. Kinetics of Oxygen Reaction in Porous  $\text{La}_{0.6}\text{Sr}_{0.4}\text{Co}_{0.2}\text{Fe}_{0.8}\text{O}_{3-\delta}$ - $\text{Ce}_{0.8}\text{Gd}_{0.2}\text{O}_{1.9}$  Composite Electrodes for Solid Oxide Cells. *Int. J. Hydrogen Energy* **2021**, *46*, 25608–25619. [[CrossRef](#)]
172. Khaerudini, D.S.; Guan, G.; Zhang, P.; Hao, X.; Wang, Z.; Xue, C.; Kasai, Y.; Abudula, A. Performance Assessment of  $\text{Bi}_{0.3}\text{Sr}_{0.7}\text{Co}_{0.3}\text{Fe}_{0.7}\text{O}_{3-\delta}$ -LSCF Composite as Cathode for Intermediate-Temperature Solid Oxide Fuel Cells with  $\text{La}_{0.8}\text{Sr}_{0.2}\text{Ga}_{0.8}\text{Mg}_{0.2}\text{O}_{3-\delta}$  Electrolyte. *J. Power Sources* **2015**, *298*, 269–279. [[CrossRef](#)]
173. Zhang, S.-L.; Shang, Y.-B.; Li, C.-X.; Li, C.-J. Vacuum Cold Sprayed Nanostructured  $\text{La}_{0.6}\text{Sr}_{0.4}\text{Co}_{0.2}\text{Fe}_{0.8}\text{O}_{3-\delta}$  as a High-Performance Cathode for Porous Metal-Supported Solid Oxide Fuel Cells Operating below 600 °C. *Mater. Today Energy* **2021**, *21*, 100815. [[CrossRef](#)]
174. Wang, S.-F.; Lu, H.-C.; Hsu, Y.-F.; Jasinski, P. High-Performance Anode-Supported Solid Oxide Fuel Cells with Co-Fired  $\text{Sm}_{0.2}\text{Ce}_{0.8}\text{O}_{2-\delta}$ / $\text{La}_{0.8}\text{Sr}_{0.2}\text{Ga}_{0.8}\text{Mg}_{0.2}\text{O}_{3-\delta}$ / $\text{Sm}_{0.2}\text{Ce}_{0.8}\text{O}_{2-\delta}$  Sandwiched Electrolyte. *Int. J. Hydrogen Energy* **2022**, *47*, 5429–5438. [[CrossRef](#)]
175. Lei, L.; Tao, Z.; Hong, T.; Wang, X.; Chen, F. A Highly Active Hybrid Catalyst Modified  $(\text{La}_{0.60}\text{Sr}_{0.40})_{0.95}\text{Co}_{0.20}\text{Fe}_{0.80}\text{O}_{3-\delta}$  Cathode for Proton Conducting Solid Oxide Fuel Cells. *J. Power Sources* **2018**, *389*, 1–7. [[CrossRef](#)]
176. Di Bartolomeo, E.; Zunic, M.; Chevallier, L.; D’Epifanio, A.; Licocchia, S.; Traversa, E. Fabrication of Proton Conducting Solid Oxide Fuel Cells by Using Electrophoretic Deposition. *ECS Trans.* **2009**, *25*, 577–584. [[CrossRef](#)]
177. Watanabe, K.; Yamaguchi, Y.; Nomura, K.; Sumi, H.; Mori, M.; Mizutani, Y.; Shimada, H. Effect of Cobalt Content on Electrochemical Performance for  $\text{La}_{0.6}\text{Sr}_{0.4}\text{Co}_x\text{Fe}_{1-x}\text{O}_{3-\delta}$  and  $\text{BaZr}_{0.8}\text{Yb}_{0.2}\text{O}_{3-\delta}$  Composite Cathodes in Protonic Ceramic Fuel Cells. *Ceram. Int.* **2023**, *49*, 21085–21090. [[CrossRef](#)]
178. Vafaenezhad, S.; Sandhu, N.K.; Hanifi, A.R.; Etsell, T.H.; Sarkar, P. Development of Proton Conducting Fuel Cells Using Nickel Metal Support. *J. Power Sources* **2019**, *435*, 226763. [[CrossRef](#)]
179. Zhang, Q.; Hou, Y.; Chen, L.; Wang, L.; Chou, K. Enhancement of Electrochemical Performance for Proton Conductive Solid Oxide Fuel Cell by 30%GDC–LSCF Cathode. *Ceram. Int.* **2022**, *48*, 17816–17827. [[CrossRef](#)]
180. Chen, X.; Zhang, H.; Li, Y.; Xing, J.; Zhang, Z.; Ding, X.; Zhang, B.; Zhou, J.; Wang, S. Fabrication and Performance of Anode-Supported Proton Conducting Solid Oxide Fuel Cells Based on  $\text{BaZr}_{0.1}\text{Ce}_{0.7}\text{Y}_{0.1}\text{Yb}_{0.1}\text{O}_{3-\delta}$  Electrolyte by Multi-Layer Aqueous-Based Co-Tape Casting. *J. Power Sources* **2021**, *506*, 229922. [[CrossRef](#)]
181. Shimada, H.; Yamaguchi, Y.; Sumi, H.; Mizutani, Y. Performance Comparison of Perovskite Composite Cathodes with  $\text{BaZr}_{0.1}\text{Ce}_{0.7}\text{Y}_{0.1}\text{Yb}_{0.1}\text{O}_{3-\delta}$  in Anode-Supported Protonic Ceramic Fuel Cells. *J. Electrochem. Soc.* **2020**, *167*, 124506. [[CrossRef](#)]
182. Gao, J.; Meng, Y.; Lee, S.; Tong, J.; Brinkman, K.S. Effect of Infiltration of Barium Carbonate Nanoparticles on the Electrochemical Performance of  $\text{La}_{0.6}\text{Sr}_{0.4}\text{Co}_{0.2}\text{Fe}_{0.8}\text{O}_{3-\delta}$  Cathodes for Protonic Ceramic Fuel Cells. *JOM* **2019**, *71*, 90–95. [[CrossRef](#)]

183. Lai, Y.-W.; Lee, K.-R.; Yang, S.-Y.; Tseng, C.-J.; Jang, S.-C.; Tsao, I.-Y.; Chen, S.; Lee, S.-W. Production of  $\text{La}_{0.6}\text{Sr}_{0.4}\text{Co}_{0.2}\text{Fe}_{0.8}\text{O}_{3-\delta}$  Cathode with Graded Porosity for Improving Proton-Conducting Solid Oxide Fuel Cells. *Ceram. Int.* **2019**, *45*, 22479–22485. [[CrossRef](#)]
184. Fan, Y.; Xi, X.; Li, J.; Wang, Q.; Xiang, K.; Medvedev, D.; Luo, J.-L.; Fu, X.-Z. Barium-Doped  $\text{Sr}_2\text{Fe}_{1.5}\text{Mo}_{0.5}\text{O}_{6-\delta}$  Perovskite Anode Materials for Protonic Ceramic Fuel Cells for Ethane Conversion. *J. Am. Ceram. Soc.* **2022**, *105*, 3613–3624. [[CrossRef](#)]
185. Gao, Y.; Yang, Y.; Lin, X.; Fu, M.; Hu, W.; Tong, H.; Tao, Z. Investigation and Study of Three Different Composite Cathodes for Proton-Conducting Solid Oxide Fuel Cells. *Sep. Purif. Technol.* **2022**, *300*, 121890. [[CrossRef](#)]
186. Lee, H.; Lee, S.; Lee, T.; Park, S.; Shin, D. Long Term Stability of Porosity Gradient Composite Cathode Controlled by Electro-Static Slurry Spray Deposition. *Int. J. Hydrogen Energy* **2017**, *42*, 3748–3752. [[CrossRef](#)]
187. Hanif, M.B.; Rauf, S.; Abadeen, Z.U.; Khan, K.; Tayyab, Z.; Qayyum, S.; Mosialek, M.; Shao, Z.; Li, C.-X.; Motola, M. Proton-Conducting Solid Oxide Electrolysis Cells: Relationship of Composition-Structure-Property, Their Challenges, and Prospects. *Matter* **2023**, *6*, 1782–1830. [[CrossRef](#)]
188. Zayas-Rey, M.J.; Dos Santos-Gómez, L.; Porras-Vázquez, J.M.; Losilla, E.R.; Marrero-López, D. Evaluation of Lanthanum Tungstates as Electrolytes for Proton Conductors Solid Oxide Fuel Cells. *J. Power Sources* **2015**, *294*, 483–493. [[CrossRef](#)]
189. Marrero-López, D.; Martín-Sedeño, M.C.; Peña-Martínez, J.; Ruiz-Morales, J.C.; Núñez, P.; Aranda, M.A.G.; Ramos-Barrado, J.R. Evaluation of Apatite Silicates as Solid Oxide Fuel Cell Electrolytes. *J. Power Sources* **2010**, *195*, 2496–2506. [[CrossRef](#)]
190. Nesaraj, A.S.; Kumar, M.; Arul Raj, I.; Radhakrishna, I.; Pattabiraman, R. Investigations on Chemical Interactions between Alternate Cathodes and Lanthanum Gallate Electrolyte for Intermediate Temperature Solid Oxide Fuel Cell (ITSOFC). *J. Iran. Chem. Soc.* **2007**, *4*, 89–106. [[CrossRef](#)]
191. Giannici, F.; Chiara, A.; Canu, G.; Longo, A.; Martorana, A. Interface Solid-State Reactions in  $\text{La}_{0.8}\text{Sr}_{0.2}\text{MnO}_3/\text{Ce}_{0.8}\text{Sm}_{0.2}\text{O}_2$  and  $\text{La}_{0.8}\text{Sr}_{0.2}\text{MnO}_3/\text{BaCe}_{0.9}\text{Y}_{0.1}\text{O}_3$  Disclosed by X-ray Microspectroscopy. *ACS Appl. Energy Mater.* **2019**, *2*, 3204–3210. [[CrossRef](#)]
192. Lyagaeva, J.; Medvedev, D.; Pikalova, E.; Plaksin, S.; Brouzgou, A.; Demin, A.; Tsiakaras, P. A Detailed Analysis of Thermal and Chemical Compatibility of Cathode Materials Suitable for  $\text{BaCe}_{0.8}\text{Y}_{0.2}\text{O}_{3-\delta}$  and  $\text{BaZr}_{0.8}\text{Y}_{0.2}\text{O}_{3-\delta}$  Proton Electrolytes for Solid Oxide Fuel Cell Application. *Int. J. Hydrogen Energy* **2017**, *42*, 1715–1723. [[CrossRef](#)]
193. Pikalova, E.; Bogdanovich, N.; Kolchugin, A.; Brouzgou, A.; Bronin, D.; Plaksin, S.V.; Khasanov, A.; Tsiakaras, P. Effect of Nature of the Ceramic Component of the Composite Electrodes Based on  $\text{La}_{1.7}\text{Ca}(\text{Sr})_{0.3}\text{NiO}_{4+\delta}$  on Their Electrochemical Performance. *ECS Trans.* **2015**, *68*, 809–815. [[CrossRef](#)]
194. Antonova, E.P.; Kolchugin, A.A.; Pikalova, E.Y.; Medvedev, D.A.; Bogdanovich, N.M. Development of Electrochemically Active Electrodes for  $\text{BaCe}_{0.89}\text{Gd}_{0.1}\text{Cu}_{0.01}\text{O}_{3-\delta}$  Proton Conducting Electrolyte. *Solid State Ion.* **2017**, *306*, 55–61. [[CrossRef](#)]
195. Pikalova, E.Y.; Kolchugin, A.A. The Influence of the Substituting Element ( $M = \text{Ca}, \text{Sr}, \text{Ba}$ ) in  $\text{La}_{1.7}\text{M}_0.3\text{NiO}_{4+\delta}$  on the Electrochemical Performance of the Composite Electrodes. *Eur. Chem. Technol. J.* **2016**, *18*, 3. [[CrossRef](#)]
196. Pikalova, E.; Kolchugin, A.; Koroleva, M.; Vdovin, G.; Farlenkov, A.; Medvedev, D. Functionality of an Oxygen  $\text{Ca}_3\text{Co}_4\text{O}_{9+\delta}$  Electrode for Reversible Solid Oxide Electrochemical Cells Based on Proton-Conducting Electrolytes. *J. Power Sources* **2019**, *438*, 226996. [[CrossRef](#)]
197. Filonova, E.A.; Tokareva, E.S.; Pikalova, N.S.; Vylkov, A.I.; Bogdanovich, N.M.; Pikalova, E.Y. Assessment of Prospective Cathodes Based on  $(1-x)\text{Ca}_3\text{Co}_4\text{O}_{9+\delta}-x\text{BaCe}_{0.5}\text{Zr}_{0.3}\text{Y}_{0.1}\text{Yb}_{0.1}\text{O}_{3-\delta}$  Composites for Protonic Ceramic Electrochemical Cells. *J. Solid State Electrochem.* **2020**, *24*, 1509–1521. [[CrossRef](#)]
198. Chen, K.; Ai, N.; Jiang, S.P. Performance and Structural Stability of  $\text{Gd}_{0.2}\text{Ce}_{0.8}\text{O}_{1.9}$  Infiltrated  $\text{La}_{0.8}\text{Sr}_{0.2}\text{MnO}_3$  Nano-Structured Oxygen Electrodes of Solid Oxide Electrolysis Cells. *Int. J. Hydrogen Energy* **2014**, *39*, 10349–10358. [[CrossRef](#)]
199. Zha, S.; Zhang, Y.; Liu, M. Functionally Graded Cathodes Fabricated by Sol-Gel/Slurry Coating for Honeycomb SOFCs. *Solid State Ion.* **2005**, *176*, 25–31. [[CrossRef](#)]
200. Kammer Hansen, K.; Menon, M.; Knudsen, J.; Bonanos, N.; Mogensen, M. The Effect of a CGO Barrier Layer on the Performance of LSM/YSZ SOFC Cathodes. *J. Electrochem. Soc.* **2010**, *157*, B309. [[CrossRef](#)]
201. Recio, P.; Alcázar, C.; Moreno, R. Colloidal Processing of  $\text{Y}_{0.08}\text{Zr}_{0.92}\text{O}_2/\text{La}_{0.80}\text{Sr}_{0.20}\text{MnO}_3$  Semi-Cells Using a Sr-Doped Lanthanum Manganite Synthesized by a Citrate Route. *Materials* **2021**, *14*, 7831. [[CrossRef](#)]
202. Chen, M.; Moon, B.H.; Kim, S.H.; Kim, B.H.; Xu, Q.; Ahn, B.-G. Characterization of  $\text{La}_{0.6}\text{Sr}_{0.4}\text{Co}_{0.2}\text{Fe}_{0.8}\text{O}_{3-\delta} + \text{La}_2\text{NiO}_{4+\delta}$  Composite Cathode Materials for Solid Oxide Fuel Cells. *Fuel Cells* **2012**, *12*, 86–96. [[CrossRef](#)]
203. Chen, Y.; Chen, F.; Ding, D.; Gao, J. Development and Fabrication of a New Concept Planar-Tubular Solid Oxide Fuel Cell (PT-SOFC). *Fuel Cells* **2011**, *11*, 451–458. [[CrossRef](#)]
204. Zunic, M.; Chevallier, L.; Di Bartolomeo, E.; D’Epifanio, A.; Licocchia, S.; Traversa, E. Anode Supported Protonic Solid Oxide Fuel Cells Fabricated Using Electrophoretic Deposition. *Fuel Cells* **2011**, *11*, 165–171. [[CrossRef](#)]
205. Harboe, S.; Lupetin, P.; Guillon, O.; Menzler, N.H. Investigation of LSM/8YSZ Cathode within an All-Ceramic SOFC, Part II: Optimization of Performance and Co-Sinterability. *J. Eur. Ceram. Soc.* **2020**, *40*, 3618–3631. [[CrossRef](#)]
206. Liang, M.; Yu, B.; Wen, M.; Chen, J.; Xu, J.; Zhai, Y. Preparation of LSM–YSZ Composite Powder for Anode of Solid Oxide Electrolysis Cell and Its Activation Mechanism. *J. Power Sources* **2009**, *190*, 341–345. [[CrossRef](#)]
207. Gong, Y.; Ji, W.; Zhang, L.; Xie, B.; Wang, H. Performance of  $(\text{La},\text{Sr})\text{MnO}_3$  Cathode Based Solid Oxide Fuel Cells: Effect of Bismuth Oxide Sintering Aid in Silver Paste Cathode Current Collector. *J. Power Sources* **2011**, *196*, 928–934. [[CrossRef](#)]

208. Tanveer, W.H.; Rezk, H.; Nassef, A.; Abdelkareem, M.A.; Kolosz, B.; Karuppasamy, K.; Aslam, J.; Gilani, S.O. Improving Fuel Cell Performance via Optimal Parameters Identification through Fuzzy Logic Based-Modeling and Optimization. *Energy* **2020**, *204*, 117976. [\[CrossRef\]](#)
209. Pijolat, C. Screen-Printing for the Fabrication of Solid Oxide Fuel Cells (SOFC). In *Printed Films*; Elsevier: Amsterdam, The Netherlands, 2012; pp. 469–495. ISBN 978-1-84569-988-8.
210. Park, S.-C.; Lee, J.-J.; Lee, S.-H.; Moon, J.; Hyun, S.-H. Design and Preparation of SOFC Unit Cells Using Scandia-Stabilized Zirconia Electrolyte for Intermediate Temperature Operation. *J. Fuel Cell Sci. Technol.* **2011**, *8*, 044501. [\[CrossRef\]](#)
211. Li, D.; Jin, Y.; Liu, C.; Fu, M.; Zong, X.; Xiong, Y. Effect of Optimal GDC Loading on Long-Term Stability of  $\text{La}_{0.8}\text{Sr}_{0.2}\text{Co}_{0.2}\text{Fe}_{0.8}\text{O}_{3-\delta}/\text{Gd}_{0.2}\text{Ce}_{0.8}\text{O}_{1.9}$  Composite Cathodes. *Ceram. Int.* **2021**, *47*, 6591–6596. [\[CrossRef\]](#)
212. Cheng, L.; Sun, M.; Ye, F.; Bai, Y.; Li, M.; Fan, S.; Zhang, L. Structure Design, Fabrication, Properties of Laminated Ceramics: A Review. *Int. J. Lightweight Mater. Manufact.* **2018**, *1*, 126–141. [\[CrossRef\]](#)
213. Liu, T.; Lin, J.; Liu, T.; Wu, H.; Xia, C.; Chen, C.; Zhan, Z. Tailoring the Pore Structure of Cathode Supports for Improving the Electrochemical Performance of Solid Oxide Fuel Cells. *J. Electroceram.* **2018**, *40*, 138–143. [\[CrossRef\]](#)
214. Li, P.; Chen, X.; Sun, Y.; Chen, T.; Zhang, B.; Li, F.; Zhou, J.; Wang, S. Fabrication of Anode Supported Solid Oxide Electrolysis Cell with the Co-Tape Casting Technique and Study on Co-Electrolysis Characteristics. *J. Power Sources* **2023**, *569*, 232912. [\[CrossRef\]](#)
215. Won, B.-R.; Kim, Y.H.; Jo, S.; Myung, J. Highly Flexible Solid Oxide Fuel Cells Using Phase-Controlled Electrolyte Support. *J. Eur. Ceram. Soc.* **2022**, *42*, 5813–5819. [\[CrossRef\]](#)
216. Snowdon, A.L.; Jiang, Z.; Steinberger-Wilckens, R. Five-layer Reverse Tape Casting of IT-SOFC. *Int. J. Appl. Ceram. Technol.* **2022**, *19*, 289–298. [\[CrossRef\]](#)
217. Xu, N.; Geng, D.; Tong, X.; Sun, M.; Xu, Z. Fabrication and Characterization of Co-Fired Metal-Supported Solid Oxide Fuel Cells. *Solid State Ion.* **2020**, *358*, 115482. [\[CrossRef\]](#)
218. Shimada, H.; Fujimaki, Y.; Fujishiro, Y. Highly Active and Durable  $\text{La}_{0.4}\text{Sr}_{0.6}\text{MnO}_{3-\delta}$  and  $\text{Ce}_{0.8}\text{Gd}_{0.2}\text{O}_{1.9}$  Nanocomposite Electrode for High-Temperature Reversible Solid Oxide Electrochemical Cells. *Ceram. Int.* **2020**, *46*, 19617–19623. [\[CrossRef\]](#)
219. Zamudio-García, J.; Caizán-Juanarena, L.; Porras-Vázquez, J.M.; Losilla, E.R.; Marrero-López, D. Boosting the Performance of  $\text{La}_{0.8}\text{Sr}_{0.2}\text{MnO}_{3-\delta}$  Electrodes by the Incorporation of Nanocomposite Active Layers. *Adv. Mater. Int.* **2022**, *9*, 2200702. [\[CrossRef\]](#)
220. Vardavoulias, M.; Gkomoza, P.; Arkas, M.; Niakolas, D.K.; Neophytides, S.G. Thermal Spray Multilayer Ceramic Structures with Potential for Solid Oxide Cell Applications. *Coatings* **2021**, *11*, 682. [\[CrossRef\]](#)
221. Pyo, S.-S.; Lee, S.-B.; Lim, T.-H.; Song, R.-H.; Shin, D.-R.; Hyun, S.-H.; Yoo, Y.-S. Characteristic of  $(\text{La}_{0.8}\text{Sr}_{0.2})_{0.98}\text{MnO}_3$  Coating on Crofer22APU Used as Metallic Interconnects for Solid Oxide Fuel Cell. *Int. J. Hydrogen Energy* **2011**, *36*, 1868–1881. [\[CrossRef\]](#)
222. Lin, J.; Li, H.; Wang, W.; Qiu, P.; Tao, G.; Huang, K.; Chen, F. Atmospheric Plasma Spraying to Fabricate Metal-Supported Solid Oxide Fuel Cells with Open-Channel Porous Metal Support. *J. Am. Ceram. Soc.* **2023**, *106*, 68–78. [\[CrossRef\]](#)
223. dos Santos-Gómez, L.; Porras-Vázquez, J.M.; Martín, F.; Ramos-Barrado, J.R.; Losilla, E.R.; Marrero-López, D. A Novel Multilaminated Composite Cathode for Solid Oxide Fuel Cells. *Ceram. Int.* **2019**, *45*, 18124–18127. [\[CrossRef\]](#)
224. Wang, H.; Zhang, X.; Zhang, W.; Wei, Z.; Guan, K.; Meng, J.; Meng, F.; Meng, J.; Liu, X. Enhancing Catalysis Activity of  $\text{La}_{0.6}\text{Sr}_{0.4}\text{Co}_{0.8}\text{Fe}_{0.2}\text{O}_{3-\delta}$  Cathode for Solid Oxide Fuel Cell by a Facile and Efficient Impregnation Process. *Int. J. Hydrogen Energy* **2019**, *44*, 13757–13767. [\[CrossRef\]](#)
225. Ahamad, S.; Ahmad, M.; Mehta, B.R.; Gupta, A. Effect of Nano-Fillers on Capacity Retention and Rate Capability of Mesocarbon Microbeads Anode. *J. Electrochem. Soc.* **2017**, *164*, A2967–A2976. [\[CrossRef\]](#)
226. Verma, R.; Suri, N.M.; Kant, S. Effect of Parameters on Adhesion Strength for Slurry Spray Coating Technique. *Mater. Manufact. Proc.* **2017**, *32*, 416–424. [\[CrossRef\]](#)
227. Creanga, C.; Serban, S.; Pittson, R.; Murr, N.E. “No Calibration” Type Sensor in Routine Amperometric Bio-sensing: An Example of a Disposable Hydrogen Peroxide Biosensor. In *Biosensors—Emerging Materials and Applications*; InTechOpen: London, UK, 2011; pp. 141–152. [\[CrossRef\]](#)
228. Ren, L.; Luo, X.; Zhou, H. The Tape Casting Process for Manufacturing Low-temperature Co-fired Ceramic Green Sheets: A Review. *J. Am. Ceram. Soc.* **2018**, *101*, 3874–3889. [\[CrossRef\]](#)
229. Emley, B.; Panthi, D.; Du, Y.; Yao, Y. Controlling Porosity of Anode Support in Tubular Solid Oxide Fuel Cells by Freeze Casting. *J. Electrochem. Energy Convers. Storage* **2020**, *17*, 041008. [\[CrossRef\]](#)
230. Yao, Y.; Wang, C.; Ma, Y.; Ye, H.; Liu, Y.; Liu, J.; Zhao, X.; Tao, T.; Yao, Y.; Lu, S.; et al. Preparation and Performance of a Nano-Honeycomb Cathode for Microtubular Solid Oxide Fuel Cells. *Int. J. Hydrogen Energy* **2023**, *48*, 5229–5236. [\[CrossRef\]](#)
231. Sahu, S.K.; Panthi, D.; Feng, H.; Du, Y. Effect of Microstructure of the Anode Support Tubes towards SOFC Performance. In *Proceedings of the ECS Transactions*; IOP Publishing Ltd.: Bristol, UK, 2021; Volume 103, pp. 407–418.
232. Timurkutluk, C.; Yildirim, F.; Toruntay, F.; Onbilgin, S.; Yagiz, M.; Timurkutluk, B. Fabrication and Optimization of LSM Infiltrated Cathode Electrode for Anode Supported Microtubular Solid Oxide Fuel Cells. *Int. J. Hydrogen Energy* **2023**, *48*, 9833–9844. [\[CrossRef\]](#)
233. Panthi, D.; Choi, B.; Tsutsumi, A. A Novel Micro-Tubular Solid Oxide Fuel Cell with a Porous Zirconia Support for Intermediate-Temperature Operation. *ECS Trans.* **2015**, *68*, 2259–2265. [\[CrossRef\]](#)
234. Min, S.H.; Song, R.-H.; Lee, J.G.; Park, M.-G.; Ryu, K.H.; Jeon, Y.-K.; Shul, Y. Fabrication of Anode-Supported Tubular  $\text{Ba}(\text{Zr}_{0.1}\text{Ce}_{0.7}\text{Y}_{0.2})\text{O}_{3-\delta}$  Cell for Intermediate Temperature Solid Oxide Fuel Cells. *Ceram. Int.* **2014**, *40*, 1513–1518. [\[CrossRef\]](#)

235. Zhao, K.; Kim, B.-H.; Norton, M.G.; Ha, S.Y. Cathode Optimization for an Inert-Substrate-Supported Tubular Solid Oxide Fuel Cell. *Front. Energy Res.* **2018**, *6*, 87. [\[CrossRef\]](#)
236. Amiri, T.; Singh, K.; Sandhu, N.K.; Hanifi, A.R.; Etsell, T.H.; Luo, J.-L.; Thangadurai, V.; Sarkar, P. High Performance Tubular Solid Oxide Fuel Cell Based on  $\text{Ba}_{0.5}\text{Sr}_{0.5}\text{Ce}_{0.6}\text{Zr}_{0.2}\text{Gd}_{0.1}\text{Y}_{0.1}\text{O}_{3-\delta}$  Proton Conducting Electrolyte. *J. Electrochem. Soc.* **2018**, *165*, F764–F769. [\[CrossRef\]](#)
237. López-Robledo, M.J.; Laguna-Bercero, M.A.; Silva, J.; Orera, V.M.; Larrea, A. Electrochemical Performance of Intermediate Temperature Micro-Tubular Solid Oxide Fuel Cells Using Porous Ceria Barrier Layers. *Ceram. Int.* **2015**, *41*, 7651–7660. [\[CrossRef\]](#)
238. Mushtaq, U.; Kim, D.-W.; Yun, U.-J.; Lee, J.-W.; Lee, S.-B.; Park, S.-J.; Song, R.-H.; Kim, G.; Lim, T.-H. Effect of Cathode Geometry on the Electrochemical Performance of Flat Tubular Segmented-in-Series (SIS) Solid Oxide Fuel Cell. *Int. J. Hydrogen Energy* **2015**, *40*, 6207–6215. [\[CrossRef\]](#)
239. Ab Rahman, M.; Othman, M.H.D.; Fansuri, H.; Harun, Z.; Omar, A.F.; Shabri, H.A.; Ravi, J.; Rahman, M.A.; Jaafar, J.; Ismail, A.F.; et al. Development of High-Performance Anode/Electrolyte/Cathode Micro-Tubular Solid Oxide Fuel Cell via Phase Inversion-Based Co-Extrusion/Co-Sintering Technique. *J. Power Sources* **2020**, *467*, 228345. [\[CrossRef\]](#)
240. ur Rehman, S.; Song, R.-H.; Lee, J.-W.; Lim, T.-H.; Park, S.-J.; Lee, S.-B. Fabrication and Characterization of  $\text{La}_{0.65}\text{Sr}_{0.3}\text{MnO}_{3-\delta}/(\text{Y}_2\text{O}_3)_{0.08}(\text{ZrO}_2)_{0.92}/\text{Gd}_{0.1}\text{Ce}_{0.9}\text{O}_{2-\delta}$  Tri-Composite Cathode-Supported Tubular Direct Carbon Solid Oxide Fuel Cell. *Ceram. Int.* **2017**, *43*, 1086–1091. [\[CrossRef\]](#)
241. Ab Rahman, M.; Othman, M.H.D.; Fansuri, H.; Harun, Z.; Jamil, S.M.; Omar, A.F.; Rahman, M.A.; Jaafar, J.; Ismail, A.F. Effect of Sintering Temperature on Perovskite-Based Hollow Fiber as a Substrate for Cathode-Supported Micro-Tubular Solid Oxide Fuel Cell. *J. Aust. Ceram. Soc.* **2021**, *57*, 1199–1208. [\[CrossRef\]](#)
242. Wang, S.-F.; Hsu, Y.-F.; Hsia, P.; Hung, W.-K.; Jasinski, P. Design and Characterization of Apatite  $\text{La}_{9.8}\text{Si}_{5.7}\text{Mg}_{0.3}\text{O}_{26\pm\delta}$ -Based Micro-Tubular Solid Oxide Fuel Cells. *J. Power Sources* **2020**, *460*, 228072. [\[CrossRef\]](#)
243. Jamil, S.M.; Dzarfan Othman, M.H.; Mohamed, M.H.; Adam, M.R.; Rahman, M.A.; Jaafar, J.; Ismail, A.F. A Novel Single-Step Fabrication Anode/Electrolyte/Cathode Triple-Layer Hollow Fiber Micro-Tubular SOFC. *Int. J. Hydrogen Energy* **2018**, *43*, 18509–18515. [\[CrossRef\]](#)
244. López-Robledo, M.J.; Laguna-Bercero, M.A.; Larrea, A.; Orera, V.M. Reversible Operation of Microtubular Solid Oxide Cells Using  $\text{La}_{0.6}\text{Sr}_{0.4}\text{Co}_{0.2}\text{Fe}_{0.8}\text{O}_{3-\delta}-\text{Ce}_{0.9}\text{Gd}_{0.1}\text{O}_{2-\delta}$  Oxygen Electrodes. *J. Power Sources* **2018**, *378*, 184–189. [\[CrossRef\]](#)
245. Pikalova, E.Y.; Kalinina, E.G. Place of Electrophoretic Deposition among Thin-Film Methods Adapted to the Solid Oxide Fuel Cell Technology: A Short Review. *Int. J. Energy Prod. Manag.* **2019**, *4*, 1–27. [\[CrossRef\]](#)
246. Kalinina, E.G.; Pikalova, E.Y. New Trends in the Development of Electrophoretic Deposition Method in the Solid Oxide Fuel Cell Technology: Theoretical Approaches, Experimental Solutions and Development Prospects. *Russ. Chem. Rev.* **2019**, *88*, 1179–1219. [\[CrossRef\]](#)
247. Yamaji, T.; Itagaki, Y.; Arakawa, K.; Sadaoka, Y. Formation of  $\text{La}_{0.8}\text{Sr}_{0.2}\text{MnO}_3$  Films as SOFC Cathodes by Electrophoretic Deposition. *J. Ceram. Soc. Jpn.* **2010**, *118*, 1202–1206. [\[CrossRef\]](#)
248. Cherng, J.S.; Wu, C.C.; Chen, W.H.; Yeh, T.H. Microstructure and Performance of Micro-Tubular Solid Oxide Fuel Cells Made by Aqueous Electrophoretic Deposition. *Ceram. Int.* **2013**, *39*, S601–S604. [\[CrossRef\]](#)
249. Cherng, J.S.; Ho, M.Y.; Yeh, T.H.; Chen, W.H. Anode-Supported Micro-Tubular SOFCs Made by Aqueous Electrophoretic Deposition. *Ceram. Int.* **2012**, *38*, S477–S480. [\[CrossRef\]](#)
250. Salehzadeh, D.; Torabi, M.; Sadeghian, Z.; Marashi, P. A Multiscale-Architecture Solid Oxide Fuel Cell Fabricated by Electrophoretic Deposition Technique. *J. Alloys Compd.* **2020**, *830*, 154654. [\[CrossRef\]](#)
251. Santillán, M.J.; Caneiro, A.; Quaranta, N.; Boccaccini, A.R. Electrophoretic Deposition of  $\text{La}_{0.6}\text{Sr}_{0.4}\text{Co}_{0.8}\text{Fe}_{0.2}\text{O}_{3-\delta}$  Cathodes on  $\text{Ce}_{0.9}\text{Gd}_{0.1}\text{O}_{1.95}$  Substrates for Intermediate Temperature Solid Oxide Fuel Cell (IT-SOFC). *J. Eur. Ceram. Soc.* **2009**, *29*, 1125–1132. [\[CrossRef\]](#)
252. Santillán, M.J.; Caneiro, A.; Lovey, F.C.; Quaranta, N.; Boccaccini, A.R. Electrophoretic Codeposition of  $\text{La}_{0.6}\text{Sr}_{0.4}\text{Co}_{0.8}\text{Fe}_{0.2}\text{O}_{3-\delta}$  and Carbon Nanotubes for Developing Composite Cathodes for Intermediate Temperature Solid Oxide Fuel Cells. *Int. J. Appl. Ceram. Technol.* **2010**, *7*, 30–40. [\[CrossRef\]](#)
253. Baharuddin, N.A. Influence of Sintering Temperature on the Polarization Resistance of  $\text{La}_{0.6}\text{Sr}_{0.4}\text{Co}_{0.2}\text{Fe}_{0.8}\text{O}_{3-\delta}$ -SDC Carbonate Composite Cathode. *Ceram. Silikáty* **2016**, *60*, 115–121. [\[CrossRef\]](#)
254. Yamamoto, K.; Sato, K.; Matsuda, M.; Ozawa, M.; Ohara, S. Anomalous Low-Temperature Sintering of a Solid Electrolyte Thin Film of Tailor-Made Nanocrystals on a Porous Cathode Support for Low-Temperature Solid Oxide Fuel Cells. *Ceram. Int.* **2021**, *47*, 15939–15946. [\[CrossRef\]](#)
255. Tsai, H.-C.; Chang, Y.-T.; Wu, P.-W.; Lin, P. Fabrication of Tri-Layered Structure for Solid Oxide Fuel Cells by Electrophoretic Depositions. *ECS Trans.* **2009**, *25*, 643–648. [\[CrossRef\]](#)
256. Itagaki, Y.; Watanabe, S.; Yamaji, T.; Asamoto, M.; Yahiro, H.; Sadaoka, Y. Electrophoretic Deposition of Bi-Layered LSM/LSM-YSZ Cathodes for Solid Oxide Fuel Cell. *J. Power Sources* **2012**, *214*, 153–158. [\[CrossRef\]](#)
257. Ji, Q.; Xu, X.; Liu, X.; Bi, L. Improvement of the Catalytic Properties of Porous Lanthanum Manganite for the Oxygen Reduction Reaction by Partial Substitution of Strontium for Lanthanum. *Electrochem. Commun.* **2021**, *124*, 106964. [\[CrossRef\]](#)
258. Torabi, A.; Hanifi, A.R.; Etsell, T.H.; Sarkar, P. Effects of Porous Support Microstructure on Performance of Infiltrated Electrodes in Solid Oxide Fuel Cells. *J. Electrochem. Soc.* **2011**, *159*, B201–B210. [\[CrossRef\]](#)
259. Benipayo, A.B.; Cervera, R.B.M. Influence of Carbon Black Pore Former on the Synthesis of LSM-YSZ Composite Electrode Material via Solid-State Reaction and Glycine-Nitrate Process. *Mater. Sci. Forum* **2019**, *950*, 154–159. [\[CrossRef\]](#)

260. Noh, J.H.; Myung, J. Optimization of Anode and Electrolyte Microstructure for Solid Oxide Fuel Cells. *Korean Chem. Eng. Res.* **2019**, *57*, 525–530. [[CrossRef](#)]
261. Wu, S.; Tan, W.; Peng, Y.; Gao, J.; Shi, H.; Qu, J.; Zhu, X. Electrochemical Reduction of Nitric Oxide in Different Carbon-Driven Solid State Cells. *J. Alloys Compd.* **2020**, *812*, 152163. [[CrossRef](#)]
262. Nie, L.; Liu, J.; Zhang, Y.; Liu, M. Effects of Pore Formers on Microstructure and Performance of Cathode Membranes for Solid Oxide Fuel Cells. *J. Power Sources* **2011**, *196*, 9975–9979. [[CrossRef](#)]
263. Mohamed, R.; Cheng, X.; Fabbri, E.; Levecque, P.; Kötz, R.; Conrad, O.; Schmidt, T.J. Electrocatalysis of Perovskites: The Influence of Carbon on the Oxygen Evolution Activity. *J. Electrochem. Soc.* **2015**, *162*, F579–F586. [[CrossRef](#)]
264. Safakas, A.; Bampos, G.; Bebelis, S. Oxygen Reduction Reaction on  $\text{La}_{0.8}\text{Sr}_{0.2}\text{Co}_x\text{Fe}_{1-x}\text{O}_{3-\delta}$  Perovskite/Carbon Black Electrocatalysts in Alkaline Medium. *Appl. Catal. B Environ.* **2019**, *244*, 225–232. [[CrossRef](#)]
265. Ding, H.; Xue, X. A Platinum Nanowire Network as a Highly Efficient Current Collector for Intermediate Temperature Solid Oxide Fuel Cells. *RSC Adv.* **2014**, *4*, 11317–11321. [[CrossRef](#)]
266. Burmistrov, I.N.; Agarkov, D.A.; Tsybrov, F.M.; Bredikhin, S.I. Preparation of Membrane-Electrode Assemblies of Solid Oxide Fuel Cells by Co-Sintering of Electrodes. *Russ. J. Electrochem.* **2016**, *52*, 669–677. [[CrossRef](#)]
267. Burmistrov, I.N.; Agarkov, D.A.; Korovkin, E.V.; Yalovenko, D.V.; Bredikhin, S.I. Fabrication of Membrane–Electrode Assemblies for Solid-Oxide Fuel Cells by Joint Sintering of Electrodes at High Temperature. *Russ. J. Electrochem.* **2017**, *53*, 873–879. [[CrossRef](#)]
268. Zhang, X.; Yu, G.; Zeng, S.; Parbey, J.; Xiao, S.; Li, B.; Li, T.; Andersson, M. Mechanism of Chromium Poisoning the Conventional Cathode Material for Solid Oxide Fuel Cells. *J. Power Sources* **2018**, *381*, 26–29. [[CrossRef](#)]
269. He, Z.; Andersen, K.B.; Keel, L.; Nygaard, F.B.; Menon, M.; Hansen, K.K. Processing and Characterization of Porous Electrochemical Cells for Flue Gas Purification. *Ionics* **2009**, *15*, 427–431. [[CrossRef](#)]
270. Abd Mutalib, M.; Othman, M.H.D.; Aziz, M.; Rahman, M.A.; Jaafar, J.; Ismail, A.F.; Mohamed, M.A. The Influence of PEEK as a Pore Former on the Microstructure of Brush-Painted LSCF Cathodes. *J. Solid State Electrochem.* **2016**, *20*, 2895–2905. [[CrossRef](#)]
271. Duan, N.-Q.; Tan, Y.; Yan, D.; Jia, L.; Chi, B.; Pu, J.; Li, J. Biomass Carbon Fueled Tubular Solid Oxide Fuel Cells with Molten Antimony Anode. *Appl. Energy* **2016**, *165*, 983–989. [[CrossRef](#)]
272. Chen, M.; Kim, B.H.; Xu, Q.; Ahn, B.G.; Huang, D.P. Fabrication and Performance of Anode-Supported Solid Oxide Fuel Cells via Slurry Spin Coating. *J. Membr. Sci.* **2010**, *360*, 461–468. [[CrossRef](#)]
273. dos Santos-Gómez, L.; Zamudio-García, J.; Porras-Vázquez, J.M.; Losilla, E.R.; Marrero-López, D. Recent Progress in Nanostructured Electrodes for Solid Oxide Fuel Cells Deposited by Spray Pyrolysis. *J. Power Sources* **2021**, *507*, 230277. [[CrossRef](#)]
274. dos Santos-Gómez, L.; Zamudio-García, J.; Porras-Vázquez, J.M.; Losilla, E.R.; Marrero-López, D. Highly Efficient  $\text{La}_{0.8}\text{Sr}_{0.2}\text{MnO}_{3-\delta}-\text{Ce}_{0.9}\text{Gd}_{0.1}\text{O}_{1.95}$  Nanocomposite Cathodes for Solid Oxide Fuel Cells. *Ceram. Int.* **2018**, *44*, 4961–4966. [[CrossRef](#)]
275. Kumari, N.; Haider, M.A.; Anjum, U.; Basu, S. Identifying Operating Mechanism in the Electrochemical Reduction of  $\text{CO}_2$  on Thin-Film Praseodymium-Doped Ceria Electrodes. *Ionics* **2020**, *26*, 5673–5684. [[CrossRef](#)]
276. Krestou, A.; Barmatsis, A.; Tsanaktisidis, C.; Matsouka, C.; Nalbandian, L.; Kiratzis, N.E. Fabrication and Characterization of Functional Ceramic Films by Solution Spray Pyrolysis: Correlations with the Thermal Decomposition Characteristics of the Constituent Salts. *ECS Trans.* **2021**, *103*, 123–138. [[CrossRef](#)]
277. Sharma, R.K.; Khamidi, N.I.; Rapenne, L.; Charlot, F.; Moussaoui, H.; Laurencin, J.; Djurado, E. Highly Efficient Architected  $\text{Pr}_6\text{O}_{11}$  Oxygen Electrode for Solid Oxide Fuel Cell. *J. Power Sources* **2019**, *419*, 171–180. [[CrossRef](#)]
278. Castro-Robles, J.D.; Soltani, N.; Chávez-Carvayar, J.Á. Structural, Morphological and Transport Properties of Nanostructured  $\text{La}_{1-x}\text{Sr}_x\text{Co}_{0.2}\text{Fe}_{0.8}\text{O}_{3-\delta}$  Thin Films, Deposited by Ultrasonic Spray Pyrolysis. *Mater. Chem. Phys.* **2019**, *225*, 50–54. [[CrossRef](#)]
279. dos Santos-Gómez, L.; Zamudio-García, J.; Porras-Vázquez, J.M.; Losilla, E.R.; Marrero-López, D. Highly Oriented and Fully Dense CGO Films Prepared by Spray-Pyrolysis and Different Precursor Salts. *J. Eur. Ceram. Soc.* **2020**, *40*, 3080–3088. [[CrossRef](#)]
280. Kamecki, B.; Karczewski, J.; Jasiński, P.; Molin, S. Improvement of Oxygen Electrode Performance of Intermediate Temperature Solid Oxide Cells by Spray Pyrolysis Deposited Active Layers. *Adv. Mater. Interfaces* **2021**, *8*, 2002227. [[CrossRef](#)]
281. Zamudio-García, J.; Caizán-Juanarena, L.; Porras-Vázquez, J.M.; Losilla, E.R.; Marrero-López, D. Unraveling the Influence of the Electrolyte on the Polarization Resistance of Nanostructured  $\text{La}_{0.6}\text{Sr}_{0.4}\text{Co}_{0.2}\text{Fe}_{0.8}\text{O}_{3-\delta}$  Cathodes. *Nanomaterials* **2022**, *12*, 3936. [[CrossRef](#)]
282. Aruna, S.T.; Balaji, L.S.; Kumar, S.S.; Prakash, B.S. Electrospinning in Solid Oxide Fuel Cells—A Review. *Renew. Sustain. Energy Rev.* **2017**, *67*, 673–682. [[CrossRef](#)]
283. Parbey, J.; Wang, Q.; Yu, G.; Zhang, X.; Li, T.; Andersson, M. Progress in the Use of Electrospun Nanofiber Electrodes for Solid Oxide Fuel Cells: A Review. *Rev. Chem. Eng.* **2020**, *36*, 879–931. [[CrossRef](#)]
284. Liu, Z.; Gu, Y.; Bi, L. Applications of Electrospun Nanofibers in Solid Oxide Fuel Cells—A Review. *J. Alloys Compd.* **2023**, *937*, 168288. [[CrossRef](#)]
285. Squizzato, E.; Sanna, C.; Glisenti, A.; Costamagna, P. Structural and Catalytic Characterization of  $\text{La}_{0.6}\text{Sr}_{0.4}\text{MnO}_3$  Nanofibers for Application in Direct Methane Intermediate Temperature Solid Oxide Fuel Cell Anodes. *Energies* **2021**, *14*, 3602. [[CrossRef](#)]
286. Gong, J.; Wu, P.; Bai, Z.; Ma, J.; Li, T.; Yao, Y.; Jiang, C. Insight into the Electrospinning Process for SOFC Cathode Nanofibers. *J. Phys. Chem. C* **2021**, *125*, 7044–7053. [[CrossRef](#)]

287. Enrico, A.; Zhang, W.; Lund Traulsen, M.; Sala, E.M.; Costamagna, P.; Holtappels, P.  $\text{La}_{0.6}\text{Sr}_{0.4}\text{Co}_{0.2}\text{Fe}_{0.8}\text{O}_{3-\delta}$  Nanofiber Cathode for Intermediate-Temperature Solid Oxide Fuel Cells by Water-Based Sol-Gel Electrospinning: Synthesis and Electrochemical Behaviour. *J. Eur. Ceram. Soc.* **2018**, *38*, 2677–2686. [[CrossRef](#)]
288. Li, D.; Liu, C.J.; Su, D.L.; Dai, C.S.; Xiong, Y.P. Effect of Microstructure on Electrochemical Performance of Nano-Structured  $\text{La}_{0.8}\text{Sr}_{0.2}\text{Co}_{0.2}\text{Fe}_{0.8}\text{O}_{3-\delta}$ - $\text{Gd}_{0.2}\text{Ce}_{0.8}\text{O}_{1.9}$  Composite Cathodes. In *Proceedings of the ECS Transactions*; Eguchi, K., Singhal, S.C., Eds.; Electrochemical Society Inc.: Philadelphia, PA, USA, 2019; Volume 91, pp. 1483–1489.
289. Zhang, W.; Wang, H.; Guan, K.; Wei, Z.; Zhang, X.; Meng, J.; Liu, X.; Meng, J.  $\text{La}_{0.6}\text{Sr}_{0.4}\text{Co}_{0.2}\text{Fe}_{0.8}\text{O}_{3-\delta}/\text{CeO}_2$  Heterostructured Composite Nanofibers as a Highly Active and Robust Cathode Catalyst for Solid Oxide Fuel Cells. *ACS Appl. Mater. Interfaces* **2019**, *11*, 26830–26841. [[CrossRef](#)] [[PubMed](#)]
290. Sanna, C.; Zhang, W.; Costamagna, P.; Holtappels, P. Synthesis and Electrochemical Characterization of  $\text{La}_{0.6}\text{Sr}_{0.4}\text{Co}_{0.2}\text{Fe}_{0.8}\text{O}_{3-\delta}/\text{Ce}_{0.9}\text{Gd}_{0.1}\text{O}_{1.95}$  Co-Electrospun Nanofiber Cathodes for Intermediate-Temperature Solid Oxide Fuel Cells. *Int. J. Hydrogen Energy* **2021**, *46*, 13818–13831. [[CrossRef](#)]
291. Bai, J.; Zhou, D.; Zhu, X.; Wang, N.; Chen, R.; Wang, B. New SOFC Cathode: 3D Core-Shell-Structured  $\text{La}_{0.6}\text{Sr}_{0.4}\text{Co}_{0.2}\text{Fe}_{0.8}\text{O}_{3-\delta}@\text{PrO}_2-\delta$  Nanofibers Prepared by Coaxial Electrospinning. *ACS Appl. Energy Mater.* **2022**, *5*, 11178–11190. [[CrossRef](#)]
292. Chen, S.-H.; Zhang, T.-T.; Zhu, D.-Y.; Wang, N.; Xu, S.; Ramakrishna, S.; Long, Y.-Z. Synthesis and Electrochemical Characterization of  $\text{La}_{0.6}\text{Sr}_{0.4}\text{Co}_{0.2}\text{Fe}_{0.8}\text{O}_{3-\delta}$  and  $\text{BaZr}_{0.8}\text{Y}_{0.2}\text{O}_{3-\delta}$  Electrospun Nanofiber Cathodes for Solid Oxide Fuel Cells. *Adv. Eng. Mater.* **2022**, *24*, 2101083. [[CrossRef](#)]
293. Hedayat, N.; Du, Y. Micro-Tubular Solid Oxide Fuel Cells with One Closed-End Fabricated via Dip-Coating and Co-Firing. *ECS Trans.* **2021**, *103*, 113–121. [[CrossRef](#)]
294. Anelli, S.; Baiutti, F.; Hornés, A.; Bernadet, L.; Torrell, M.; Tarancón, A. Improved Mesostructured Oxygen Electrodes for Highly Performing Solid Oxide Cells for Co-Electrolysis of Steam and Carbon Dioxide. *J. Mater. Chem. A* **2019**, *7*, 27458–27468. [[CrossRef](#)]
295. Yan, Z.; He, A.; Hara, S.; Shikazono, N. In-Silico Design of Functionally Graded Electrodes for Solid Oxide Fuel Cells. In *Proceedings of the ECS Transactions*; Eguchi, K., Singhal, S.C., Eds.; Electrochemical Society Inc.: Philadelphia, PA, USA, 2019; Volume 91, pp. 2055–2064.
296. Muhoza, S.P.; Gross, M.D. Creating and Preserving Nanoparticles during Co-Sintering of Solid Oxide Electrodes and Its Impact on Electrocatalytic Activity. *Catalysts* **2021**, *11*, 1073. [[CrossRef](#)]
297. Muhoza, S.P.; Taylor, T.H.; Song, X.; Gross, M.D. The Impact of Sintering Atmosphere and Temperature on the Phase Evolution of High Surface Area LSCF Prepared by in Situ Carbon Templating. *J. Electrochem. Soc.* **2021**, *168*, 034519. [[CrossRef](#)]
298. Hedayat, N.; Du, Y.; Ilkhani, H. Review on Fabrication Techniques for Porous Electrodes of Solid Oxide Fuel Cells by Sacrificial Template Methods. *Renew. Sustain. Energy Rev.* **2017**, *77*, 1221–1239. [[CrossRef](#)]
299. Kim, S.; Kim, G.; Manthiram, A. A Review on Infiltration Techniques for Energy Conversion and Storage Devices: From Fundamentals to Applications. *Sustain. Energy Fuels* **2021**, *5*, 5024–5037. [[CrossRef](#)]
300. Vohs, J.M.; Gorte, R.J. High-Performance SOFC Cathodes Prepared by Infiltration. *Adv. Mater.* **2009**, *21*, 943–956. [[CrossRef](#)]
301. Biswas, S.; Kaur, G.; Paul, G.; Giddey, S. A Critical Review on Cathode Materials for Steam Electrolysis in Solid Oxide Electrolysis. *Int. J. Hydrogen Energy* **2023**, *48*, 12541–12570. [[CrossRef](#)]
302. He, S.; Zou, Y.; Chen, K.; Li, N.; Li, D.; Jiang, S.P. A Critical Review of the Nano-Structured Electrodes of Solid Oxide Cells. *Chem. Commun.* **2022**, *58*, 10619–10626. [[CrossRef](#)] [[PubMed](#)]
303. Chen, Y.; Liang, L.; Paredes Navia, S.A.; Hinerman, A.; Gerdes, K.; Song, X. Synergetic Interaction of Additive Dual Nanocatalysts to Accelerate Oxygen Reduction Reaction in Fuel Cell Cathodes. *ACS Catal.* **2019**, *9*, 6664–6671. [[CrossRef](#)]
304. Zhang, S.-L.; Wang, H.; Yang, T.; Lu, M.Y.; Barnett, S.A. Characteristics of Oxygen Electrode Supported Reversible Solid Oxide Cells. *J. Electrochem. Soc.* **2021**, *168*, 054504. [[CrossRef](#)]
305. Han, F.-Z.; Zhang, J.-H.; Zhang, S.-L.; Li, C.-X. Comparative Study on the Electrochemical Performance of  $\text{Sr}(\text{Ti}_{0.3}\text{Fe}_{0.7})\text{O}_{3-\delta}$  Fuel Electrode in Different Fuel Gases for Solid Oxide Electrochemical Cells. *Ceram. Int.* **2023**, *49*, 2410–2418. [[CrossRef](#)]
306. Orera, A.; Betato, A.; Silva-Treviño, J.; Larrea, Á.; Laguna-Bercero, M.Á. Advanced Metal Oxide Infiltrated Electrodes for Boosting the Performance of Solid Oxide Cells. *J. Mater. Chem. A* **2022**, *10*, 2541–2549. [[CrossRef](#)]
307. Tian, Y.; Wu, P.; Zhang, X.; Ding, L.; Li, Y.; Wu, X. Characterization of  $\text{La}_{0.65}\text{Sr}_{0.35}\text{MnO}_3$ -Based Double-Layered Oxygen Electrode for Reversible Solid Oxide Cells. *Ionics* **2022**, *28*, 801–812. [[CrossRef](#)]
308. Koo, J.Y.; Mun, T.; Lee, J.; Choi, M.; Kim, S.J.; Lee, W. Enhancement of Oxygen Reduction Reaction Kinetics Using Infiltrated Yttria-Stabilized Zirconia Interlayers at the Electrolyte/Electrode Interfaces of Solid Oxide Fuel Cells. *J. Power Sources* **2020**, *472*, 228606. [[CrossRef](#)]
309. Zhang, Y.; Yan, F.; Yan, M.; Wan, Y.; Jiao, Z.; Xia, C.; Chen, F.; Ni, M. High-Throughput, Super-Resolution 3D Reconstruction of Nano-Structured Solid Oxide Fuel Cell Electrodes and Quantification of Microstructure-Property Relationships. *J. Power Sources* **2019**, *427*, 112–119. [[CrossRef](#)]
310. Wan, S.; Yan, M.; Zhang, Y. A Numerical Study of Infiltrated Solid Oxide Fuel Cell Electrode with Dual-phase Backbone. *Int. J. Energy Res.* **2019**, *43*, 2562–2570. [[CrossRef](#)]
311. Kim, S.J.; Koo, J.Y.; Mun, T.; Choi, M.; Lee, W. Tailoring Defect Chemistry at Interfaces for Promoted Oxygen Reduction Reaction Kinetics. *J. Mater. Chem. A* **2020**, *8*, 23313–23322. [[CrossRef](#)]
312. Yang, T.; Kollasch, S.L.; Grimes, J.; Xue, A.; Barnett, S.A.  $(\text{La}_{0.8}\text{Sr}_{0.2})_{0.98}\text{MnO}_{3-\delta}$ - $\text{Zr}_{0.92}\text{Y}_{0.16}\text{O}_{2-\delta}$ :PrOx for Oxygen Electrode Supported Solid Oxide Cells. *Appl. Catal. B Environ.* **2022**, *306*, 121114. [[CrossRef](#)]

313. Lu, M.Y.; Scipioni, R.; Park, B.-K.; Yang, T.; Chart, Y.A.; Barnett, S.A. Mechanisms of PrOx Performance Enhancement of Oxygen Electrodes for Low and Intermediate Temperature Solid Oxide Fuel Cells. *Mater. Today Energy* **2019**, *14*, 100362. [[CrossRef](#)]
314. Zhao, X.; Yan, Y.; Li, M.; Ding, X. In-Situ Strategy to Suppress Chromium Poisoning on  $\text{La}_{0.6}\text{Sr}_{0.4}\text{Co}_{0.2}\text{Fe}_{0.8}\text{O}_{3-\delta}$  Cathodes of Solid Oxide Fuel Cells. *Int. J. Hydrogen Energy* **2019**, *44*, 30401–30408. [[CrossRef](#)]
315. Soltanizade, A.; Babaei, A.; Ataie, A.; Seyed-Vakili, S.V. Temperature Dependency of Activity of Nano-Catalysts on  $\text{La}_{0.6}\text{Sr}_{0.4}\text{Co}_{0.2}\text{Fe}_{0.8}\text{O}_{3-\delta}$  Cathode of Solid Oxide Fuel Cells. *J. Appl. Electrochem.* **2019**, *49*, 1113–1122. [[CrossRef](#)]
316. Sındıraç, C.; Büyükaksoy, A.; Akkurt, S. Electrochemical Performance of  $\text{La}_{0.6}\text{Sr}_{0.4}\text{Co}_{0.2}\text{Fe}_{0.8}\text{O}_{3-\delta}\text{Ce}_{0.9}\text{Gd}_{0.1}\text{O}_{2-\delta}$  Composite SOFC Cathodes Fabricated by Electrocatalyst and/or Electrocatalyst-Ionic Conductor Infiltration. *J. Sol Gel Sci. Technol.* **2019**, *92*, 45–56. [[CrossRef](#)]
317. Huang, Z.; Qi, H.; Zhao, Z.; Shang, L.; Tu, B.; Cheng, M. Efficient CO<sub>2</sub> Electroreduction on a Solid Oxide Electrolysis Cell with  $\text{La}_{0.6}\text{Sr}_{0.4}\text{Co}_{0.2}\text{Fe}_{0.8}\text{O}_{3-\delta}\text{Gd}_{0.2}\text{Ce}_{0.8}\text{O}_{2-\delta}$  Infiltrated Electrode. *J. Power Sources* **2019**, *434*, 226730. [[CrossRef](#)]
318. Ge, L.; Sun, K.; Gu, Y.; Ni, Q.; Huang, X. Boosting the Performance of Conventional Air Electrodes for Solid Oxide Cells by In-Situ Loading of Nano Praseodymium Oxide. *Energy Convers. Manag.* **2021**, *249*, 114873. [[CrossRef](#)]
319. Brito, M.E.; Morishita, H.; Yamada, J.; Nishino, H.; Uchida, H. Further Improvement in Performances of  $\text{La}_{0.6}\text{Sr}_{0.4}\text{Co}_{0.2}\text{Fe}_{0.8}\text{O}_{3-\delta}$ —Doped Ceria Composite Oxygen Electrodes with Infiltrated Doped Ceria Nanoparticles for Reversible Solid Oxide Cells. *J. Power Sources* **2019**, *427*, 293–298. [[CrossRef](#)]
320. Chen, X.; Ni, W.; Du, X.; Sun, Z.; Zhu, T.; Zhong, Q.; Han, M. Electrochemical Property of Multi-Layer Anode Supported Solid Oxide Fuel Cell Fabricated through Sequential Tape-Casting and Co-Firing. *J. Mater. Sci. Technol.* **2019**, *35*, 695–701. [[CrossRef](#)]
321. Zhang, Y.; Xu, N.; Fan, H.; Han, M.  $\text{La}_{0.6}\text{Sr}_{0.4}\text{Co}_{0.2}\text{Fe}_{0.8}\text{O}_{3-\delta}$  Nanoparticles Modified Ni-Based Anode for Direct Methane-Fueled SOFCs. In *Proceedings of the Energy Procedia*; Li, H., Yan, J., Yang, H.-X., Chen, X., Eds.; Elsevier Ltd.: Amsterdam, The Netherlands, 2019; Volume 158, pp. 2250–2255.
322. Fatah, A.F.B.M.A.; Murat, M.N.; Hamid, N.A. Lscf-Cuo as Promising Cathode for It Sofc. *J. Eng. Technol. Sci.* **2021**, *53*, 210411. [[CrossRef](#)]
323. Wang, Z.; Sun, H.; Li, J.; Guo, X.; Hu, Q.; Yang, Z.; Yu, F.; Li, G. Modified  $\text{La}_{0.6}\text{Sr}_{0.4}\text{Co}_{0.2}\text{Fe}_{0.8}\text{O}_{3-\delta}$  Cathodes with the Infiltration of  $\text{Er}_{0.4}\text{Bi}_{1.6}\text{O}_3$  for Intermediate-Temperature Solid Oxide Fuel Cells. *Int. J. Hydrogen Energy* **2021**, *46*, 22932–22941. [[CrossRef](#)]
324. Zhang, Y.; Nicholas, J.D. Evidence That Surface-Segregated Sr Phases Can Be Removed in LSCF via Ceria Pre-Infiltration, Are Less Apt to Form in SSC. *J. Electrochem. Soc.* **2021**, *168*, 024522. [[CrossRef](#)]
325. Nadeem, M.; Li, Y.; Bouwmeester, H.J.M.; Xia, C. PbO Effect on the Oxygen Reduction Reaction in Intermediate-Temperature Solid Oxide Fuel Cell. *Int. J. Hydrogen Energy* **2020**, *45*, 25299–25306. [[CrossRef](#)]
326. Qiu, P.; Yang, X.; Zou, L.; Zhu, T.; Yuan, Z.; Jia, L.; Li, J.; Chen, F.  $\text{LaCrO}_3$ -Coated  $\text{La}_{0.6}\text{Sr}_{0.4}\text{Co}_{0.2}\text{Fe}_{0.8}\text{O}_{3-\delta}$  Core-Shell Structured Cathode with Enhanced Cr Tolerance for Intermediate-temperature Solid Oxide Fuel Cells. *ACS Appl. Mater. Interfaces* **2020**, *12*, 29133–29142. [[CrossRef](#)]
327. Park, B.-K.; Barnett, S.A. Boosting Solid Oxide Fuel Cell Performance: Via Electrolyte Thickness Reduction and Cathode Infiltration. *J. Mater. Chem. A* **2020**, *8*, 11626–11631. [[CrossRef](#)]
328. Namgung, Y.; Hong, J.; Kumar, A.; Lim, D.-K.; Song, S.-J. One Step Infiltration Induced Multi-Cation Oxide Nanocatalyst for Load Proof SOFC Application. *Appl. Catal. B Environ.* **2020**, *267*, 118374. [[CrossRef](#)]
329. Song, Y.-H.; Rehman, S.U.; Kim, H.-S.; Song, H.-S.; Song, R.-H.; Lim, T.-H.; Hong, J.-E.; Park, S.-J.; Huh, J.-Y.; Lee, S.-B. Facile Surface Modification of LSCF/GDC Cathodes by Epitaxial Deposition of  $\text{Sm}_{0.5}\text{Sr}_{0.5}\text{CoO}_3$  via Ultrasonic Spray Infiltration. *J. Mater. Chem. A* **2020**, *8*, 3967–3977. [[CrossRef](#)]
330. Zhang, Y.; Han, M.; Sun, Z. High Performance and Stability of Nanocomposite Oxygen Electrode for Solid Oxide Cells. *Int. J. Hydrogen Energy* **2020**, *45*, 5554–5564. [[CrossRef](#)]
331. Akbari, Z.; Babaei, A. Electrochemical Performance of  $\text{La}_{0.8}\text{Sr}_{0.2}\text{MnO}_3$  Oxygen Electrode Promoted by Ruddlesden-Popper Structured  $\text{La}_2\text{NiO}_4$ . *J. Am. Ceram. Soc.* **2020**, *103*, 1332–1342. [[CrossRef](#)]
332. Khoshkalam, M.; Faghihi-Sani, M.A.; Tong, X.; Chen, M.; Hendriksen, P.V. Enhanced Activity of  $\text{Pr}_6\text{O}_{11}$  and CuO Infiltrated  $\text{Ce}_{0.9}\text{Gd}_{0.1}\text{O}_2$  Based Composite Oxygen Electrodes. *J. Electrochem. Soc.* **2020**, *167*, 024505. [[CrossRef](#)]
333. Fatah, A.F.; Mohamad, A.A.; Muchtar, A.; Hamid, N.A. Physical Characterization of LSCF–CuO via Enhanced Modified Sol-Gel Method for Intermediate Temperature Solid Oxide Fuel Cells (IT-SOFCs). *Mater. Today Proc.* **2020**, *46*, 2052–2057. [[CrossRef](#)]
334. Rosli, A.Z.; Somalu, M.R.; Osman, N.; Hamid, N.A. Physical Characterization of LSCF–NiO as Cathode Material for Intermediate Temperature Solid Oxide Fuel Cell (IT-SOFCs). *Mater. Today Proc.* **2020**, *46*, 1895–1900. [[CrossRef](#)]
335. Ghamarinia, M.; Babaei, A.; Zamani, C. Electrochemical Characterization of  $\text{La}_2\text{NiO}_4$ -Infiltrated  $\text{La}_{0.6}\text{Sr}_{0.4}\text{Co}_{0.2}\text{Fe}_{0.8}\text{O}_{3-\delta}$  by Analysis of Distribution of Relaxation Times. *Electrochim. Acta* **2020**, *353*, 136520. [[CrossRef](#)]
336. Lu, M.Y.; Yang, T.; Scipioni, R.; Chart, Y.A.; Furlong, A.; Barnett, S.A.  $\text{Sm}_{0.5}\text{Sr}_{0.5}\text{CoO}_{3-\delta}$  Surface Modification of  $\text{La}_{0.6}\text{Sr}_{0.4}\text{Co}_{0.2}\text{Fe}_{0.8}\text{O}_{3-\delta}\text{Ce}_{0.9}\text{Gd}_{0.1}\text{O}_{2-\delta}$  Composite Oxygen Electrodes for Solid Oxide Electrochemical Cells. *J. Electrochem. Soc.* **2020**, *167*, 164504. [[CrossRef](#)]
337. Kim, M.; Kim, D.H.; Han, G.D.; Choi, H.J.; Choi, H.R.; Shim, J.H. Lanthanum Strontium Cobaltite-Infiltrated Lanthanum Strontium Cobalt Ferrite Cathodes Fabricated by Inkjet Printing for High-Performance Solid Oxide Fuel Cells. *J. Alloys Compd.* **2020**, *843*, 155806. [[CrossRef](#)]

338. Hong, J.; Bhardwaj, A.; Namgung, Y.; Bae, H.; Song, S.-J. Evaluation of the Effects of Nanocatalyst Infiltration on the SOFC Performance and Electrode Reaction Kinetics Using the Transmission Line Model. *J. Mater. Chem. A* **2020**, *8*, 23473–23487. [[CrossRef](#)]
339. Rehman, S.U.; Song, H.-S.; Kim, H.-S.; Hassan, M.H.; Joh, D.-W.; Song, R.-H.; Lim, T.-H.; Hong, J.-E.; Park, S.-J.; Lee, S.-B. A Dynamic Infiltration Technique to Synthesize Nanolayered Cathodes for High Performance and Robust Solid Oxide Fuel Cells. *J. Energy Chem.* **2022**, *70*, 201–210. [[CrossRef](#)]
340. Zhao, H.; Li, W.; Wang, H.; Zhou, J.; Sun, X.; Wang, E.; Zhao, L.; Dong, B.; Wang, S. Surface Modification of  $\text{La}_{0.6}\text{Sr}_{0.4}\text{Co}_{0.2}\text{Fe}_{0.8}\text{O}_{3-\delta}$  Cathode by Infiltrating A-Site Deficient Non-Strontium  $\text{La}_{0.94}\text{Ni}_{0.6}\text{Fe}_{0.4}\text{O}_3$  Perovskite for Solid Oxide Fuel Cells. *Appl. Surf. Sci.* **2022**, *572*, 151382. [[CrossRef](#)]
341. Shi, Y.; Wen, Y.; Huang, K.; Xiong, X.; Wang, J.; Liu, M.; Ding, D.; Chen, Y.; Liu, T. Surface Enhanced Performance of  $\text{La}_{0.6}\text{Sr}_{0.4}\text{Co}_{0.2}\text{Fe}_{0.8}\text{O}_{3-\delta}$  Cathodes by Infiltration Pr-Ni-Mn-O Progress. *J. Alloys Compd.* **2022**, *902*, 163337. [[CrossRef](#)]
342. Zhou, J.; Lin, X.; Long, C.; Li, Y.; Tao, Z. Performance Optimization for Proton Conducting SOFCs by Impregnating Triple-Conducting NBSCF to Form Composite Cathode. *Mater. Lett.* **2022**, *328*, 133181. [[CrossRef](#)]
343. Jeon, S.; Seo, J.; Shin, J.W.; Lee, S.; Seo, H.G.; Lee, S.; Tsvetkov, N.; Kim, J.; An, J.; Jung, W. Metal-Oxide Nanocomposite Catalyst Simultaneously Boosts the Oxygen Reduction Reactivity and Chemical Stability of Solid Oxide Fuel Cell Cathode. *Chem. Eng. J.* **2023**, *455*, 140611. [[CrossRef](#)]
344. Huang, J.; Liu, Q.; Jiang, S.P.; Zhao, L.; Ai, N.; Wang, X.; Shao, Y.; Guan, C.; Fang, H.; Luo, Y.; et al. Promotional Role of  $\text{BaCO}_3$  on the Chromium-Tolerance of  $\text{La}_{0.6}\text{Sr}_{0.4}\text{Co}_{0.2}\text{Fe}_{0.8}\text{O}_{3-\delta}$  Cathodes of Solid Oxide Fuel Cells. *Appl. Catal. B Environ.* **2023**, *321*, 122080. [[CrossRef](#)]
345. Tarragó, D.P.; Moreno, B.; Chinarro, E.; de Fraga Malfatti, C.; de Sousa, V.C. Deposition of Nanostructured LSM Perovskite Thin Film on Dense YSZ Substrate by Airbrushed Solution Combustion (ASC) for Application in SOFC Cathodes. *Int. J. Hydrogen Energy* **2020**, *45*, 11749–11760. [[CrossRef](#)]
346. Kevin, B.; Abernathy, H.; Liu, M. Surface Enhanced Raman Spectroscopy for Investigation of SOFC Cathodes. In Proceedings of the Advances in Solid Oxide Fuel Cells V—33rd International Conference on Advanced Ceramics and Composites, Atlanta, GA, USA, 18–23 January 2009; Volume 30, pp. 63–73.
347. Yoo, Y.-S.; Namgung, Y.; Bhardwaj, A.; Song, S.-J. A Facile Combustion Synthesis Route for Performance Enhancement of  $\text{La}_{0.6}\text{Sr}_{0.4}\text{Co}_{0.2}\text{Fe}_{0.8}\text{O}_{3-\delta}$  (LSCF6428) as a Robust Cathode Material for IT-SOFC. *J. Korean Ceram. Soc* **2019**, *56*, 497–505. [[CrossRef](#)]
348. Tai, X.Y.; Zhakeyev, A.; Wang, H.; Jiao, K.; Zhang, H.; Xuan, J. Accelerating Fuel Cell Development with Additive Manufacturing Technologies: State of the Art, Opportunities and Challenges. *Fuel Cells* **2019**, *19*, 636–650. [[CrossRef](#)]
349. Minary-Jolandan, M. Formidable Challenges in Additive Manufacturing of Solid Oxide Electrolyzers (SOECs) and Solid Oxide Fuel Cells (SOFCs) for Electrolytic Hydrogen Economy toward Global Decarbonization. *Ceramics* **2022**, *5*, 761–779. [[CrossRef](#)]
350. Zouridi, L.; Garagounis, I.; Vourros, A.; Marnellos, G.E.; Binas, V. Advances in Inkjet-Printed Solid Oxide Fuel Cells. *Adv. Mater. Technol.* **2022**, *7*, 2101491. [[CrossRef](#)]
351. Kawale, S.S.; Jang, I.; Farandos, N.M.; Kelsall, G.H. Inkjet 3D-Printing of Functional Layers of Solid Oxide Electrochemical Reactors: A Review. *React. Chem. Eng.* **2022**, *7*, 1692–1712. [[CrossRef](#)]
352. Jang, I.; Alexander, J.C.; Farandos, N.M.; Kelsall, G.H. Predicting Optimal Geometries of 3D-Printed Solid Oxide Electrochemical Reactors. *Electrochim. Acta* **2022**, *427*, 140902. [[CrossRef](#)]
353. Rath, M.K.; Kossenko, A.; Danchuk, V.; Shatalov, M.; Rahumi, O.; Borodianskiy, K.; Zinigrad, M.; Sahoo, T.; Mishra, S. Development of Highly Efficient and Durable Large-Area Solid Oxide Fuel Cell by a Direct-Ink-Writing Three-Dimensional Printer. *J. Power Sources* **2022**, *552*, 232225. [[CrossRef](#)]
354. Fashalameh, K.M.; Sadeghian, Z.; Ebrahimi, R. A High-Performance Planar Anode-Supported Solid Oxide Fuel Cell with Hierarchical Porous Structure through Slurry-Based Three-Dimensional Printing. *J. Alloys Compd.* **2022**, *916*, 165406. [[CrossRef](#)]
355. Jang, I.; Kelsall, G.H. Fabrication of 3D NiO-YSZ Structures for Enhanced Performance of Solid Oxide Fuel Cells and Electrolysers. *Electrochem. Commun.* **2022**, *137*, 107260. [[CrossRef](#)]
356. Farandos, N.M.; Jang, I.; Alexander, J.C.; Kelsall, G.H. 3-D Inkjet Printed Solid Oxide Electrochemical Reactors III. Cylindrical Pillared Electrode Microstructures. *Electrochim. Acta* **2022**, *426*, 140834. [[CrossRef](#)]
357. Anelli, S.; Rosa, M.; Baiutti, F.; Torrell, M.; Esposito, V.; Tarancón, A. Hybrid-3D Printing of Symmetric Solid Oxide Cells by Inkjet Printing and Robocasting. *Addit. Manuf.* **2022**, *51*, 102636. [[CrossRef](#)]
358. Tian, J.; Dou, Y.; Nian, Q.; Milcarek, R.J. Solid Oxide Fuel Cells with 3D Inkjet Printing Modified LSM–YSZ Interface. *ECS Trans.* **2022**, *109*, 51–61. [[CrossRef](#)]
359. Lira, M.; Kostretsova, N.; Bernadet, L.; Morata, A.; Torrell, M.; Tarancón, A. Additive Manufacturing of Large Area SOC with Advanced Features. *ECS Trans.* **2021**, *103*, 149–157. [[CrossRef](#)]
360. Qu, P.; Xiong, D.; Zhu, Z.; Gong, Z.; Li, Y.; Li, Y.; Fan, L.; Liu, Z.; Wang, P.; Liu, C.; et al. Inkjet Printing Additively Manufactured Multilayer SOFCs Using High Quality Ceramic Inks for Performance Enhancement. *Addit. Manuf.* **2021**, *48*, 102394. [[CrossRef](#)]
361. Lee, J.; Byeon, J.; Lee, C. Fabrication of Thickness-Controllable Double Layer Electrolyte Using Roll-to-Roll Additive Manufacturing System. *Int. J. Precis. Eng. Manuf. Green Technol.* **2020**, *7*, 635–642. [[CrossRef](#)]
362. Østergård, M.J.L.; Clausen, C.; Bagger, C.; Mogensen, M. Manganite-Zirconia Composite Cathodes for SOFC: Influence of Structure and Composition. *Electrochim. Acta* **1995**, *40*, 1971–1981. [[CrossRef](#)]

363. Li, N. The Interaction of LSM–YSZ Composite and Improvement of the Solid Oxide Cell Durability by Mn-Modified YSZ. Ph.D. Thesis, University of Connecticut, Storrs, CT, USA, 2014.
364. Natoli, A.; Arias-Serrano, B.I.; Rodríguez-Castellón, E.; Żurawska, A.; Frade, J.R.; Yaremchenko, A.A. Mixed Ionic-Electronic Conductivity, Redox Behavior and Thermochemical Expansion of Mn-Substituted 5YSZ as an Interlayer Material for Reversible Solid Oxide Cells. *Materials* **2021**, *14*, 641. [[CrossRef](#)]
365. Niu, B.; Jin, F.; Feng, T.; Zhang, L.; Zhang, Y.; He, T. A-Site Deficient  $(\text{La}_{0.6}\text{Sr}_{0.4})_{1-x}\text{Co}_{0.2}\text{Fe}_{0.6}\text{Nb}_{0.2}\text{O}_{3-\delta}$  Symmetrical Electrode Materials for Solid Oxide Fuel Cells. *Electrochim. Acta* **2018**, *270*, 174–182. [[CrossRef](#)]
366. Bucher, E.; Sitte, W.; Klauser, F.; Bertel, E. Oxygen Exchange Kinetics of  $\text{La}_{0.6}\text{Sr}_{0.4}\text{Co}_{0.2}\text{Fe}_{0.8}\text{O}_{3-\delta}$  at 600 °C in Dry and Humid Atmospheres. *Solid State Ion.* **2011**, *191*, 61–67. [[CrossRef](#)]
367. Kostogloudis, G.C.; Ftikos, C. Properties of A-Site-Deficient  $\text{La}_{0.6}\text{Sr}_{0.4}\text{Co}_{0.2}\text{Fe}_{0.8}\text{O}_{3-\delta}$ -Based Perovskite Oxides. *Solid State Ion.* **1999**, *126*, 143–151. [[CrossRef](#)]
368. Yang, Y.; Bao, H.; Ni, H.; Ou, X.; Wang, S.; Lin, B.; Feng, P.; Ling, Y. A Novel Facile Strategy to Suppress Sr Segregation for High-Entropy Stabilized  $\text{La}_{0.8}\text{Sr}_{0.2}\text{MnO}_{3-\delta}$  Cathode. *J. Power Sources* **2021**, *482*, 228959. [[CrossRef](#)]
369. Shi, Y.; Ni, N.; Ding, Q.; Zhao, X. Tailoring High-Temperature Stability and Electrical Conductivity of High Entropy Lanthanum Manganite for Solid Oxide Fuel Cell Cathodes. *J. Mater. Chem. A* **2022**, *10*, 2256–2270. [[CrossRef](#)]
370. Dąbrowa, J.; Olszewska, A.; Falkenstein, A.; Schwab, C.; Szymczak, M.; Zajusz, M.; Możdziej, M.; Mięka, A.; Zielińska, K.; Berent, K.; et al. An Innovative Approach to Design SOFC Air Electrode Materials: High Entropy  $\text{La}_{1-x}\text{Sr}_x(\text{Co,Cr,Fe,Mn,Ni})\text{O}_{3-\delta}$  ( $x = 0, 0.1, 0.2, 0.3$ ) Perovskites Synthesized by the Sol–Gel Method. *J. Mater. Chem. A* **2020**, *8*, 24455–24468. [[CrossRef](#)]
371. Xu, H.; Dang, L.; Yan, J.; Wan, F.; Gong, W. A New  $(\text{La}_{0.2}\text{Nd}_{0.2}\text{Gd}_{0.2}\text{Sr}_{0.2}\text{Ba}_{0.2})\text{Co}_{0.2}\text{Fe}_{0.8}\text{O}_{3-\delta}$  High-Entropy Oxide Cathode for Intermediate Temperature Solid Oxide Fuel Cell. *Solid State Ion.* **2023**, *397*, 116233. [[CrossRef](#)]
372. Khan, M.S.; Xu, X.; Zhao, J.; Knibbe, R.; Zhu, Z. A Porous Yttria-Stabilized Zirconia Layer to Eliminate the Delamination of Air Electrode in Solid Oxide Electrolysis Cells. *J. Power Sources* **2017**, *359*, 104–110. [[CrossRef](#)]
373. Wang, S. Promoting Effect of YSZ on the Electrochemical Performance of YSZ+LSM Composite Electrodes. *Solid State Ion.* **1998**, *113–115*, 291–303. [[CrossRef](#)]
374. Rehman, S.U.; Song, R.-H.; Lee, J.-W.; Lim, T.-H.; Park, S.-J.; Lee, S.-B. Effect of GDC Addition Method on the Properties of LSM–YSZ Composite Cathode Support for Solid Oxide Fuel Cells. *Ceram. Int.* **2016**, *42*, 11772–11779. [[CrossRef](#)]
375. Nielsen, J.; Hjelm, J. Impedance of SOFC Electrodes: A Review and a Comprehensive Case Study on the Impedance of LSM:YSZ Cathodes. *Electrochim. Acta* **2014**, *115*, 31–45. [[CrossRef](#)]
376. Agbede, O.O.; Hellgardt, K.; Kelsall, G.H. Electrical Conductivities and Microstructures of LSM, LSM–YSZ and LSM–YSZ/LSM Cathodes Fabricated on YSZ Electrolyte Hollow Fibres by Dip-Coating. *Mater. Today Chem.* **2020**, *16*, 100252. [[CrossRef](#)]
377. Chen, K.; Ai, N.; Jiang, S.P. Reasons for the High Stability of Nano-Structured  $(\text{La,Sr})\text{MnO}_3$  Infiltrated  $\text{Y}_2\text{O}_3\text{–ZrO}_2$  Composite Oxygen Electrodes of Solid Oxide Electrolysis Cells. *Electrochem. Commun.* **2012**, *19*, 119–122. [[CrossRef](#)]
378. Wang, J.X.; Sun, J.L.; He, C.R.; Wang, Q.; Wang, W.G. Mass Synthesis of High Performance  $(\text{La}_{0.75}\text{Sr}_{0.25})_{0.95}\text{MnO}_{3\pm\delta}$  Nano-Powder Prepared via a Low-Carbon Chemical Solution Method. *J. Power Sources* **2014**, *253*, 424–430. [[CrossRef](#)]
379. Sun, K.; Piao, J.; Zhang, N.; Chen, X.; Xu, S.; Zhou, D. Fabrication and Performance of  $\text{La}_{0.8}\text{Sr}_{0.2}\text{MnO}_3/\text{YSZ}$  Graded Composite Cathodes for SOFC. *Rare Met.* **2008**, *27*, 278–281. [[CrossRef](#)]
380. Jørgensen, M. Effect of Sintering Temperature on Microstructure and Performance of LSM–YSZ Composite Cathodes. *Solid State Ion.* **2001**, *139*, 1–11. [[CrossRef](#)]
381. Yeh, C.-Y.; Lin, T.-N.; Kuo, H.-Y.; Liao, M.-W.; Chen, Y.-M.; Kao, W.-X.; Lee, R.-Y.; Lee, S.-W. Microstructure Modification in the Electrodes to Enhance Performance of the Anode-Supported Solid Oxide Fuel Cell. In *Ceramic Engineering and Science Proceedings*; Salem, J., Koch, D., Mechnich, P., Kusnezoff, M., Bansal, N., LaSalvia, J., Balaya, P., Fu, Z., Ohji, T., Eds.; John Wiley & Sons, Inc.: Hoboken, NJ, USA, 2019; pp. 113–121. ISBN 978-1-119-54334-3.
382. Taylor, T.H.; Muhoza, S.P.; Gross, M.D. Lowering the Impedance of Lanthanum Strontium Manganite-Based Electrodes with Lanthanum Oxychloride and Lanthanum Scavenging Chloride Salts. *J. Electrochem. Soc.* **2021**, *168*, 114508. [[CrossRef](#)]
383. Lee, E.; Jeong, H.; Shin, T.H.; Myung, J.-H. Determination of the Rate-Determining Step of the Oxygen Reduction Reaction of  $\text{La}_{0.8}\text{Sr}_{0.2}\text{MnO}_3(\text{LSM})\text{-}8\text{mol}\%$  Yttria-Stabilized Zirconia(YSZ): Composition and Microstructure. *Ceram. Int.* **2021**, *47*, 1792–1797. [[CrossRef](#)]
384. Burmistrov, I.; Agarkov, D.; Bredikhin, S.; Nepochatov, Y.; Tiunova, O.; Zadorozhnaya, O. Multilayered Electrolyte-Supported SOFC Based on NEVZ-Ceramics Membrane. *ECS Trans.* **2013**, *57*, 917–923. [[CrossRef](#)]
385. Khan, M.S.; Xu, X.; Knibbe, R.; Zhu, Z. Porous Scandia-Stabilized Zirconia Layer for Enhanced Performance of Reversible Solid Oxide Cells. *ACS Appl. Mater. Interfaces* **2018**, *10*, 25295–25302. [[CrossRef](#)]
386. Nagasawa, T.; Hanamura, K. Particle-Scaled Visualization of Active Sites in LSM/ScSZ Composite Cathode of SOFC through Oxygen Isotope Labeling. *ECS Trans.* **2017**, *78*, 855–859. [[CrossRef](#)]
387. Yaroslavtsev, I.Y.; Bronin, D.I.; Vdovin, G.K.; Isupova, L.A. Oxide Cathodes for Electrochemical Devices Made with the Use of a Nanostructured Composition Material. *Russ. J. Electrochem.* **2012**, *48*, 981–985. [[CrossRef](#)]
388. Sadykov, V.; Alikina, G.; Lukashevich, A.; Muzykantov, V.; Usoltsev, V.; Boronin, A.; Koscheev, S.; Krieger, T.; Ishchenko, A.; Smirnova, A.; et al. Design and Characterization of LSM/ScCeSZ Nanocomposite as Mixed Ionic–Electronic Conducting Material for Functionally Graded Cathodes of Solid Oxide Fuel Cells. *Solid State Ion.* **2011**, *192*, 540–546. [[CrossRef](#)]

389. Osinkin, D.A.; Bogdanovich, N.M.; Beresnev, S.M.; Pikalova, E.Y.; Bronin, D.I.; Zaikov, Y.P. Reversible Solid Oxide Fuel Cell for Power Accumulation and Generation. *Russ. J. Electrochem.* **2018**, *54*, 644–649. [\[CrossRef\]](#)
390. Jeong, H.; Sharma, B.; Jo, S.; Kim, Y.H.; Myung, J. Electrochemical Characteristics of  $\text{La}_{0.8}\text{Sr}_{0.2}\text{MnO}_3$  (LSM)–Scandia-Stabilized Zirconia (ScSZ) Composite Cathode. *J. Korean Ceram. Soc.* **2022**, *59*, 473–479. [\[CrossRef\]](#)
391. Sanna, C.; Squizzato, E.; Costamagna, P.; Holtappels, P.; Glisenti, A. Electrochemical Study of Symmetrical Intermediate Temperature—Solid Oxide Fuel Cells Based on  $\text{La}_{0.6}\text{Sr}_{0.4}\text{MnO}/\text{Ce}_{0.9}\text{Gd}_{0.1}\text{O}_{1.95}$  for Operation in Direct Methane/Air. *Electrochim. Acta* **2022**, *409*, 139939. [\[CrossRef\]](#)
392. Wang, Z.; Wang, X.; Xu, Z.; Deng, H.; Dong, W.; Wang, B.; Feng, C.; Liu, X.; Wang, H. Semiconductor-Ionic Nanocomposite  $\text{La}_{0.1}\text{Sr}_{0.9}\text{MnO}_{3-\delta}-\text{Ce}_{0.8}\text{Sm}_{0.2}\text{O}_{2-\delta}$  Functional Layer for High Performance Low Temperature SOFC. *Materials* **2018**, *11*, 1549. [\[CrossRef\]](#)
393. Baiutti, F.; Chiabrera, F.; Acosta, M.; Diercks, D.; Parfitt, D.; Santiso, J.; Wang, X.; Cavallaro, A.; Morata, A.; Wang, H.; et al. A High-Entropy Manganite in an Ordered Nanocomposite for Long-Term Application in Solid Oxide Cells. *Nat. Commun.* **2021**, *12*, 2660. [\[CrossRef\]](#)
394. Pajot, M.; Duffort, V.; Capoen, E.; Mamede, A.-S.; Vannier, R.-N. Influence of the Strontium Content on the Performance of  $\text{La}_{1-x}\text{Sr}_x\text{MnO}_3/\text{Bi}_{1.5}\text{Er}_{0.5}\text{O}_3$  Composite Electrodes for Low Temperature Solid Oxide Fuel Cells. *J. Power Sources* **2020**, *450*, 227649. [\[CrossRef\]](#)
395. Zhang, C.; Huang, K. A New Composite Cathode for Intermediate Temperature Solid Oxide Fuel Cells with Zirconia-Based Electrolytes. *J. Power Sources* **2017**, *342*, 419–426. [\[CrossRef\]](#)
396. Timurkutluk, B.; Altan, T.; Toros, S.; Genc, O.; Celik, S.; Korkmaz, H.G. Engineering Solid Oxide Fuel Cell Electrode Microstructure by a Micro-Modeling Tool Based on Estimation of TPB Length. *Int. J. Hydrogen Energy* **2021**, *46*, 13298–13317. [\[CrossRef\]](#)
397. Kim, S.J.; Dayaghi, A.M.; Kim, K.J.; Choi, G.M.  $\text{Er}_{0.4}\text{Bi}_{1.6}\text{O}_{3-\delta}-\text{La}_{0.8}\text{Sr}_{0.2}\text{MnO}_{3-\delta}$  Nano-Composite as a Low-Temperature Firing Cathode of Solid Oxide Fuel Cell. *J. Power Sources* **2017**, *344*, 218–222. [\[CrossRef\]](#)
398. Lee, K.T.; Jung, D.W.; Yoon, H.S.; Camaratta, M.; Sexson, N.; Wachsmann, E.D. High Performance LSM-ESB Cathode on ESB Electrolyte for Low to Intermediate Temperature Solid Oxide Fuel Cells. *ECS Trans.* **2011**, *35*, 1861–1869. [\[CrossRef\]](#)
399. Yun, B.-H.; Kim, K.J.; Joh, D.W.; Chae, M.S.; Lee, J.J.; Kim, D.; Kang, S.; Choi, D.; Hong, S.-T.; Lee, K.T. Highly Active and Durable Double-Doped Bismuth Oxide-Based Oxygen Electrodes for Reversible Solid Oxide Cells at Reduced Temperatures. *J. Mater. Chem. A* **2019**, *7*, 20558–20566. [\[CrossRef\]](#)
400. Dotelli, G.; Mari, C.; Ruffo, R.; Pelosato, R.; Sora, I. Electrical Behaviour of LSGM–LSM Composite Cathode Materials. *Solid State Ion.* **2006**, *177*, 1991–1996. [\[CrossRef\]](#)
401. Pelosato, R.; Sora, I.N.; Dotelli, G.; Ruffo, R.; Mari, C.M. Characterization of  $(1-x)\text{La}_{0.83}\text{Sr}_{0.17}\text{Ga}_{0.83}\text{Mg}_{0.17}\text{O}_{2.83}-x\text{La}_{0.8}\text{Sr}_{0.2}\text{MnO}_3$  ( $0 \leq x \leq 1$ ) Composite Cathodes. *J. Eur. Ceram. Soc.* **2005**, *25*, 2587–2591. [\[CrossRef\]](#)
402. Shahrokhi, S.; Babaei, A.; Zamani, C. Reversible Operation of  $\text{La}_{0.8}\text{Sr}_{0.2}\text{MnO}_3$  Oxygen Electrode Infiltrated with Ruddlesden-Popper and Perovskite Lanthanum Nickel Cobaltite. *Int. J. Hydrogen Energy* **2018**, *43*, 23091–23100. [\[CrossRef\]](#)
403. Liu, Z.; Liu, M.; Yang, L.; Liu, M. LSM-Infiltrated LSCF Cathodes for Solid Oxide Fuel Cells. *J. Energy Chem.* **2013**, *22*, 555–559. [\[CrossRef\]](#)
404. Ai, N.; Chen, K.; Jiang, S.P. A  $\text{La}_{0.8}\text{Sr}_{0.2}\text{MnO}_3/\text{La}_{0.6}\text{Sr}_{0.4}\text{Co}_{0.2}\text{Fe}_{0.8}\text{O}_{3-\delta}$  Core-Shell Structured Cathode by a Rapid Sintering Process for Solid Oxide Fuel Cells. *Int. J. Hydrogen Energy* **2017**, *42*, 7246–7251. [\[CrossRef\]](#)
405. Seyed-Vakili, S.V.; Babaei, A.; Ataie, M.; Heshmati-Manesh, S.; Abdizadeh, H. Enhanced Performance of  $\text{La}_{0.8}\text{Sr}_{0.2}\text{MnO}_3$  Cathode for Solid Oxide Fuel Cells by Co-Infiltration of Metal and Ceramic Precursors. *J. Alloys Compd.* **2018**, *737*, 433–441. [\[CrossRef\]](#)
406. Khellaf, N.; Kahoul, A.; Naamoune, F.; Cheriti, M. Impact of the Synthesis Method on Electrochemical Performance of  $\text{La}_{0.5}\text{Sr}_{0.5}\text{MnO}_3$  Perovskite Oxide as a Cathode Material in Alkaline Fuel Cells. *Russ. J. Electrochem.* **2022**, *58*, 10–20. [\[CrossRef\]](#)
407. Leng, Y.; Chan, S.; Liu, Q. Development of LSCF–GDC Composite Cathodes for Low-Temperature Solid Oxide Fuel Cells with Thin Film GDC Electrolyte. *Int. J. Hydrogen Energy* **2008**, *33*, 3808–3817. [\[CrossRef\]](#)
408. Liu, Q.L.; Khor, K.A.; Chan, S.H. Optimization of LSCF–GDC Composite Cathodes for Thin Film GDC Electrolyte Solid Oxide Fuel Cells. In Proceedings of the Third International Conference on Materials Processing for Properties and Performance (MP3), Singapore, 24–26 November 2004; Khor, K.A., Ramanujan, R.V., Ooi, C.P., Zhao, J., Eds.; Institute of Materials (East Asia): Singapore, 2004; pp. 657–666.
409. Dusastre, V.; Kilner, J.A. Optimisation of Composite Cathodes for Intermediate Temperature SOFC Applications. *Solid State Ion.* **1999**, *126*, 163–174. [\[CrossRef\]](#)
410. Perry Murray, E. Electrochemical Performance of  $(\text{La,Sr})(\text{Co,Fe})\text{O}_3-(\text{Ce,Gd})\text{O}_3$  Composite Cathodes. *Solid State Ion.* **2002**, *148*, 27–34. [\[CrossRef\]](#)
411. Chen, J.; Liang, F.; Yan, D.; Pu, J.; Chi, B.; Jiang, S.P.; Jian, L. Performance of Large-Scale Anode-Supported Solid Oxide Fuel Cells with Impregnated  $\text{La}_{0.6}\text{Sr}_{0.4}\text{Co}_{0.2}\text{Fe}_{0.8}\text{O}_{3-\delta}+\text{Y}_2\text{O}_3$  Stabilized  $\text{ZrO}_2$  Composite Cathodes. *J. Power Sources* **2010**, *195*, 5201–5205. [\[CrossRef\]](#)
412. Han, M.F.; Liu, Z.; Qian, J. Fabrication and Characterization of  $\text{La}_{0.6}\text{Sr}_{0.4}\text{Co}_{0.2}\text{Fe}_{0.8}\text{O}_{3-\delta}-\text{Yttria}$  Stabilized Zirconia Composites Cathode Prepared by Infiltration Method. *ECS Trans.* **2011**, *35*, 2295–2303. [\[CrossRef\]](#)
413. Ko, H.J.; Myung, J.; Lee, J.-H.; Hyun, S.-H.; Chung, J.S. Synthesis and Evaluation of  $(\text{La}_{0.6}\text{Sr}_{0.4})(\text{Co}_{0.2}\text{Fe}_{0.8})\text{O}_3$  (LSCF)– $\text{Y}_{0.08}\text{Zr}_{0.92}\text{O}_{1.96}$  (YSZ)– $\text{Gd}_{0.1}\text{Ce}_{0.9}\text{O}_{2-\delta}$  (GDC) Dual Composite SOFC Cathodes for High Performance and Durability. *Int. J. Hydrogen Energy* **2012**, *37*, 17209–17216. [\[CrossRef\]](#)

414. Gong, J.; Shi, H.; Yu, Y.; Yue, Z.; Wang, Y.; Tan, W. Restrictions of Nitric Oxide Electrocatalytic Decomposition over Perovskite Cathode in Presence of Oxygen: Oxygen Surface Exchange and Diffusion. *J. Colloid Interface Sci.* **2022**, *628*, 95–105. [[CrossRef](#)]
415. Xi, X.; Kondo, A.; Kozawa, T.; Naito, M. LSCF–GDC Composite Particles for Solid Oxide Fuel Cells Cathodes Prepared by Facile Mechanical Method. *Adv. Powder Technol.* **2016**, *27*, 646–651. [[CrossRef](#)]
416. Gao, C.; Liu, Y.; Xi, K.; Jiao, S.; Tomov, R.I.; Kumar, R.V. Improve the Catalytic Property of  $\text{La}_{0.6}\text{Sr}_{0.4}\text{Co}_{0.2}\text{Fe}_{0.8}\text{O}_{3-\delta}$ / $\text{Ce}_{0.9}\text{Gd}_{0.1}\text{O}_2$  (LSCF/CGO) Cathodes with CuO Nanoparticles Infiltration. *Electrochim. Acta* **2017**, *246*, 148–155. [[CrossRef](#)]
417. Zhao, E.; Liu, X.; Liu, L.; Huo, H.; Xiong, Y. Effect of  $\text{La}_{0.8}\text{Sr}_{0.2}\text{Co}_{0.2}\text{Fe}_{0.8}\text{O}_{3-\delta}$  Morphology on the Performance of Composite Cathodes. *Progr. Nat. Sci. Mater. Inter.* **2014**, *24*, 24–30. [[CrossRef](#)]
418. Zhao, L.; Amarasinghe, S.; Jiang, S.P. Enhanced Chromium Tolerance of  $\text{La}_{0.6}\text{Sr}_{0.4}\text{Co}_{0.2}\text{Fe}_{0.8}\text{O}_{3-\delta}$  Electrode of Solid Oxide Fuel Cells by  $\text{Gd}_{0.1}\text{Ce}_{0.9}\text{O}_{1.95}$  Impregnation. *Electrochem. Commun.* **2013**, *37*, 84–87. [[CrossRef](#)]
419. Li, N.; Verma, A.; Singh, P.; Kim, J.-H. Characterization of  $\text{La}_{0.58}\text{Sr}_{0.4}\text{Co}_{0.2}\text{Fe}_{0.8}\text{O}_{3-\delta}$ - $\text{Ce}_{0.8}\text{Gd}_{0.2}\text{O}_2$  Composite Cathode for Intermediate Temperature Solid Oxide Fuel Cells. *Ceram. Int.* **2013**, *39*, 529–538. [[CrossRef](#)]
420. Zhang, N.; Li, J.; Ni, D.; Sun, K. Preparation of Honeycomb Porous  $\text{La}_{0.6}\text{Sr}_{0.4}\text{Co}_{0.2}\text{Fe}_{0.8}\text{O}_{3-\delta}$ - $\text{Gd}_{0.2}\text{Ce}_{0.8}\text{O}_{2-\delta}$  Composite Cathodes by Breath Figures Method for Solid Oxide Fuel Cells. *Appl. Surf. Sci.* **2011**, *258*, 50–57. [[CrossRef](#)]
421. Zhi, M.; Lee, S.; Miller, N.; Menzler, N.H.; Wu, N. An Intermediate-Temperature Solid Oxide Fuel Cell with Electrospun Nanofiber Cathode. *Energy Environ. Sci.* **2012**, *5*, 7066. [[CrossRef](#)]
422. Shen, F.; Lu, K.  $\text{La}_{0.6}\text{Sr}_{0.4}\text{Co}_{0.2}\text{Fe}_{0.8}\text{O}_3$  Cathodes Incorporated with  $\text{Sm}_{0.2}\text{Ce}_{0.8}\text{O}_2$  by Three Different Methods for Solid Oxide Fuel Cells. *J. Power Sources* **2015**, *296*, 318–326. [[CrossRef](#)]
423. Hu, B.; Wang, Y.; Xia, C. Oxygen Incorporation at the Three-Phase Boundary of LSCF–SDC Composite. *J. Power Sources* **2014**, *269*, 180–188. [[CrossRef](#)]
424. Lee, S.; Song, H.S.; Hyun, S.H.; Kim, J.; Moon, J. LSCF–SDC Core–Shell High-Performance Durable Composite Cathode. *J. Power Sources* **2010**, *195*, 118–123. [[CrossRef](#)]
425. Nie, L.; Liu, M.; Zhang, Y.; Liu, M.  $\text{La}_{0.6}\text{Sr}_{0.4}\text{Co}_{0.2}\text{Fe}_{0.8}\text{O}_{3-\delta}$  Cathodes Infiltrated with Samarium-Doped Cerium Oxide for Solid Oxide Fuel Cells. *J. Power Sources* **2010**, *195*, 4704–4708. [[CrossRef](#)]
426. Wang, S. Performance of a  $\text{La}_{0.6}\text{Sr}_{0.4}\text{Co}_{0.2}\text{Fe}_{0.8}\text{O}_3$ - $\text{Ce}_{0.8}\text{Gd}_{0.2}\text{O}_{1.9}$ -Ag Cathode for Ceria Electrolyte SOFCs. *Solid State Ion.* **2002**, *146*, 203–210. [[CrossRef](#)]
427. Liu, W.; Zhao, Z.; Tu, B.; Cui, D.; Ou, D.; Cheng, M. Enhanced Performance and Stability of Interlayer-Free  $\text{La}_{0.6}\text{Sr}_{0.4}\text{Co}_{0.2}\text{Fe}_{0.8}\text{O}_{3-\delta}$ - $\text{Ce}_{0.8}\text{Zr}_{0.2}\text{O}_{2-\delta}$  Cathode for Solid Oxide Fuel Cells. *Int. J. Hydrogen Energy* **2015**, *40*, 4861–4867. [[CrossRef](#)]
428. Guo, W.; Liu, J.; Jin, C.; Gao, H.; Zhang, Y. Electrochemical Evaluation of  $\text{La}_{0.6}\text{Sr}_{0.4}\text{Co}_{0.2}\text{Fe}_{0.8}\text{O}_{3-\delta}$ - $\text{La}_{0.9}\text{Sr}_{0.1}\text{Ga}_{0.8}\text{Mg}_{0.2}\text{O}_{3-\delta}$  Composite Cathodes for  $\text{La}_{0.9}\text{Sr}_{0.1}\text{Ga}_{0.8}\text{Mg}_{0.2}\text{O}_{3-\delta}$  Electrolyte SOFCs. *J. Alloys Compd.* **2009**, *473*, 43–47. [[CrossRef](#)]
429. Lin, Y.; Barnett, S.  $\text{La}_{0.9}\text{Sr}_{0.1}\text{Ga}_{0.8}\text{Mg}_{0.2}\text{O}_{3-\delta}$ - $\text{La}_{0.6}\text{Sr}_{0.4}\text{Co}_{0.2}\text{Fe}_{0.8}\text{O}_{3-\delta}$  Composite Cathodes for Intermediate-Temperature Solid Oxide Fuel Cells. *Solid State Ion.* **2008**, *179*, 420–427. [[CrossRef](#)]
430. Giuliano, A.; Carpanese, M.P.; Panizza, M.; Cerisola, G.; Clematis, D.; Barbucci, A. Characterisation of  $\text{La}_{0.6}\text{Sr}_{0.4}\text{Co}_{0.2}\text{Fe}_{0.8}\text{O}_{3-\delta}$ - $\text{Ba}_{0.5}\text{Sr}_{0.5}\text{Co}_{0.8}\text{Fe}_{0.2}\text{O}_{3-\delta}$  Composite as Cathode for Solid Oxide Fuel Cells. *Electrochim. Acta* **2017**, *240*, 258–266. [[CrossRef](#)]
431. Świerczek, K. Electrolyte-Supported IT-SOFC with LSCF–SCFN Composite Cathode. *Solid State Ion.* **2011**, *192*, 486–490. [[CrossRef](#)]
432. Burye, T.E.; Nicholas, J.D. Improving  $\text{La}_{0.6}\text{Sr}_{0.4}\text{Co}_{0.2}\text{Fe}_{0.8}\text{O}_{3-\delta}$  Infiltrated Solid Oxide Fuel Cell Cathode Performance through Precursor Solution Desiccation. *J. Power Sources* **2015**, *276*, 54–61. [[CrossRef](#)]
433. Wang, L.; Wang, P.; Geng, C.; Cao, H.; Xu, C.; Cheng, J.; Hong, T. A Novel Core-Shell LSCF Perovskite Structured Electrocatalyst with Local Hetero-Interface for Solid Oxide Fuel Cells. *Int. J. Hydrogen Energy* **2020**, *45*, 11824–11833. [[CrossRef](#)]
434. Fasquelle, D.; Chi, Z.; Belakry, S. Impregnation of Gadolinium-Doped Ceria Backbone Electrodes Modified by Addition of Pore-Formers for SOFC Application. *J. Solid State Electrochem.* **2023**, *27*, 695–703. [[CrossRef](#)]
435. Wei, M.; Chen, H.; Zhao, X.; Liu, Y.; Chen, X.; Li, W.; Kang, K.; Wang, C. High Performance  $\text{La}_2\text{NiO}_{4+\delta}$  Impregnated  $\text{La}_{0.6}\text{Sr}_{0.4}\text{Co}_{0.2}\text{Fe}_{0.8}\text{O}_{3-\delta}$  Cathodes for Solid Oxide Fuel Cells. *Solid State Ion.* **2022**, *387*, 116065. [[CrossRef](#)]
436. Liu, Y.; Pan, Z.; Zhao, X.; Zhong, S.; Chen, X.; Wang, C. Performance of  $\text{PrBaCo}_2\text{O}_{5+\delta}$  Impregnated  $\text{La}_{0.6}\text{Sr}_{0.4}\text{Co}_{0.2}\text{Fe}_{0.8}\text{O}_{3-\delta}$  Composites as Potential Cathode Materials for Solid Oxide Fuel Cells. *J. Alloys Compd.* **2021**, *886*, 161155. [[CrossRef](#)]
437. Zheng, Z.; Jing, J.; Yu, H.; Yang, Z.; Jin, C.; Chen, F.; Peng, S. Boosting and Robust Multifunction Cathode Layer for Solid Oxide Fuel Cells. *ACS Sustain. Chem. Eng.* **2022**, *10*, 6817–6825. [[CrossRef](#)]
438. Wang, J.; Yang, T.; Wen, Y.; Zhang, Y.; Sun, C.; Huang, K. Performance and Stability of  $\text{SrCo}_{0.9}\text{Nb}_{0.1}\text{O}_{3-\delta}$ - $(\text{La}_{0.60}\text{Sr}_{0.40})_{0.95}(\text{Co}_{0.20}\text{Fe}_{0.80})\text{O}_{3-\delta}$  Bilayer Cathode for Intermediate-Temperature Solid Oxide Fuel Cells. *J. Power Sources* **2019**, *414*, 24–30. [[CrossRef](#)]
439. Chen, J.; Liang, F.; Chi, B.; Pu, J.; Jiang, S.P.; Jian, L. Palladium and Ceria Infiltrated  $\text{La}_{0.8}\text{Sr}_{0.2}\text{Co}_{0.5}\text{Fe}_{0.5}\text{O}_{3-\delta}$  Cathodes of Solid Oxide Fuel Cells. *J. Power Sources* **2009**, *194*, 275–280. [[CrossRef](#)]
440. Ji, Y.; Kilner, J.; Carolan, M. Electrical Properties and Oxygen Diffusion in Ytria-Stabilised Zirconia (YSZ)- $\text{La}_{0.8}\text{Sr}_{0.2}\text{MnO}_{3+\delta}$  (LSM) Composites. *Solid State Ion.* **2005**, *176*, 937–943. [[CrossRef](#)]
441. Agbede, O.O.; Kelsall, G.H.; Hellgardt, K. A Solid Oxide Fuel Cell with Molten Tin Anode for Electricity Generation and Methane Reforming. *J. Power Sources* **2020**, *474*, 228577. [[CrossRef](#)]
442. Harboe, S.; Sohn, Y.J.; Guillon, O.; Menzler, N.H. Investigation of LSM–8YSZ Cathode within an All Ceramic SOFC. Part I: Chemical Interactions. *J. Eur. Ceram. Soc.* **2020**, *40*, 3608–3617. [[CrossRef](#)]

443. Matte, E.; Holzlechner, G.; Epple, L.; Stolten, D.; Lupetin, P. Impact of Silicate Substrate and Cosintering on Cathode Performance in an Inert Substrate-Supported Solid Oxide Fuel Cell. *J. Power Sources* **2019**, *413*, 334–343. [[CrossRef](#)]
444. Wu, X.; Tian, Y.; Zhou, X.; Kong, X.; Zhang, J.; Zuo, W.; Ye, X. High Performance Yttria-Stabilized Zirconia Based Intermediate Temperature Solid Oxide Fuel Cells with Double Nano Layer Composite Cathode. *Int. J. Hydrogen Energy* **2017**, *42*, 1093–1102. [[CrossRef](#)]
445. Celikbilek, O.; Dessemond, L.; Djurado, E. State-of-the-Art  $\text{La}_{0.6}\text{Sr}_{0.4}\text{Co}_{0.2}\text{Fe}_{0.8}\text{O}_{3-\delta}$  Cathode for SOFC: Microstructural and Electrochemical Properties. *ECS Trans.* **2017**, *78*, 747–758. [[CrossRef](#)]
446. Sohal, M.S.; O'Brien, J.E.; Stoots, C.M.; Sharma, V.I.; Yildiz, B.; Virkar, A. Degradation Issues in Solid Oxide Cells during High Temperature Electrolysis. In Proceedings of the ASME 2010 8th International Fuel Cell Science, Engineering and Technology Conference, Brooklyn, New York, NY, USA, 1 January 2010; ASMEDC: Houston, TX, USA, 2010; Volume 1, pp. 377–387. [[CrossRef](#)]
447. Pan, Z.; Liu, Q.; Yan, Z.; Jiao, Z.; Bi, L.; Chan, S.H.; Zhong, Z. On the Delamination of Air Electrodes of Solid Oxide Electrolysis Cells: A Mini-Review. *Electrochem. Commun.* **2022**, *137*, 107267. [[CrossRef](#)]
448. Kim, S.J.; Kim, S.W.; Park, Y.M.; Kim, K.J.; Choi, G.M. Effect of Gd-Doped Ceria Interlayer on the Stability of Solid Oxide Electrolysis Cell. *Solid State Ion.* **2016**, *295*, 25–31. [[CrossRef](#)]
449. Jang, I.; Kim, S.; Kim, C.; Lee, H.; Yoon, H.; Song, T.; Paik, U. Interface Engineering of Yttrium Stabilized Zirconia/Gadolinium Doped Ceria Bi-Layer Electrolyte Solid Oxide Fuel Cell for Boosting Electrochemical Performance. *J. Power Sources* **2019**, *435*, 226776. [[CrossRef](#)]
450. Kim, S.J.; Kim, K.J.; Choi, G.M. Effect of  $\text{Ce}_{0.43}\text{Zr}_{0.43}\text{Gd}_{0.1}\text{Y}_{0.04}\text{O}_{2-\delta}$  Contact Layer on Stability of Interface between GDC Interlayer and YSZ Electrolyte in Solid Oxide Electrolysis Cell. *J. Power Sources* **2015**, *284*, 617–622. [[CrossRef](#)]
451. Ni, N.; Xiao, W.; Zheng, C.; Jiang, J.; Yu, Y.; Hao, W.; Tang, M.; Shen, H.; Peng, D. Flash Cosintering of a Lanthanum Strontium Cobalt Ferrite Nanofibre/Gd-Doped Ceria Bilayer Structure. *J. Eur. Ceram. Soc.* **2022**, *42*, 2870–2878. [[CrossRef](#)]
452. He, A.; Onishi, J.; Gong, J.; Shikazono, N. Three-Dimensional Optimization of  $\text{La}_{0.6}\text{Sr}_{0.4}\text{Co}_{0.2}\text{Fe}_{0.8}\text{O}_3$  Cathode Microstructure with Particle Radius Constraint. *Electrochim. Acta* **2021**, *398*, 139287. [[CrossRef](#)]
453. He, A.; Onishi, J.; Gong, J.; Shikazono, N. Microstructure Optimization of Porous Mixed Ionic and Electronic Conducting Cathode for Solid Oxide Fuel Cells. *J. Power Sources* **2020**, *478*, 228771. [[CrossRef](#)]
454. He, A.; Onishi, J.; Shikazono, N. Numerical Optimization of the Solid Oxide Fuel Cell Electrode-Electrolyte Interface Structure with Adjoint Method. In *Proceedings of the ECS Transactions*; Eguchi, K., Singhal, S.C., Eds.; Electrochemical Society Inc.: Philadelphia, PA, USA, 2019; Volume 91, pp. 2045–2054. [[CrossRef](#)]
455. Sharma, S.; Stanley, R.; Kumari, N. Electrochemical Modeling and Simulation of  $\text{CO}_2$  Reduction in Solid Oxide Electrolysis Cells. *J. Hazard. Toxic Radioact. Waste* **2022**, *26*, 04022005. [[CrossRef](#)]
456. Yang, T.; Liu, J.; Lei, Y.; Li, W.; Cheng, T.-L.; Finklea, H.; Wen, Y.-H.; Liu, X.; Abernathy, H.W.; Lee, S.; et al. Investigation of LSM–YSZ Composite Cathode Performance Degradation with a Multistep Charge Transfer Model. *J. Electrochem. Soc.* **2019**, *166*, F448–F457. [[CrossRef](#)]
457. Ananyev, M.V.; Farlenkov, A.S.; Eremin, V.A.; Kurumchin, E.K. Degradation Kinetics of LSM–YSZ Cathode Materials for SOFC. *Int. J. Hydrogen Energy* **2018**, *43*, 951–959. [[CrossRef](#)]
458. Cook, K.; Wrubel, J.; Ma, Z.; Huang, K.; Jin, X. Modeling Electrokinetics of Oxygen Electrodes in Solid Oxide Electrolyzer Cells. *J. Electrochem. Soc.* **2021**, *168*, 114510. [[CrossRef](#)]
459. Yan, Z.; He, A.; Hara, S.; Shikazono, N. Modeling of Solid Oxide Fuel Cell (SOFC) Electrodes from Fabrication to Operation: Correlations between Microstructures and Electrochemical Performances. *Energy Convers. Manag.* **2019**, *190*, 1–13. [[CrossRef](#)]
460. He, A.; Shimura, T.; Gong, J.; Shikazono, N. Numerical Simulation of  $\text{La}_{0.6}\text{Sr}_{0.4}\text{Co}_{0.2}\text{Fe}_{0.8}\text{O}_3-\text{Gd}_{0.1}\text{Ce}_{0.9}\text{O}_{1.95}$  Composite Cathodes with Micro Pillars. *Int. J. Hydrogen Energy* **2019**, *44*, 6871–6885. [[CrossRef](#)]
461. Subramanian, Y.; Veena, R.; Muhammed Ali, S.A.; Kumar, A.; Gubediran, R.K.; Dhanasekaran, A.; Gurusamy, D.; Muniandi, K. Artificial Intelligence Technique Based Performance Estimation of Solid Oxide Fuel Cells. *Mater. Today Proc.* **2023**, *80*, 2573–2576. [[CrossRef](#)]
462. Donazzi, A.; De Pascali, S.; Garavaglia, F.; Bracconi, M. A Quasi 2D Model for the Interpretation of Impedance and Polarization of a Planar Solid Oxide Fuel Cell with Interconnects. *Electrochim. Acta* **2021**, *365*, 137346. [[CrossRef](#)]
463. Iwai, H.; Maejima, K.; Kishimoto, M.; Saito, M.; Yoshida, H.; Kishimoto, H.; Yamaji, K.; Yokokawa, H. Numerical Model of Sulfur Poisoning on LSCF Cathode and Its Application to a 2-D Single Cell Simulation. In *Proceedings of the ECS Transactions*; Eguchi, K., Singhal, S.C., Eds.; Electrochemical Society Inc.: Philadelphia, PA, USA, 2019; Volume 91, pp. 2115–2125.
464. Effori, E.; Laurencin, J.; Tezyk, V.; Montella, C.; Dessemond, L.; Siebert, E. A Physically-Based Modelling to Predict the Cyclic Voltammetry Response of LSCF-Type Electrodes: Impact of the Ohmic Losses and Microstructure. *Solid State Ion.* **2021**, *371*, 115765. [[CrossRef](#)]

**Disclaimer/Publisher's Note:** The statements, opinions and data contained in all publications are solely those of the individual author(s) and contributor(s) and not of MDPI and/or the editor(s). MDPI and/or the editor(s) disclaim responsibility for any injury to people or property resulting from any ideas, methods, instructions or products referred to in the content.